ASSESSMENT OF CORROSION-FATIGUE DEGRADATION OF GRADE R4 STEEL USING AN ELECTROCHEMICAL-MECHANICAL COMBINED APPROACH

FELIPE AZEVEDO CANUT

TESE DE DOUTORADO EM CIÊNCIAS MECÂNICAS
DEPARTAMENTO DE ENGENHARIA MECÂNICA

FACULDADE DE TECNOLOGIA

UNIVERSIDADE DE BRASÍLIA

UNIVERSIDADE DE BRASÍLIA
FACULDADE DE TECNOLOGIA
DEPARTAMENTO DE ENGENHARIA MECÂNICA

ASSESSMENT OF CORROSION-FATIGUE DEGRADATION OF GRADE R4 STEEL USING AN ELECTROCHEMICAL-MECHANICAL COMBINED APPROACH

FELIPE AZEVEDO CANUT

Orientador: PROF. EDGAR NOBUO MAMIYA, PHD.
(UNIVERSIDADE DE BRASÍLIA)
Coorientadora: PROFA. ALDA MARIA PEREIRA SIMÕES, PHD.
(UNIVERSIDADE DE LISBOA, PORTUGAL)

TESE DE DOUTORADO EM CIÊNCIAS MECÂNICAS

BRASÍLIA-DF, 30 DE AGOSTO DE 2022.

UNIVERSIDADE DE BRASÍLIA
FACULDADE DE TECNOLOGIA
DEPARTAMENTO DE ENGENHARIA MECÂNICA

ASSESSMENT OF CORROSION-FATIGUE DEGRADATION OF GRADE R4 STEEL USING AN ELECTROCHEMICAL-MECHANICAL

FELIPE AZEVEDO CANUT

TESE DE DOUTORADO ACADÊMICO SUBMETIDA AO DEPARTAMENTO DE ENGENHARIA MECÂNICA DA FACULDADE DE TECNOLOGIA DA UNIVERSIDADE DE BRASÍLIA, COMO PARTE DOS REQUISITOS NECESSÁRIOS PARA A OBTENÇÃO DO GRAU DE DOUTOR EM CIÊNCIAS MECÂNICAS

APROVADA POR:

Prof. Edgar Nobuo Mamiya, PhD. (Universidade de Brasília, Brasil)
Orientador

Prof. João Carlos Salvador Santos Fernandes, PhD. (Universidade de Lisboa, Portugal)
Examinador Externo

Prof. Waldek Wladimir Bose Filho, PhD. (Universidade de São Paulo, Brasil)
Examinador Externo

Prof. Jorge Luiz de Almeida Ferreira, PhD. (Universidade de Brasília, Brasil)
Examinador Interno

Prof. José Alexander Araújo, PhD. (Universidade de Brasília, Brasil)
Examinador Suplente

Acknowledgements

I would like to thank my advisor Prof. Edgar Mamiya for the continuous support and patience during my Ph.D study. His guidance was indispensable for the development of this research.

My sincere thanks to Prof. Alda Simões, my co-advisor, for her patience, motivation, and immense knowledge. This study would not be possible without her help.

I greatly appreciate the support received from professors Luis Reis and Manuel Freitas during my stay at the *Instituto Superior Técnico* (IST). Their help was essential to the development of this work. I also would like to acknowledge the technical and infrastructural support provided by the IST during this period.

I would like to thank professors Ivan Bastos, Fábio Castro and Lucival Malcher for the fruitful discussions and important feedback during the development of this work.

I wish to acknowledge the help and infrastructure provided by the Grupo de Fadiga, Fratura e Materiais (GFFM) the Mechanical Engineering department of the University of Brasília.

I thank my fellow labmates Cainã, Eduardo, Guilherme, LC, Raniere, Vinícius and Vítor for the stimulating discussions and for all the fun we have had in the last years.

This research was partially funded by Petrogal S.A./ISPG Brasil S.A. (Contract number GALP 09 - Durabilidade de Componentes de Sistemas de Amarração para Uso em Águas Profundas: Experimentação e Modelagem – DSAM) and Agência Nacional do Petróleo, Gás Natural e Biocombustiveis - ANP (Contract number 19103-1). These funders are gratefully acknowledged for the financial support. I also would like to express my thanks for the scholarship provided by CAPES.

Last but not least, I am grateful to my family, Vera Cristina, Respino, Vera Maria, Vasco and Marina, for their unconditional support.

Abstract

The study deals with the combined effect of corrosion and mechanical cyclic stresses observed on the grade R4 steel. This material is commonly employed in the production of mooring chains used on Floating Production Storage and Offloading (FPSO). Corrosion-fatigue tests under stress-controlled loading were performed in artificial seawater (3.5 wt.% NaCl) using a corrosion cell developed for this purpose. Fully reversed ($R = -1$) and tension-tension ($R = 0.1$) loads were applied. In-air fatigue and no-load immersion tests were also carried out for comparative purposes. The results have shown an acceleration of the failure caused by the corrosive environment when compared to the in-air fatigue. The corrosive environment has a greater detrimental effect towards lower stress amplitudes on the observed corrosion-fatigue life. Periodic corrosion potential measurements were carried out during the experiments and the acquired signals were correlated with the degradation level of the specimen. This technique has proven to be effective in detecting important phenomena, such as pitting formation and crack initiation. Electrochemical Impedance Spectroscopy (EIS) measurements were performed to assess the evolution of the electrochemical system during the corrosion fatigue tests and the results were compared to non-loaded specimens. The specimens were examined in a Scanning Electron Microscope (SEM) and in a Confocal microscope. The corrosion degradation on the surface of the specimens was assessed using the corroded area fraction as an index. The microscopic analysis revealed that the application of mechanical loads together with chemical exposure produces a higher fraction of corroded area when compared to the no-load immersion samples, highlighting the synergistic nature of the corrosion fatigue phenomenon. A higher density of microcracks and pits were observed for the lower fatigue loads while large secondary cracks and few pits were identified for the higher amplitudes. Therefore, the failure of grade R4 steel in the seawater environment could be divided into two regimes: one dominated by electrochemical effects, observed in lower stress amplitudes, and the other dominated by mechanical effects for higher stress amplitudes.

Keywords : Corrosion-Fatigue, Grade R4 Steel, Corrosion Potential, Electrochemical Impedance Spectroscopy.

Resumo

O estudo trata do efeito combinado de carregamentos mecânicos cíclicos em ambiente corrosivo no aço grau R4. Este material é comumente empregado na produção de correntes de amarração das Unidades Flutuantes de Produção, Armazenamento e Transferência (FPSO). Ensaios de fadiga sob corrosão controlados por tensão foram realizados em água do mar artificial (3,5 p.% de NaCl). Uma célula de corrosão foi desenvolvida para esta finalidade. Carregamentos completamente alternados ($R = -1$) e na presença de carga média ($R = 0,1$) foram utilizados nos experimentos. Testes de fadiga em ar e testes de imersão pura também foram realizados para fins comparativos. Os resultados mostraram uma aceleração da falha causada pelo ambiente corrosivo quando comparada à fadiga em ar. O efeito do ambiente corrosivo se torna mais severo para amplitudes de tensão mecânica menores. Medições periódicas do potencial de corrosão foram realizadas durante os experimentos e os sinais adquiridos foram correlacionados com o nível de degradação do corpo de prova. Esta técnica se mostrou eficaz na detecção de fenômenos importantes, como a formação de pites e iniciação de trincas. Medições de Espectroscopia de Impedância Eletroquímica (EIS) foram realizadas para avaliar a evolução do sistema eletroquímico durante os testes de fadiga sob corrosão e os resultados foram comparados com corpos de prova em imersão pura. Os corpos de prova também foram examinados em Microscópio Eletrônico de Varredura (SEM) e em microscópio confocal. A degradação da superfície lateral dos corpos de prova pelo efeito da corrosão foi avaliada usando a fração de área corroída como parâmetro. A partir da análise de microscópio, constatou-se que a aplicação de carga mecânica combinada com a exposição ao ambiente salino gera uma fração de área corroída maior em relação às amostras em imersão pura, destacando a natureza sinérgica da fadiga sob corrosão. Uma grande densidade de microfissuras e pites foi observada para as menores cargas de fadiga, enquanto poucos pites e grandes trincas secundárias foram identificados para as maiores amplitudes de tensão. Assim, a falha do aço grau R4 em ambiente salino pôde ser dividida em dois regimes: um dominado por efeitos eletroquímicos, observado para menores amplitudes de tensão, e outro dominado por efeitos mecânicos, observado em maiores amplitudes de tensão.

Palavras-chave: Fadiga sob Corrosão, Aço Grau R4, Potencial de Corrosão, Espectroscopia de Impedância Eletroquímica.

Contents

List of Figures

List of Tables

List of Symbols

BPD	Barrels per Day
CE	Counter Electrode
CFCG	Corrosion Fatigue Crack Growth
CPE	Constant Phase Element
EIS	Electrochemical Impedance Spectroscopy
FFT	Fast Fourier Transform
FPS	Floating Production Systems
FPSO	Floating Production Storage and Offloading
IACS	International Association Classification Societies
OPB	Out-of-Plane Bending
PSB	Persistent Slip Band
RE	Reference Electrode
ROV	Remotely Operated Vehicle
SEM	Scanning Electron Microscope
SENB	Single Edge Notched Bend
SHE	Standard Hydrogen Electrode
SWT	Smith-Watson-Topper
THD	Total Harmonic Distortion
VHCF	Very High Cycle Fatigue
WE	Working Electrode

Chapter 1 – Introduction

This study is part of a project sponsored by *GALP Energia*, which aims to study failures on mooring chain links of Floating Production Storage and Offloading (FPSO) units and focuses on the investigation of the corrosion fatigue behavior of grade R4 steel. The following topics were addressed within the project's framework:

- Investigation of the corrosion fatigue behavior of grade R4 steel. The experiments performed for the development of this research were carried in collaboration with *Instituto Superior Técnico* (IST) - University of Lisbon (Canut *et al.*, 2019a; Canut *et al.*, 2019b; Canut *et al.*, 2021).
- Experiments and modeling of fatigue of mooring chains subjected to out-of-plane bending using a reduced scale testing rig developed for this purpose (Mamiya *et al.*, 2019).
- Multiaxial fatigue analysis of the marine material grade U2 steel (Castro *et al.*, 2019).
- Computational fatigue life estimation of the fairlead-mooring chain system.

1.1 Scope and main contributions

This Ph.D. thesis is focused on the joint effect of corrosion and mechanical cyclic stresses observed on grade R4 steel. The tests were performed in artificial sea water under load control. Fully reversed experiments and tests in the presence of mean stress were performed. Monitoring of the corrosion-fatigue degradation was performed using an electrochemical approach, with a setup developed for the purpose, which allows electrochemical measurements to be performed during the application of the cyclic mechanical loads. After the failure, the specimens were examined in a Scanning Electron Microscope (SEM) and in a Confocal microscope. The corrosion degradation on the surface of the specimens was assessed using the corroded area fraction as a parameter. A new corrosion fatigue test approach was also proposed to overcome the fact that a variation on the applied stress amplitude causes a different corrosion fatigue life, hence different immersion period. A trunk conical-shaped specimen was designed, enabling the application of a range of stress amplitudes simultaneously. This method has shown to be both cost and time efficient since one specimen can be used to analyze a wide range of load conditions.

This phase of the project yielded to the following original contributions:

- The corrosion potential monitoring technique has proven capable of identifying important phenomena, such as crack initiation and crack propagation, on the material under corrosion-fatigue loading condition. Although this technique has already been applied to different materials, its use on grade R4 steel is unprecedented. This contribution (Canut *et al.*, 2019a) is published in the Fatigue & Fracture of Engineering Materials & Structures journal.

- Electrochemical Impedance Spectroscopy results, carried out simultaneously with the corrosion fatigue tests, have been compared to a reference sample submitted to a no-load immersion. This contribution (Canut *et al.*, 2019b) is published in the Proceedings of the 7th International Symposium on Solid Mechanics.

- A quantitative corrosion level analysis, using a Python script developed for this purpose, has shown the synergistic nature of the corrosion fatigue phenomenon on the grade R4 steel. Some partial results involving this study are published (Canut *et al.*, 2021) in the 26^{th} International Congress of Mechanical Engineering Conference proceedings.

- The use of trunk conical specimens associated with a quantitative corrosion level analysis has shown the effects of the stress amplitude on the corrosion fatigue degradation. With this approach, the immersion time was kept constant for a range of stress amplitudes.

The aforementioned contributions were published in the following references:

F. A. Canut, A. M. Simões, L. Reis, M. Freitas, I. N. Bastos, F. C. Castro and E. N. Mamiya. "Monitoring of corrosion-fatigue degradation of grade R4 steel using an electrochemical-mechanical combined approach". In: *Fatigue & Fracture of Engineering Materials & Structures* 42.11 (July 2019), pp. 2509-2519.

F. A. Canut, A. Simões, L. Reis, I. Bastos, E. Mamiya and G. Ferreira. "Influence of Mechanical Cyclic Loads on the Corrosion Rate of Grade R4 Steel". In: *Proceedings of the 7th International Symposium on Solid Mechanics.* ABCM, 2019.

F. A. Canut, A. Sim oes, L. Reis, I. Bastos and E. Mamiya. "Corrosion fatigue analysis of grade R4 Steel in simulated seawater." In: *Proceedings of the 26th International Congress of Mechanical Engineering.* ABCM, 2021.

E. Mamiya, F. Castro, G. Ferreira, E. N. Filho, F. Canut, R. Neves and L. Malcher. "Fatigue of mooring chain links subjected to out-of-plane bending: Experiments and modeling". In: *Engineering Failure Analysis* 100 (2019), pp. 206-213.

F. C. Castro, E. N. Mamiya, L. Malcher, F. A. Canut, G. V. Ferreira and R. S. Neves. "Multiaxial fatigue of quenched and tempered U2 steel: Testing and fatigue life prediction". In: *Fatigue & Fracture of Engineering Materials & Structures* (July 2019).

1.2 Motivation

The pre-salt discoveries are among the most important made in the world over the last decade. The discovery of these reserves created the possibility of higher productive wells compared to post-salt extraction [1]. Pre-salt oil is abundant in the Brazilian coast, and since 2017 pre-salt oil extraction has been greater than post-salt [2].

The discovery of deep-water oil reserves with depths exceeding 1500 m have created the necessity of new types of oil extracting structures, the so-called Floating Production Systems (FPS). This type of structure must stay at a fixed position for decades without dry-docking for inspection or repair. In Floating Production Storage and Offloading (FPSO) units, the stationkeeping positioning is achieved by using mooring systems composed of several lines. Each mooring line consists of an association of steel chains and synthetic ropes [3]. Steel chains are typically used at the top and the bottom ends of the mooring line (splash zone and trash zone, respectively), where the possibility of marine life growth due to sunlight exposure and the wear due to the contact with sea bed precludes the use of synthetic ropes.

Mooring systems are typically designed for lives that can exceed 20 years of service. During this timespan, steel chains must withstand field conditions combining corrosive marine aggressiveness and high static and dynamic loads. Environmental factors, such as wind, waves and currents, should be considered for a maximum operating condition using a 100-year return period criterion, *i.e.* the mooring system has to withstand the most severe environmental condition observed in the last 100 years [4].

The failure of a mooring line is a critical event that may have high environmental and economic costs. The cost of a single line failure can be as high as £10.5M [3], considering a production of 250 thousand barrels per day (BPD). Various sources of mooring line failure have been identified [5–7], as follows:

- Overload;
- Fatigue at a sheave or connection, often aggravated by Out of Plane Bending (OPB);
- Corrosion;
- Wear;
- Mechanical failure of the mooring line handling system.

A single line failure may cause overload of the remaining mooring lines leading to multiple line failure, which could result in hydrocarbon release and production shutdown due to free drifting of the FPSO unit. Single and multiple failures in the chain section observed from 2001 to 2011, have been reported [7] as summarized in Table 1.1. It is noteworthy that the multiple lines failure observed in the *Gryphon Alpha* vessel resulted in rupture of the riser and oil release.

Table 1.1: Mooring Chains Incidents between 2001 and 2011 (Adapted from [7])

Year	Vessel Name	Number of Lines Failed	Age of the Component
2011	Banff	5	12 years
2011	Gryphon Alpha	4	19 years
2011	Fluminense	1	8 years
2010	Jubarte	3	2 years
2008	Dalia	1	2 years
2008	Balder	1	9 months
2006	Schiehallion	1	8 years
2006	Varg	1	7 years
2005	Foinaven	1	2 years
2003	Girassol buoy	1	2 years
2002	Girassol buoy	3	8 months

Since the mooring system is a critical component to ensure a safe operation in FPSO units, the evolution of degradation in mooring lines has to be properly monitored. However, data reported for the north sea FPSOs [3] indicate that 50% of the units cannot monitor line tensions in real-time. The monitoring system usually consists of load cells to measure the force on each line and/or inclinometers to measure the angle of the lines, which can also give an estimative of the line tension. However, the monitoring of the load alone does not guarantee safe operation, since the fatigue life of the metallic elements of the mooring line are highly dependent on the level of corrosion degradation.

Regarding the corrosion evolution on mooring chains, monitoring is usually performed by visual inspection using a remotely operated vehicle (ROV). This is not an easy task, especially when the chain links are almost entirely covered with marine life, as shown in Fig. 1.1 [8].

(a) **(b)**

Figure 1.1: Mooring chains (a) before and (b) after cleaning the marine life [8].

Protection against corrosion is usually provided by increasing the diameter of the chain links.

According to the standard API RP 2SK [4], the diameter of chain links situated in the splash zone or trash zone must consider an additional 0.4 mm to 1.0 mm per year of designed service life.

The behavior of offshore structural steels is strongly affected by the presence of seawater environment, and structures become susceptible to premature crack initiation and higher rates of crack propagation [9] leading to a decrease in fatigue strength. The combined damage due to corrosion and cyclic loading has been observed to be greater than the damage caused by each of them acting separately [10, 11]. There are many studies on the effect of the maritime environment on the fatigue life of mooring chain steels [8–12], and on the effect of local physicochemical parameters (*e.g.*, temperature, salinity, dissolved oxygen) on the corrosion rate [13]. Nevertheless, many aspects of the synergy between corrosion and fatigue remain open.

Numerous experimental apparatuses have been proposed to address the phenomenon of *in-situ* corrosion-fatigue [9–11, 14–20]. Although some authors [9–11] have studied the behavior of steel alloys used in the manufacturing of mooring lines, the testing conditions were quite different from the in-field ones. Palin-Luc, Perez-Mora and co-workers [10, 11] performed tests in very high cycle fatigue (VHCF) testing rig at 20 kHz load frequency, which is much greater than the typical off-shore loading frequency (0.1 Hz to 0.2 Hz). Rampi and Vargas carried out *in-situ* corrosion-fatigue tests using already notched (SENB - single edge notched bend) specimens [9]. These studies also focussed on the mechanical aspects of the corrosion fatigue, and no electrochemical data was analysed.

Some studies [18–20] carried out electrochemical-mechanical combined analyses of corrosion-fatigue tests for different materials. These studies correlated the shapes of the electrochemical responses with the degradation of the specimen. Tada [18, 19] was able to detected the crack initiation phase by monitoring either the evolution oh harmonics in the current response or the decrease in phase shift between strain and current responses. However, the current measurement required the application of a certain level of polarization leading to a condition that does not represent the free corrosion behavior of the material. Recently [20], the corrosion fatigue behavior of magnesium alloys was characterized. Corrosion potential response was used on the identification of the cracking mechanisms in low cycle fatigue and high cycle fatigue regimes.

Electrochemical current monitoring also gives valuable information about the kinetics of the corrosion-fatigue system. However, its measurement commonly requires the application of a certain level of polarization leading to a condition that does not represent the free corrosion behavior of the material. Another powerful electrochemical technique, which allows measurement of corrosion rates and learning about corrosion mechanisms is the Electrochemical Impedance Spectroscopy (EIS), in which an alternating potential or current signal is applied to an electrochemical cell and the resulting current (or potential) fluctuations is measured. The technique has been successfully applied on stainless steel under corrosion-fatigue degradation [17].

1.3 Objectives

The main objective of this research is to study the uniaxial behavior of the grade R4 steel simultaneously under corrosive environment and cyclic mechanical loading. Fully alternated ($R = -1$) and tension-tension ($R = 0.1$) tests were carried out with the fatigue lives varying between 10^3 and 2.10^6 cycles. In order to achieve this goal, the following specific objectives were proposed:

- Study of the influence of the corrosive environment on the fatigue life of grade R4 steels. Corrosion-fatigue and in-air fatigue experiments were carried out and the observed lives were compared in order to evaluate the detrimental effects of the aggressive environment.
- Study of the influence of environmental variables on the degradation mechanisms of the grade R4 steel. For this purpose, small variations on the corrosion potential response of the material due to cyclic loading were monitored and investigated during corrosion-fatigue tests. Valuable information on the mechanisms of degradation of offshore steel under corrosion-fatigue condition is drawn from these measurements.
- Study of the influence of the cyclic mechanical loads on the corrosion behaviour of the material. A corrosion level quantitative analysis was carried out using the fraction of corroded area for different loading conditions as an index. Microscopic analysis was also performed in order to obtain qualitative information about the morphology of the corroded specimens after the corrosion fatigue tests.

This document is organized as follows: Chapter 2 presents an overview of the theoretical aspects involved in corrosion-fatigue. In Chapter 3, the experimental setup and procedures were depicted. The results of the corrosion-fatigue experiments, as well as the electrochemical measurements are shown in Chapter 4 and discussion in Chapter 5. The main conclusions and the next steps are summarized in Chapter 6.

Chapter 2 – Literature Review

In this section, a brief overview of electrochemistry and some important information on corrosion fatigue are presented. Then, a concise review of the main setups used for testing corrosion fatigue is presented. Lastly, a description of the critical loading mode, observed at the top portion of the mooring lines, is described.

2.1 Electrochemistry

This section presents some concepts related to the thermodynamics and kinetics of electrochemical reactions. These concepts were used in the design and the discussion of the corrosion fatigue experiments presented in Chapter 3. Further details on these subjects can be found, for instance, in references [21–26].

Corrosion is defined as the destruction or deterioration of a metal because of the reaction with its environment and it is often classified as uniform or localized[23]. Both are fundamentally electrochemical processes, but while the first affects almost uniformly the entire surface exposed to the corrosive agent, the second attacks the metal locally. Uniform corrosion is very common in carbon steel where it usually results in the formation of the so-called rust. Normally, the damages caused by uniform corrosion are evaluated by the thickness loss (or mass loss) of the exposed component. Localized corrosion can proceed very rapidly along intergranular or transgranular paths to go through the thickness of a component. In these cases, the mass loss can be almost imperceptible, but the geometric defects resulting from this localized attack create stress concentrators that can cause catastrophic failure on the structure.

An electrochemical reaction is a process in which electrons are present as reactants or products. The description of the equilibrium state of an electrochemical system is defined so the content of energy between the stoichiometric quantities of products and reagents are equal, as follows:

$$\sum_i \nu_i \widetilde{\mu}_i = 0, \tag{2.1}$$

where ν_i is the stoichiometric coefficient of the species i and $\widetilde{\mu}$ is the so-called electrochemical potential, given by:

$$\widetilde{\mu} = \left(\frac{\partial G}{\partial n_{mol,i}}\right)_{T,p,j\neq i} = \mu_i + z_i F \varphi^{\alpha}, \tag{2.2}$$

where G is the Gibbs free energy, $n_{mol,i}$ represents the number of mols of the i^{th} species for constant absolute temperature T and pressure p, z_i is the charge of the species, φ^{α} is the inner potential felt by the species in the α phase [21]. The chemical potential, μ_i, can be expressed in terms of the activity, a, as:

$$\mu_i = \mu_i^0 + RT \ln a_i, \tag{2.3}$$

where μ_i^0 is the chemical potential of a species in its standard state. The activity can be understood as the effective concentration of a species in the chemical reaction and is equal to unity for pure substances, by definition. For solutions at low concentration, the activity of a species can be considered approximately equal to its concentration.

The electrochemical equilibrium at the solution/electrode interface can be described as:

$$\widetilde{\mu}_i^s = \widetilde{\mu}_i^e. \tag{2.4}$$

Hence:

$$\mu_i^s + z_i F \varphi^s = \mu_i^e + z_i F \varphi^e, \tag{2.5}$$

where the superscripts s and e are related to the solution and electrode, respectively. The potential difference at the solution/electrode interface, $\Delta\varphi$, is given by:

$$\Delta\varphi = \varphi^s - \varphi^e = \frac{\mu_i^s - \mu_i^e}{z_i F} \tag{2.6}$$

The so called Nernst equation is obtained by substituting the chemical potentials, μ_i^s and μ_i^e,

in Eq. 2.6,

$$\Delta\varphi = \Delta\varphi^0 - \frac{RT}{z_i F} \ln a_i^s. \tag{2.7}$$

The potential difference, $\Delta\varphi$, given by Equation 2.7 is valid only for the solution/electrode interface and it is not measurable. The electrochemical potential measurements are carried out by comparing the potential difference between a work and a reference electrode. By convention, the Standard Hydrogen Electrode (SHE) is the standard measurement of electrode potential for the thermodynamic scale, *i.e.* $\Delta\varphi^{SHE} = 0$. Therefore, the electrochemical potential of an electrode compared to the SHE is expressed by:

$$E = \Delta\varphi - \Delta\varphi^{SHE}, \tag{2.8}$$

$$E = E^0 - \frac{RT}{z_i F} \ln a_i^s. \tag{2.9}$$

And considering a general chemical reaction, Eq. 2.9 yields:

$$E = E^0 - \frac{RT}{z_i F} \ln \frac{\prod a^\nu(Products)}{\prod a^\nu(Reactants)}. \tag{2.10}$$

Equation 2.10 highlights that the thermodynamic state of a system depends not only on the corrosion potential but also on the concentration of the species that are part of the electrochemical reaction. The concentration of H^+ (pH) is one of the most important aspects on electrochemical reactions, so it is very common to illustrate the thermodynamic equilibrium as a *potential - pH* diagrams, the so-called Pourbaix diagrams [27]. The Pourbaix diagram for iron corroding in water at 25° C is shown in Fig. 2.1 in which E_{O_2/H_2O} is the equilibrium potential for the oxygen electrode reaction, E_{H^+/H_2} is the equilibrium potential for the hydrogen electrode reaction, and V_{SHE} is volt on the standard hydrogen electrode scale.

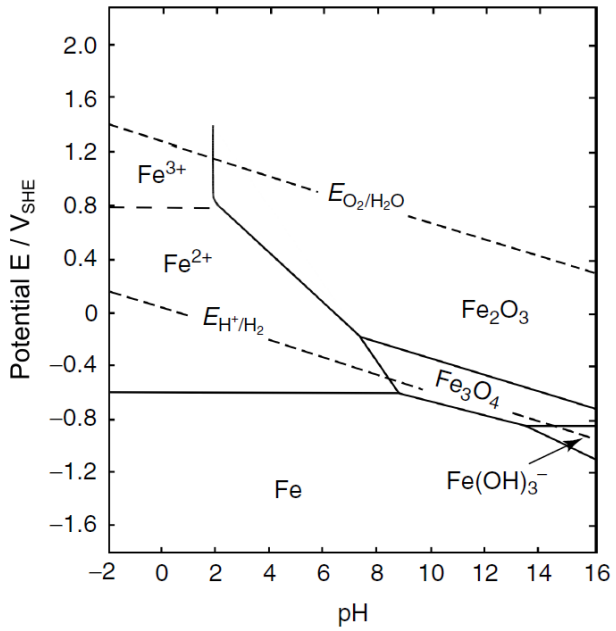

Figure 2.1: Potential–pH diagram for iron corrosion in water at room temperature [26].

The electrochemical thermodynamics is important to evaluate which reactions are possible. However, in order to evaluate corrosion rates, the electrochemical kinetics needs to be addressed. The current generated by each electrochemical reaction can be calculated by Faraday's law, which relates the charge Q with the number of moles electrons involved, as it follows:

$$Q = FNz, \tag{2.11}$$

where N is the number of moles converted, z is the number of electrons exchanged per molecule of the species and F is the Faraday's constant, in which 1 F is equivalent to 96458 C/(mol of electrons). The current I of the reaction is given by:

$$I = \frac{\mathrm{d}Q}{\mathrm{d}t}, \tag{2.12}$$

where t is the duration of the electrochemical process.

For a metal corroding spontaneously in aqueous environment, both anodic and cathodic reactions take place simultaneously at the metallic surface. The electrons released in the anodic reaction flow through the metal and react with the solution at cathodic sites, meaning that there is no net charge accumulation, otherwise the metal would become spontaneously charged. These two processes have the equilibrium potentials E_a (for the anodic reaction) and E_c (for

the cathodic reaction), and can be generically described as:

$$\mathrm{Red}_1 \rightleftharpoons \mathrm{Ox}_1 + \mathrm{n}_1\,\mathrm{e}^-, \tag{2.13}$$

$$\mathrm{Ox}_2 + \mathrm{n}_2\,\mathrm{e}^- \rightleftharpoons \mathrm{Red}_2. \tag{2.14}$$

Considering that the metal is immersed in a sufficiently conductive solution, it is expected that the cathodic potential, E_c, shifts to a more negative potential, E'_c, whereas the anodic potential, E_a, shifts to a more positive potential, E'_a, until the potential difference $\Delta E = E'_c - E'_a$ becomes practically zero. Therefore, the corrosion potential, E_{corr}, can be defined as:

$$E_{corr} = E'_a = E'_c. \tag{2.15}$$

It is important to notice that neither E'_a or E'_c corresponds to the equilibrium potentials of the reactions 2.13 and 2.14. In this case, the rate of the reactions are:

$$|I_a| = |I_c|, \tag{2.16}$$

where $|I_a|$ and $|I_c|$ are the absolute anodic and cathodic currents. In order to better understand the local processes involved in the electrochemical reactions, the current densities i_a and i_c are defined in terms of the anodic and cathodic surfaces, S_a and S_c as:

$$I_{anodic} = i_a S_a = I_{cathodic} = i_c S_c, \tag{2.17}$$

$$i_a = i_c \frac{S_c}{S_a}. \tag{2.18}$$

Equation 2.18 highlights how harmful localized anodic regions, such as pits or localized plastic strain sites [28], can be. In these regions, the anodic surface is much smaller than the cathodic surface ($S_a/S_c \ll 1$). Therefore, local anodic dissolution can be very severe, even for low overall anodic currents. The current density associated with the anodic reaction, i_a, is in practice the corrosion current, i_{corr}, and corresponds to the rate of the metallic corrosion.

The corrosion kinetics is usually described by the electrode potential versus the reaction current curves of both the anodic oxidation and the cathodic reduction, as schematically shown in Fig. 2.2. The intersecting point of the anodic and cathodic polarization curves represents the state of corrosion: the corrosion potential (E_{corr}) and the corrosion current (i_{corr}).

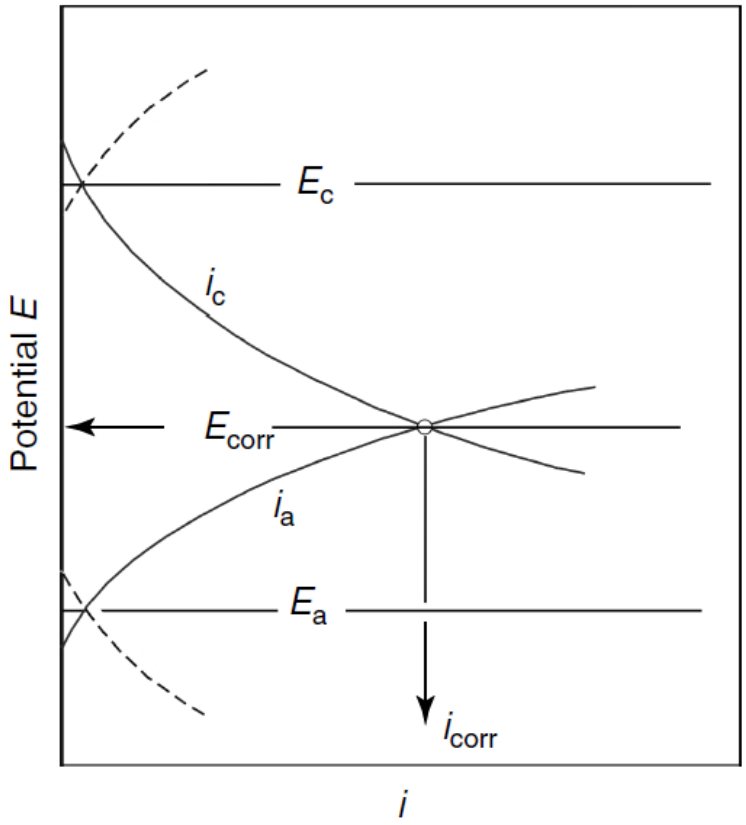

Figure 2.2: Illustrative curves for anodic and cathodic reactions assuming uniform reaction rates on the surface ($S_a = S_c$) [26].

2.1.1 Electrochemical Impedance Spectroscopy

Electrochemical Impedance Spectroscopy (EIS) is a powerful and non-destructive tool which allows investigating electrochemical properties by comparing the real corrosion system with an idealized electric circuit, formed by a set of resistors, capacitor and inductors. This is an attractive technique because the components of the equivalent electric circuit have a physical meaning. The EIS measurements are carried out by imposing an alternating potential (or current) and measuring the current (or potential) response over a range of frequencies. Considering a potentiostatic EIS (potential excitation), the imposed potential signal, $E(t)$, and the current response signal, $I(t)$, are expressed as follows:

$$E(t) = E_0 \sin(\omega t), \tag{2.19}$$

$$I(t) = I_0 \sin(\omega t + \phi), \tag{2.20}$$

where E_0 and I_0 are the amplitudes of potential and current, respectively, t is time, ϕ is the phase shift and ω is the radial frequency, which can be expressed as $\omega = 2\pi f$, where f is the

frequency in Hertz. The impedance of the electrochemical system is given by:

$$Z = \frac{E(t)}{I(t)} = \frac{E_0 \sin(\omega t)}{I_0 \sin(\omega t + \phi)} = Z_0 \frac{\sin(\omega t)}{\sin(\omega t + \phi)}. \tag{2.21}$$

The impedance can also be expressed as a complex number:

$$Z(\omega) = Z_0(\cos\phi + j\sin(\phi)). \tag{2.22}$$

For an EIS measurement to be considered valid, the perturbation signal should be small enough so the response is pseudo-linear and it must be due only to the excitation signal. The system also must be stable during the measurement. One way to guarantee the steady-state of the system is to repeat the EIS measurement and check for similar results.

For a simple equivalent circuit, such as the RC circuit, the resistors may either represent the bulk conductivity of the electrolyte or the electrode reaction. The former is also called as Electrolyte Resistance, R_E while the latter is called the Charge-Transfer Resistance, R_{CT}. The capacitor represents the double layer response due to the separation of charges on the metal-electrolyte interface this region behaves like a parallel plate capacitor. Thus, in this simplified system, the charges can either flow across the interface, which is controlled by the Charge-Transfer Resistance, R_{CT}, or form the double layer capacitance, C_{DL}. The charge movement through the solution is controlled by the electrolyte resistance, R_E. The impedance responses for resistors, Z_R, and capacitors, Z_C are given as follows:

$$Z_R = R, \tag{2.23}$$

$$Z_C = \frac{1}{j\omega C}, \tag{2.24}$$

where R is the resistance coefficient, and C is the capacitance. It is noteworthy that the impedance of a resistor is independent of frequency and thus has no imaginary component. This means the current that passes through the resistor (or an association of resistors) stays in phase with the applied potential. The capacitors, on the other hand, have only the imaginary component, which means that the applied potential and the current response have a phase shift of 90°.

The metallic interface is not always homogeneous, therefore, the double layer of a real system does not always behave like an ideal parallel plate capacitor. A constant phase element (CPE) can be used to take into account the heterogeneities on the metallic surface. The impedance of

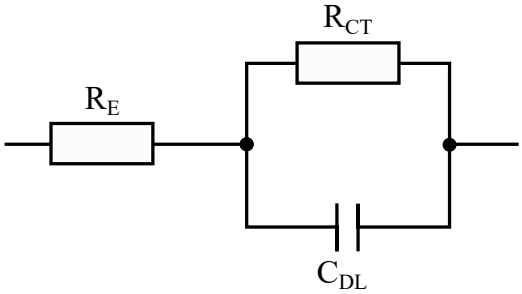

Figure 2.3: RC circuit diagram.

the CPE is given by:

$$Z_{CPE} = \frac{1}{Q(j2\pi f)^{\alpha}}, \tag{2.25}$$

where $j = \sqrt{-1}$, f is the frequency (Hz), Q is the phase-independent element, which is related with the exposed area and the exponent α takes into consideration the heterogeneities on the surface [29, 30]. Hence, substituting the ideal double layer capacitance by CPE, the equivalent circuit can be described as shown in Fig. 2.4.

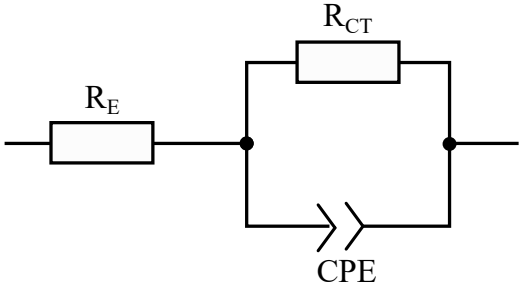

Figure 2.4: Modified RC circuit Diagram.

The EIS data is often presented in two forms as Nyquist or Bode plots. In the Nyquist representation, the real part of the impedance is represented in the abscissa and the imaginary part in the ordinate. For the sake of readability, the ordinate axis is often inverted. In this representation, each parallel association of a resistor with a capacitor defines a semicircle. One disadvantage of the Nyquist plot is that the frequency is not explicitly expressed. The Bode representation is composed of two plots: log of impedance modulus over the log of frequency and phase shift over the log of frequency, usually overlaid. The phase shift is also often presented in an inverted axis.

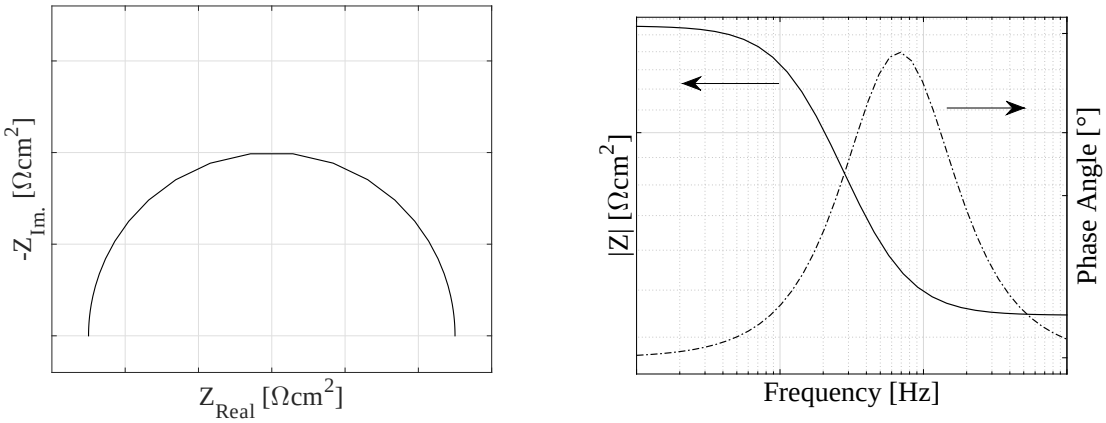

(a) **(b)**

Figure 2.5: Typical representation of EIS data, described by Eq. 2.22, as (a) Nyquist and (b) Bode plots.

From the EIS measurements, it is possible to extract the corrosion resistance (R_{corr}) of the system, which is inversely related to the corrosion rate. For the equivalent circuits presented in this section (Figs. 2.3 and 2.4) the corrosion resistance is represented by the charge transfer resistance. Even tough the circuits presented in this section are simple, they are suitable to describe the phenomena occurring in the spontaneous corrosion of bare steel in NaCl solution.

2.2 Corrosion Fatigue

It is well known that under corrosion fatigue conditions, the fatigue life can be lowered considerably and often the fatigue limit is no longer existent [31]. The classical fatigue life component can be split into two phases: crack initiation and crack propagation. Fatigue crack propagation life is often calculated using fracture mechanics [28]. It is known that corrosion can have a great influence on crack initiation and propagation.

During fatigue loading under uniform corrosion, a reduction of the cross section area over time is observed. Therefore, the effective stress amplitude will increase with time. Thus, in this condition, the fatigue life is determined by the general corrosion rate and the stress amplitude [31].

Most of the studies involving corrosion fatigue deal with stainless steels and alloys with passive behaviour and corrosion fatigue has been described by a mechanism involving several stages [32]: (i) passive film breakdown, (ii) corrosion defect nucleation and growth, (iii) pit to crack transition, and (iv) crack propagation. For materials that do not passivate spontaneously, the first stage is not observed. The growth rate of corrosion defects has been studied [33, 34] for different materials. It is accepted that a crack only nucleates after the corrosion defect, such as pits or crevices, reaches a critical size [34, 35]. Even for materials that undergo generalized

corrosion, it is observed that the crack initiates in a localized corroded site [36]. This local corrosion may onset at the intrusions and extrusions regions. These heterogeneities cause a permanent separation of the anodic and cathodic sites leading to local dissolution at the anodic sites. The crack propagation regime under corrosion fatigue condition is usually modelled using linear elastic fracture mechanics theory [37, 38]. However, studies [39, 40] have reported that in an early stage of crack propagation, when cracks are only a few grains in length, the mean crack growth rate can be greater than the rate predicted by specimens containing a long crack. This would, therefore, produce non-conservative predictions if one considers the crack growth rate corresponding to the steady crack growth regime.

The rate of degradation of a structure under corrosion fatigue condition depends on several mechanical and electrochemical parameters. Studies have focused on quantifying the effect of various parameters such as strain rate [41, 42], temperature [43] and corrosion-deformation interactions [18, 19, 44–46] on the fatigue life. Even though the material is simultaneously under electrochemical and mechanical interactions, most stages of this process seem to be mainly controlled by only one major driving force. While uniform corrosion and stable pitting growth are usually considered time-dependent phenomena, primarily controlled by electrochemical activity, the long crack propagation stage can be considered a cycle-dependent phenomenon, dominated by mechanical effects [28]. This is expected if one considers that during crack propagation the crack growth rate is higher than the dissolution rate at the crack tip [47]. Therefore, the determination of the portion of fatigue life for crack initiation and crack propagation is essential for a proper corrosion fatigue analysis.

2.2.1 Crack Initiation

Cyclic loads can cause irreversible plastic deformations that generate high local dislocation densities on slip planes. The occurrence of intrusion and extrusion due to persistent slip bands (PSB) movement could cause a favourable site where crack nucleation takes place [48]. For in-air fatigue, is usually accepted that crack initiation occurs at the surface of the material, although, under specific conditions such as very high cycles fatigue, a crack can nucleate from inclusions inside of the material [10].

The cracking mechanisms of a metallic material under in-air fatigue condition was first described in 1903 by Ewing and Humphrey [49]. It was observed that cyclic plastic shear strains eventually cause the nucleation of slip band. The first slip bands will be formed in grains whose crystallographic orientation in favourable with respect to the resultant shear stress. Considering that all grains have the same critical resolved shear stress, *i.e.* the shear stress at which plastic deformation initiates, they will yield and plastically deform at different applied stresses because of they are orientated in different orientations [50]. At low applied stresses only a few grains will have favourable orientations and only a few slip bands will form. At higher stresses, the critical resolved shear stress is exceeded in a grater number of grains, resulting in more slip

bands formation. During repeated cyclic loading these slip bands grow and coalescence into a single dominant fatigue crack.

Corrosion fatigue cracks are always initiated at the surface, unless there are near-surface defects that act as stress concentration sites and facilitate subsurface crack initiation. Surface features at origins of corrosion fatigue cracks vary with the alloy and with specific environmental conditions. In carbon steels, cracks often originate at hemispherical corrosion pits and often contain significant amounts of corrosion products. However, surface pitting is not a prerequisite for corrosion fatigue cracking of carbon steels. Corrosion fatigue cracks may occur in the absence of pits and follow grain boundaries or prior-austenite grain boundaries [51].

The corrosion fatigue cracks can initiate at the surface either intergranularly or transgranularly. Intergranular corrosion provides initiation sites at the surface for fatigue cracks which could then grow transgranularly [52]. Zhao and co-authors [53] performed corrosion fatigue experiments on high strength low alloy steel. They observed that crack initiation occurs preferable on grain boundaries for lower stress amplitudes, causing intergranular failure. For higher stress amplitudes, transgranular failure was observed, indicating that the mechanical component dominated the crack initiation process.

In the early stages of the corrosion fatigue failure, the main effect of the environment is to accelerate the plastic deformations and slip processes that precede short crack formation. The following phenomena can play an important role in this phase of the failure: *i)* slip band reversibility interference due to oxide films formation, *ii)* nucleation of dislocations caused by absorption of species, *iii)* injection of embrittling species, *e.g.* hydrogen embrittlement, *iv)* removal of plastically deformed material due to dissolution. At the crack propagation regime, two additional processes take place: *v)* Effect of corrosion products on the crack closure and *vi)* effect of the long and narrow crack on the diffusion of species present in the electrolyte which may result in a different chemical environment at the crack tip compared to the bulk solution [54].

Whitman and Evans [55] studied cold worked steel wire and concluded that cracks advanced by a combination of electrochemical and mechanical action. During the application of cyclic stresses, preferential attack of the slip bands was observed and attributed to the higher energy state of atoms at the crack tip than in the specimen body. Accordingly to the authors, the atoms associated with dislocations are preferentially attacked because it takes less activation energy to remove these atoms from the material. The dissolution unlocks otherwise blocked slip processes, accelerates extrusion-intrusion formation leading premature crack initiation. Zhao and co-workers [56] observed the formation of adherent corrosion products on the slip band surface. With the mechanical cycling, the recently formed slip band moves in the opposite direction which results in intrusion of oxides into the material, as shown in Fig 2.6.

For a material under corrosion, anodic processes can develop locally at Persistent Slip Bands (PSB) or crack tips. This local dissolution cannot proceed without the corresponding cathodic

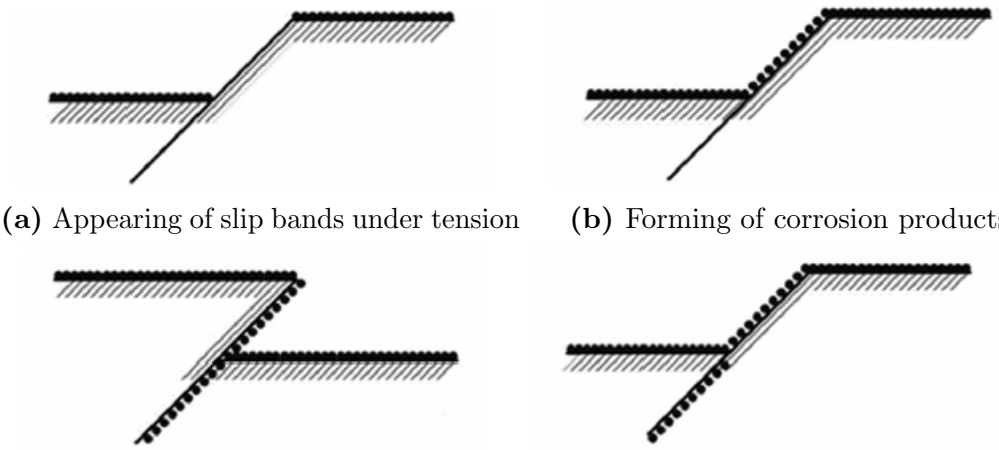

(a) Appearing of slip bands under tension **(b)** Forming of corrosion products

(c) Intruding of corrosion products under compression **(d)** Initiation of surface crack under tension

Figure 2.6: Formation of corrosion products on slipping bands in corrosion fatigue conditions [56].

process. At the nucleation stage, the anodic/cathodic surface ratio also plays an important role in the fatigue behaviour of the material. For instance, Cornet and Golan [57] carried out corrosion fatigue tests at different temperatures and observed that a more severe environment (higher temperature) had a beneficial effect on the corrosion fatigue life of steel rods. This was attributed to the fact that a more severe environment generated more pits on the metallic surface, increasing the anodic/cathodic surfaces ratio, which produced shallower corrosion defects and lower stress concentrators.

2.2.2 Crack Propagation

The environmental effect plays an important role in the corrosion fatigue crack propagation regime. The region near the crack tip tends to be more anodic compared to the surrounding environment, which makes crack tips susceptible to corrosion dissolution and thereby accelerates fatigue failure.

During the crack propagation regime, the environmental influence is more severe for microstructurally small cracks, where the crack growth rate for corrosion fatigue condition can be much higher when compared to fatigue in air [28, 32, 47]. Any oxidising agent will react rapidly with the fresh metal surface exposed by crack propagation. In this case, the extent of the reaction per cycle on the fresh material will depend on the duration of the mechanical cycle, *i.e.* loading frequency. Since dissolved oxygen cannot penetrate far down in the cracks, hydrogen evolution is the most likely driving reaction. In some cases, crack tip dissolution may also slow the corrosion fatigue cracking propagation down by blunting the crack tip [58].

The role of the corrosive environment on the corrosion fatigue crack propagation is not always straight forward. Depending on the dissolution rate of the metal, the crack tip surface

can blunt itself causing the crack to arrest. In these cases, the corrosive environment can actually reduce the crack growth rate [51].

For higher stress amplitudes the environmental effect on the Corrosion Fatigue Crack Growth (CFCG) rate can become negligible. This is expected if one considers that at higher stress amplitudes the CFCG is faster and the life is shorter, therefore, the aggressive medium has less time to contribute to the crack-tip degradation process [47].

The main processes that can affect the CFCG rate are:

- Exposure of bare material at the crack tip;
- Build up of oxides inside the crack which may restrict the crack closure;
- Separation of the anodic and cathodic sites

Even though numerous authors have studied the effects of different mechanical and electrochemical aspects on the corrosion fatigue life, a complete assessment of all variables present in this process is practically impossible [52].

2.3 Experimental setups for corrosion fatigue

There is no standard or globally accepted test rig for corrosion fatigue testing. Researchers have developed different testing rigs during the last years to meet their own necessities. A great number of apparatus has been proposed to simulate maritime environment [59]. A few other researchers considered different environments, but still designed usable measuring techniques that could be adapted to work with the seawater environment.

2.3.1 Rotating bending machines

Some authors have used corrosion chambers mounted in rotating bending machines. In this case, the rigs tend to be simpler when compared to the rigs mounted on servo-electric fatigue testing machines. Some notable rigs mounted on rotating bending machines were used by Li & Akid [60] and Infante [61]. The former developed a sealed chamber (Fig. 2.7a), while the later proposed a chamber with solution circulation system (Fig. 2.7b). A few downsides of this kind of apparatus are: *i)* It its impractical, if not impossible, to perform precise electrochemical measurements. Even for the second case (Fig. 2.7b), in which the chamber is fixed, the relative movement between the specimen and the solution would jeopardize the electrochemical measurements *ii)* The load applied is always fully reversed, ($R = -1$), which limits the study of components under fatigue in the presence of mean stress.

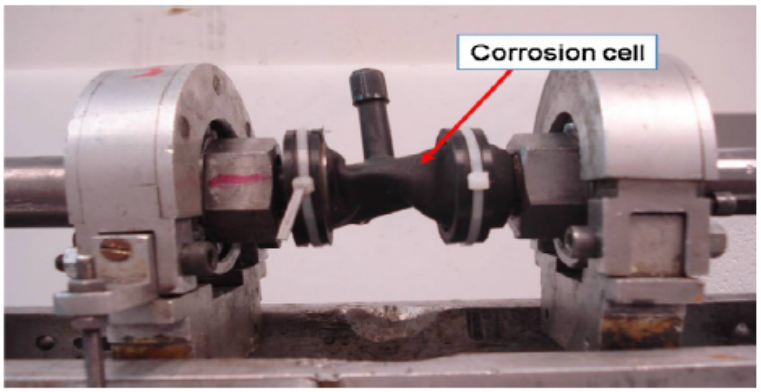

(a)

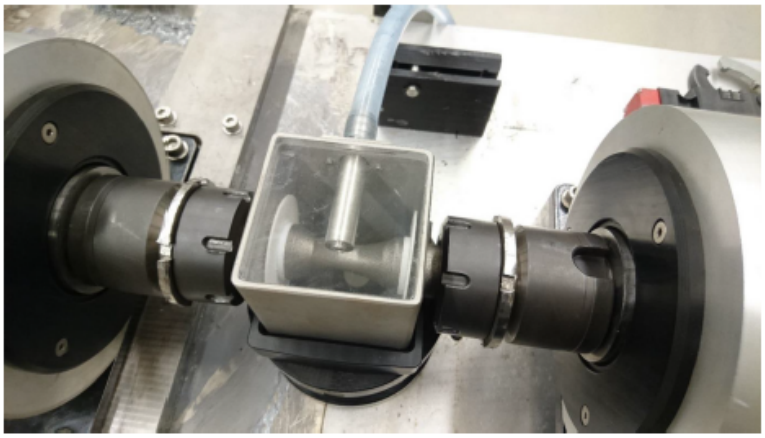

(b)

Figure 2.7: Testing rigs proposed by (a) Li & Akid [60] and (b) Infante [61] using rotary bending machines.

2.3.2 Servohydraulic fatigue testing machines

Corrosion chambers mounted on servohydraulic fatigue testing machines is often used as a testing rig. In fact, many researches [9, 15, 17–20, 38, 53, 62–64] used this approach in the last years. These apparatus can be mainly based on two approaches: fracture mechanics or fatigue.

Tests based on the fracture mechanics are carried out with pre-cracked specimens, therefore, they are suitable to evaluate only the crack propagation regime. Authors that use this type of experiments usually claim that crack initiation occurs faster in the corrosive environment and the greater part of the fatigue life is under the crack propagation regime. These tests aim to obtain the crack growth rate in terms of the applied stress intensity factor range and the behavior of the material in normally modeled by a modification of the Paris law [38]. An example of corrosion fatigue apparatus based on fracture mechanics is shown in Fig. 2.8. Using this apparatus, only a few loading cycles are required to calculate the crack growth rate at a given stage of the experiment. Therefore, the researches often perform a load frequency sweep in this kind of tests to obtain the crack growth rate for different frequencies using only one specimen. This is a clear advantage when compared to classical fatigue tests in which it is necessary to

keep the same frequency until the rupture of the specimen in order to obtain a valid fatigue life.

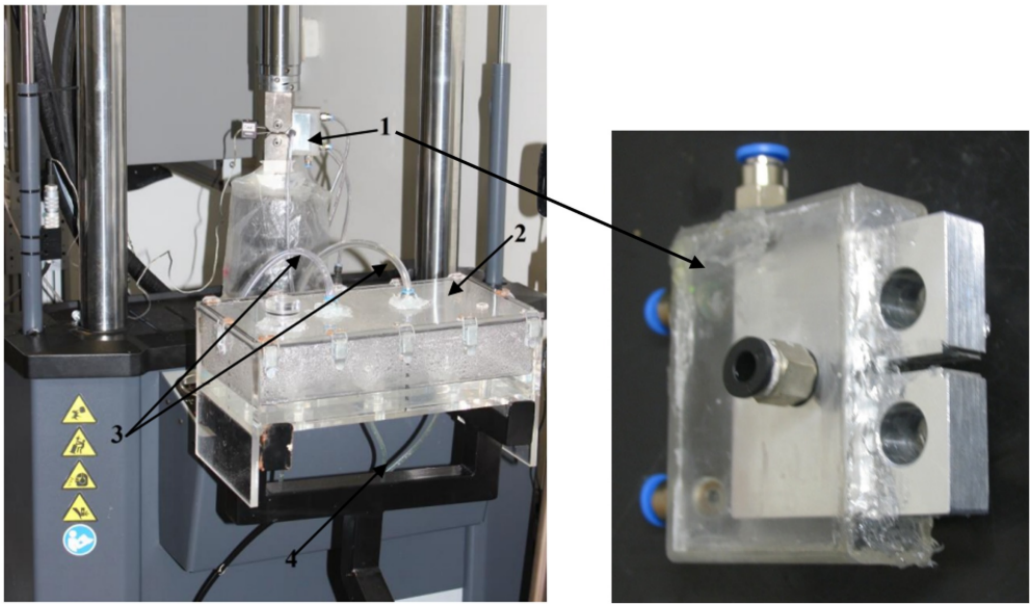

Figure 2.8: Corrosion fatigue testing rigs based on fracture mechanics [64].

Another possible approach is to use a classical fatigue testing machine with smooth specimens. In this approach, corrosion cells are typically designed to expose only the middle section of the specimen to the corrosive environment immersed. The extremities of the specimen are usually kept outside of the corrosion chamber so they can be attached to the fatigue machine grips. In order to obtain more information about the phenomena related to the corrosion fatigue degradation, these cells are normally equipped with electrodes. The electrodes and the specimen are connected to a potenciostat, which performs the electrochemical measurements. A schematic representation is shown in Fig. 2.9.

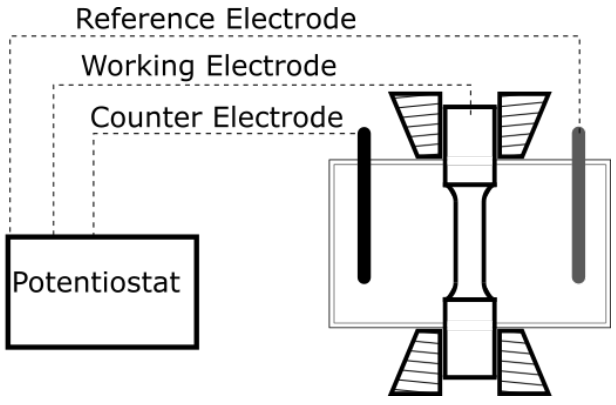

Figure 2.9: Schematic representation of an experimental setup used on corrosion fatigue tests.

Many authors [15, 17–20, 53] carried out some kind of electrochemical monitoring during the corrosion fatigue experiments. Electrochemical Impedance Spectroscopy (EIS) and potential monitoring has proven to be capable of identifying impedance changes related to passive film rupture for stainless steels [17]. However, only a few of them [18–20] were able to measure the

variation of a electrochemical properties, *e.g.* corrosion potential or corrosion current, within a loading cycle. Since electrochemical reactions are mainly controlled by the electrochemical potential and pH, some researches performed the experiments with a controlled potential, therefore measuring the corrosion current, meaning the thermodynamically possible reactions were known.

2.4 Mooring line critical load condition

The details of the approach used to calculate the OPB loads presented in this section can be found in Ref. [65].

Among the failures observed in mooring lines, fatigue of chain links subjected to out-of-plane bending (OPB) has been recognized as a critical loading mode at terminations such as fairleads and hawse pipes [5, 6]. The OPB mechanism results from a combination of high pretension level in the mooring chain, along with poor articulation of the fairlead or chain hawse [66]. This loading condition creates a severe stress concentration on the surface that potentially reduces its fatigue life.

Figure 2.10 illustrates the interaction of the mooring chain with the fairlead sheave. Due to the forces acting on the mooring line, a rotation of the fairlead sheave is expected, which causes a rotation of the hatched link relative to the adjacent ones. Another important feature of the problem is the increase of the contact surface area between links due to the proof load applied to the mooring chain, which is a standard procedure during its manufacturing. The enlarged contact area aggravates the frictional forces between adjacent links, resulting in a cantilever-like behavior and out-of-plane bending of the link adjacent to the hatched one.

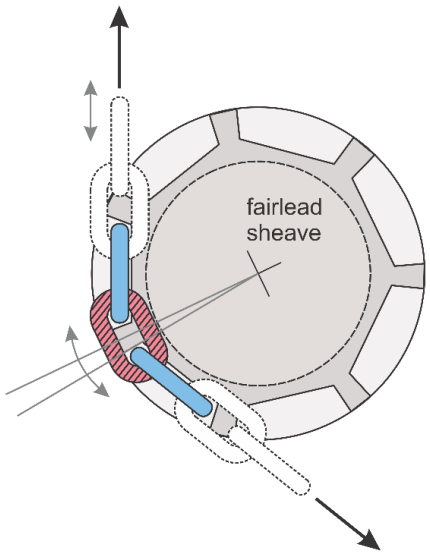

Figure 2.10: Schematics of the fairlead/mooring chain system [65].

In order to mimic the loading acting on the fairlead-mooring chain system, a test bench for fatigue testing of chain samples under out-of-plane bending was designed within the framework of this project. A schematic representation of the loading applied to a chain segment is shown in Fig. 2.11. A 9-link chain segment is first submitted to an axial preload F_H0 in its initial configuration (represented by dashed lines). The central hatched link is then subjected to a cyclic vertical displacement, $V(t)$, resulting in out-of-plane bending of the adjacent links. Positive vertical displacements were imposed to ensure that interlink angles are positive, as typically occurs in the fairlead/mooring chain system.

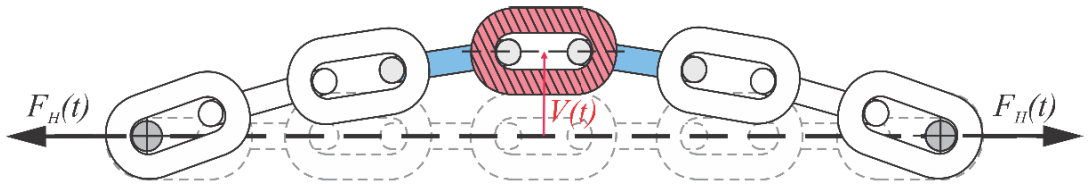

Figure 2.11: Schematics of the loading applied to a chain segment for the reduced scale rig [65].

The layout of the experimental apparatus is shown in Fig. 2.12, where its main components are identified. A 9-link chain is fixed to two flanges. One of them is attached to an axial load cell, which measures the horizontal force, $F_H(t)$, acting on the chain. The other one is attached to a hydraulic jack which is used to apply the preload, F_H0. The vertical displacement of the middle link, $V(t)$, is imposed by the servo-hydraulic actuator of an MTS 322 test system. During the test, the vertical force on the middle link, $F_V(t)$, is measured by the MTS load cell.

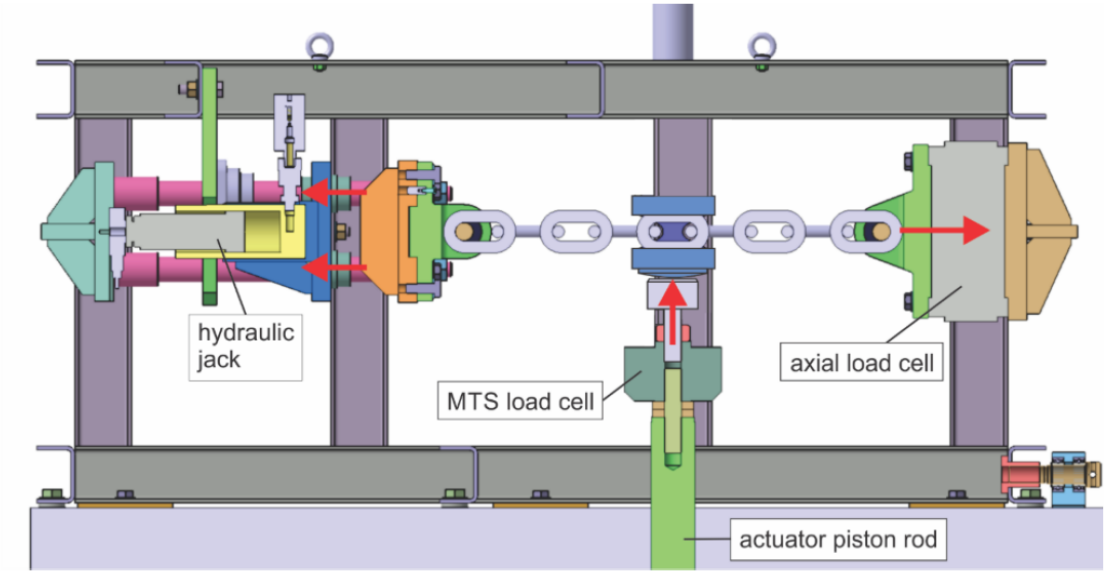

Figure 2.12: Layout of the reduced scale apparatus for fatigue testing of chains under out-of-plane bending [65].

Each test was defined by three parameters: an axial preload, F_H0, the maximum axial force, F_{Hmax}, and the minimum axial force, F_{Hmin}, acting on the chain specimen. The preload was first imposed by the hydraulic jack. The vertical displacement applied to the central link was then adjusted so that the axial force cycled between the maximum and minimum target values.

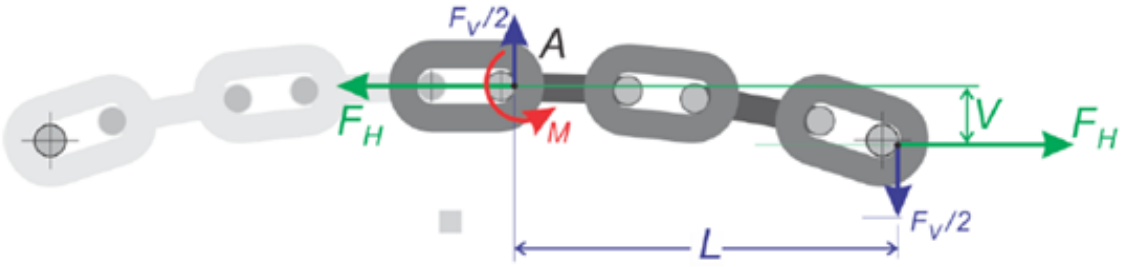

Figure 2.13: Loading on the chain segment [65].

The stress at the hotspot of the chain link is calculated as the sum of the axial and OPB stress contributions:

$$\sigma_{hotspot} = \sigma_{axial} + \sigma_{OPB}. \tag{2.26}$$

And the values of σ_{axial} and σ_{OPB} are defined as follows:

$$\sigma_{axial} = \frac{2F_H}{\pi d^2}, \tag{2.27}$$

$$\sigma_{OPB} = \frac{16L}{\pi d^3}\left(\frac{F_V}{2} - F_H\frac{V}{L}\right), \tag{2.28}$$

where d is the chain diameter. F_H, F_V, L and V are defined as shown in Fig. 2.13.

Seven tests with different levels of preload, F_H0, were investigated (Tab. 2.1). Failure was defined as the total rupture of a link. The loading frequencies of the applied vertical load varied from 1.2 to 2.3 Hz. These frequencies were higher than those typically observed in offshore conditions (0.1 to 0.2 Hz) [9] to allow the testing program to be completed within the project schedule.

For the load conditions tested, the stress contribution due to the OPB was much greater

Table 2.1: Parameters used on the fatigue tests of mooring chains.

Test	F_H0 [kN]	F_{Hmin} [kN]	F_{Hmax} [kN]	F_Vmin [kN]	F_{Vmax} [kN]	V_{min} [mm]	V_{max} [mm]	Cycles to Failure
1	52.0	55.2	109.9	3.0	24.0	12.9	26.3	34323
2	50.0	55.3	109.5	3.3	24.3	16.7	30.2	16409
3	41.0	45.8	81.0	2.5	15.0	13.8	23.8	149698
4	41.0	46.0	90.8	1.8	18.4	11.8	24.3	89332
5	41.0	45.4	99.6	2.2	21.3	15.3	29.1	79321
6	41.0	45.9	71.0	2.8	11.3	10.8	19.2	1000000
7	41.0	45.6	75.8	3.3	13.5	12.2	21.3	1000000

them the stress due to axial loading of the mooring line, as shown in Fig 2.14. Even though the chain operates in tension-tension load condition, it is possible to observe compressive stresses for some of the conditions tested (Fig. 2.14) due to the effects of the out-of-plane bending. The load ratios, defined as the minimum stress divided by the maximum stress, for the conditions tested varied from -0.23 to 0.12. Therefore, it is important to understand the behavior of the material under both positive and negative load ratios.

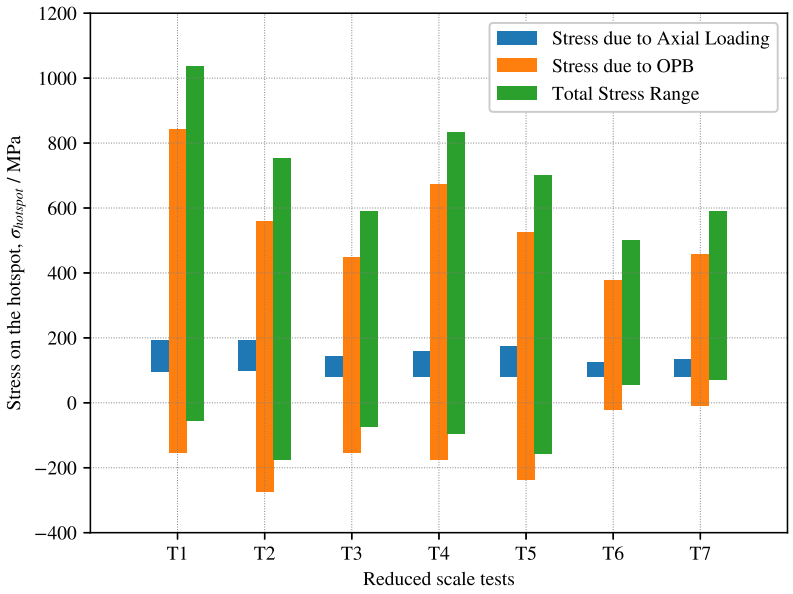

Figure 2.14: Stress levels on the hotspot for the different tests.

Chapter 3 – Experimental Procedures

In this section, the information about the material, as well as, the experimental procedures are outlined. Two sets of experiments were carried out. The first aimed to observe the evolution of the corrosion fatigue degradation for different load conditions. To quantify the degradation, the corroded area was used as a indicative of the electrochemical activity. The second set of tests was performed to assess the evolution of the electrochemical properties of the system during the corrosion fatigue tests. Periodic measurements of corrosion potential and the electrochemical impedance spectroscopy were carried out in this stage. The experimental program regarding the monitoring of electrochemical properties of the system submitted to corrosion fatigue condition was designed and performed at *Instituto Superior Técnico* (IST - University of Lisbon).

3.1 Material

The material used in the preliminary studies is a grade R4 steel supplied by *Companhia Brasileira de Amarras Brasilamarras*. According to the International Association Classification Societies (IACS), this material must contain a minimum of 0.2% of molybdenum and its mechanical properties must satisfy the following requirements: minimum yield stress of 580 MPa, minimum tensile strength of 860 MPa and minimum elongation of 12% [67]. The exact chemical composition of this grade R4 steel is property of *Vicinay Cadenas, S.A.* and cannot be provided due to a confidentiality agreement made with the supplier. To meet the requirements of the standard IACS - W22 [67], the material was quenched in water, after heating at 890°C for 30 min, and then tempered in water, after heating at 650°C for 60 min. The quasi-static monotonic tensile test is shown in Fig. 3.1, where the "x" at the end of the curve represents the rupture of the specimen. The monotonic properties are summarized in Table 3.1.

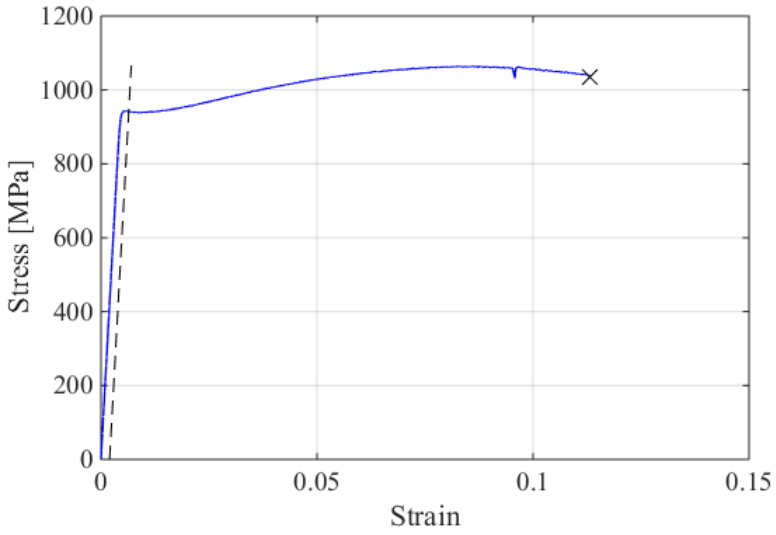

Figure 3.1: True Stress and True Strain obtained from quasi-static monotonic tensile test.

Table 3.1: Static properties of the material.

	Youngs Modulus [GPa]	Yield Stress [MPa]	Ultimate Stress [MPa]	Brinell Hardness [HBW 2.5/187.5]
R4 Steel	210	940	1060	294

To characterize the microstructure of the material, a metallographic specimen was ground up to 1000 grit, polished using alumina and etched with nital 3%. The micrography of the cross section of the bar, perpendicular to the load direction, is shown in Fig. 3.2. A martensite microstructure composed was observed.

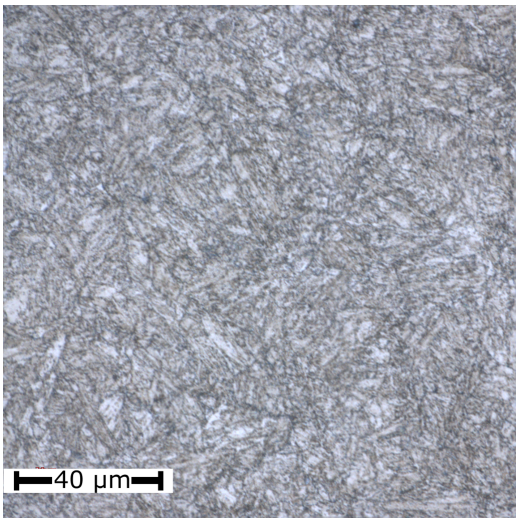

Figure 3.2: Microstructure of the material (grade R4 steel).

3.2 Corrosion Fatigue Tests for Degradation Analysis

Two geometries were used in the section. The first part of the work deals with cylindrical working section, while the second part uses conical working section specimens.

The cylindrical specimens with a working section length of 10 mm and diameter of 6 mm were machined from round bars (3.3a). After the machining, the surfaces were abraded at the circumferential direction with emery paper up to grade 1000 and then degreased with alcohol and dried with air jet.

In order to evaluate the effects of different stress level on the corrosion behavior of the material, a new specimen was designed. The new design presents a trunk conical working section, with the diameter varying from 6 mm to 4 mm (3.3b). This new geometry allowed a better comparison between stress level and corrosion morphology since a range of stresses is exposed to the corrosive environment for the same period.

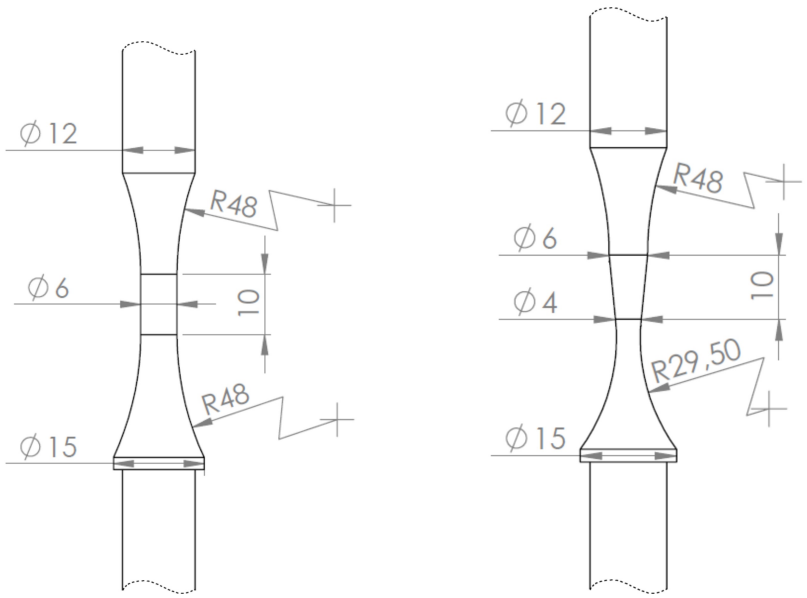

Figure 3.3: (a) Classical cylindrical specimen and (b) specimen with trunk conical working section.

The arithmetic roughness, R_a, on the specimen axis direction was measured using a confocal microscope (Olympus OLS 4000 LEXT). The typical surface roughness value was $R_a = 0.07$ μm, considering the 1000 grit finish in the circumferential direction. This value is significantly lower than 0.2 μm, which is the roughness stipulated by the standard ASTM E 466 [68] for fatigue in-air tests and 0.4 μm stipulated by ASTM F 1801 [69] for corrosion fatigue testing of metallic implant materials. To the best of the author's knowledge, there is not a standard concerning the surface roughness limit for corrosion fatigue tests of steels in artificial seawater.

A corrosion cell was developed to allow *in-situ* corrosion fatigue testing. The cell consists

of an acrylic chamber which surrounds the working section of the specimen. Both ends of the specimen are clamped to a servo-hydraulic fatigue testing machine (MTS 810). A saline solution was prepared using deionised Millipore water and pure NaCl (3.5 wt% NaCl by Sigma–Aldrich). The schematic representation of the corrosion fatigue test setup is shown in Fig. 3.4.

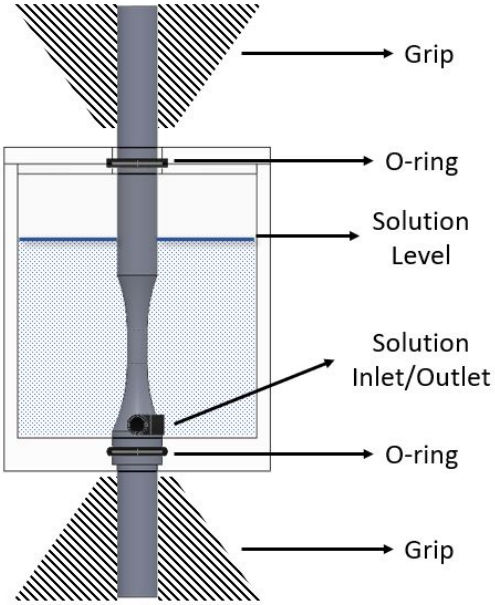

Figure 3.4: Schematic representation of the corrosion fatigue apparatus.

The corrosion fatigue tests were performed under load control regime with sinusoidal waveform and 1.0 Hz load frequency. Fully reversed loads, $R = -1$, and tests in the presence of mean stress, $R = 0.1$, were performed. The load ratio, R, is defined as:

$$R = \frac{S_{min}}{S_{max}}, \tag{3.1}$$

where S_{min} and S_{max} are the minimum and maximum nominal applied load, respectively.

In-air fatigue tests were also performed for comparative purposes. The stop criterion for the fatigue tests was defined as the complete rupture of the specimen. Specimens that did not fail after 2 million cycles were identified as "runout". All tests were carried out at room temperature.

After the corrosion fatigue tests, the specimens were submitted to a confocal microscopic inspection to assess the level of corrosion degradation. The specimens were cleaned in ultrasonic bath with acetone and ground at the longitudinal direction with 4000 grit mesh. This procedure helped to achieve an overall polished surface but preserved the corrosion pit marks and nucleated cracks. The fraction of corroded area was used as a parameter. Even though this parameter alone cannot fully describe the degradation mechanisms on the corrosion fatigue process, this

measurement was used only as an indicative of the intensity of the electrochemical activity.

The identification of the corroded zones was performed automatically, using a Python script developed for this purpose. The identification processes consists of 3 stages: *i)* The image colouring is modified to greyscale (Fig. 3.5a). *ii)* A grey threshold of 0.3 is applied - where 0 corresponds to white and 1.0 to black - and the darker areas are identified as corroded regions. The fraction of corroded area is calculated in this stage (Fig. 3.5b) as the ratio of darker pixels over the total pixels of the image. *iii)* The identified zones are overlaid on the original image to validate the process (Fig. 3.5c). In order to obtain a better estimation of the fraction of corroded area, four images with the area of 640 μm x 640 μm were used for each load condition and the mean corroded area was calculated. The standard deviation was used as a dispersion measure.

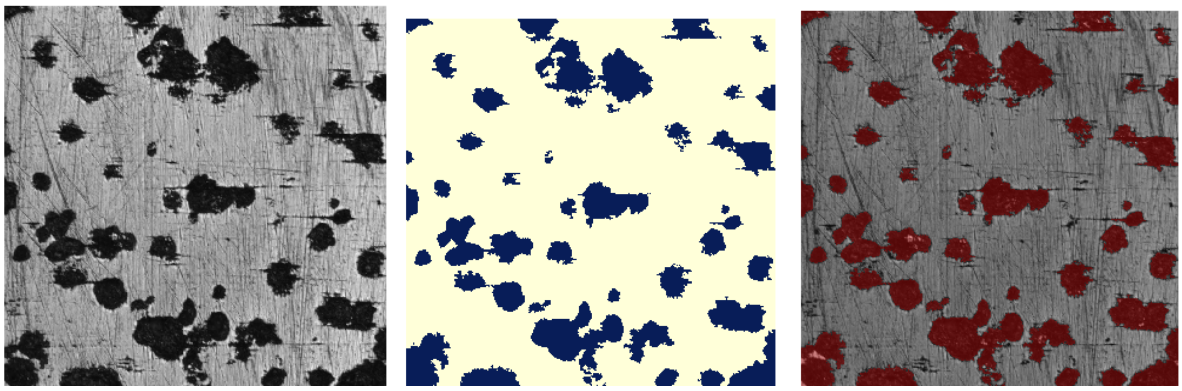

(a) **(b)** **(c)**

Figure 3.5: Stages of the corrosion level identification process. (a) The image coloring is modified to greyscale, (b) the total corroded area is calculated and (c) the validation stage.

3.3 Corrosion Fatigue Tests With Electrochemical Measurements

A special corrosion cell was developed with a three-electrode configuration: a reference electrode (R.E.), a platinum counter electrode (C.E.) and the steel specimen as working electrode (W.E.) to allow electrochemical measurements of *in-situ* corrosion fatigue testing in simulated seawater (3.5 wt% NaCl solution). The electrodes were connected to an Interface 1000 potentiostat (Gamry Instruments). The corrosion cell also has a solution inlet and outlet which allows solution circulation during the tests. A picture and a schema of the corrosion fatigue test setup are shown in Fig. 3.6.

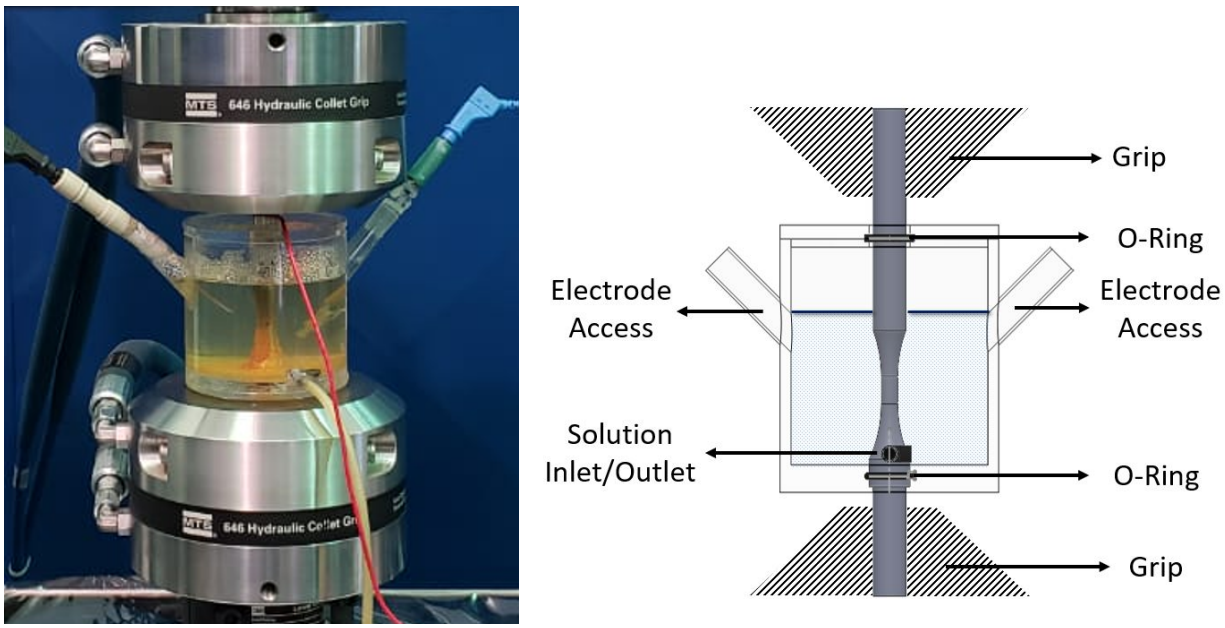

(a) **(b)**

Figure 3.6: (a) Picture and (b) schematic representation of the experimental setup used on corrosion fatigue tests with electrochemical monitoring.

For this setup, the corrosion fatigue tests were performed under fully alternated load-controlled regime. A sinusoidal waveform, 1.0 Hz frequency and stress amplitudes from 350 MPa to 550 MPa were applied. All tests were carried out at room temperature.

The full fatigue experimental program is depicted in Table 3.2 for the fully alternated loads and Table 3.3 for the tests in the presence of mean stress, where S_a is the nominal stress amplitude.

Table 3.2: Fatigue tests carried out under fully alternated loading ($R = -1$).

ID	Environment	S_a [MPa]	S_{min} [MPa]	S_{max} [MPa]	N_f
IA1	In-Air	750	-750	750	3814
IA2	In-Air	700	-700	700	21899
IA3	In-Air	670	-670	670	88000
IA4	In-Air	650	-650	650	58622
IA5	In-Air	650	-650	650	140260
IA6	In-Air	625	-625	625	24290
IA7	In-Air	625	-625	625	79394
IA8	In-Air	600	-600	600	2000000*
IA9	In-Air	500	-500	500	2000000*
IA10	In-Air	450	-450	450	2000000*
CF1	Seawater	550	-550	550	42264
CF2	Seawater	500	-500	500	66018
CF3	Seawater	500	-500	500	58622
CF4	Seawater	500	-500	500	55750
CF5	Seawater	500	-500	500	48990
CF6	Seawater	450	-450	450	104300
CF7	Seawater	400	-400	400	101717
CF8	Seawater	400	-400	400	91645
CF9	Seawater	375	-375	375	185648
CF10	Seawater	350	-350	350	156543
CF11	Seawater	350	-350	350	198571
CF12	Seawater	300	-300	300	215858
CF13	Seawater	250	-250	250	489734

Table 3.3: Fatigue tests carried out under the presence of mean stress ($R = 0.1$).

ID	Environment	S_a [MPa]	S_{min} [MPa]	S_{max} [MPa]	N_f
IAM1	In-Air	435	97	968	21713
IAM2	In-Air	435	97	968	51870
IAM3	In-Air	402	89	893	127286
IAM4	In-Air	369	82	819	2000000*
IAM5	In-Air	335	74	744	1307099
CFM1	Seawater	435	97	968	13648
CFM2	Seawater	369	82	819	38208
CFM3	Seawater	335	74	744	47478
CFM4	Seawater	302	67	670	117990
CFM5	Seawater	251	56	558	128509
CFM6	Seawater	235	52	521	182955
CFM7	Seawater	201	45	447	215858
CFM8	Seawater	168	37	372	489734

The electrochemical measurements were carried out in blocks of 5000 s at the free electrochemical potential. Each block consisted of the corrosion potential monitoring followed by two EIS measurements. The corrosion potential was recorded periodically during the experiment against a saturated Ag/AgCl reference electrode ($E_{(Ag/AgCl)} = 0.197$ V) with a sampling rate of 100 Hz. The E_{corr} response progressions were analysed in order to monitor the evolution of the degradation on the metallic surface. EIS measurements were performed from 10^4 Hz to 10^{-2} Hz, 10 mV_{rms} sinusoidal perturbation, and the data were checked for steady-state condition by repeating every spectrum. The first spectrum was carried out with only 4 points per decade whereas the second was performed with 7 points per decade. This arrangement allowed to carry out both spectra in a shorter time interval. The block of measurement is summarised in Table 3.4.

Table 3.4: Electrochemical measurements during the corrosion fatigue tests

Measurement	Duration	Description
Corrosion Potential	600 s	OCP monitoring at a sampling frequency of 100 Hz.
EIS	1200 s	4 points per decade from 10^4 Hz to 10^{-2} Hz.
EIS	2100 s	7 points per decade from 10^4 Hz to 10^{-2} Hz.
Delay	1100 s	Wait until 5000 s and start a new block of measurements.

In order to be able to correlate the different responses of the corrosion potential with the degradation state of the specimen, a new set of corrosion fatigue tests were carried out. The tests were performed under a stress amplitude of $S_a = 500$ MPa, at a frequency of 1.0 Hz. Each

test was stopped at selected lives of: 5000, 20000, 35000, 45000 and 64440 cycles. The later was carried out until the rupture. An inspection of the corroded surface on confocal microscope was performed for each test.

The EIS study was focussed on the effect of cyclic loading on the electrochemical behaviour of the material. The measurements were compared to a non-loaded specimen exposed to identical corrosive solution for the same time length. The equivalent electric circuit is shown in Fig. 3.7, where R_E and R_{CT} are the electrolyte and the charge-transfer resistances, respectively, and the Constant Phase Element (CPE) was used to simulate the non-ideal behaviour of the double layer capacitance formed on the interface between the specimen and the electrolyte. The measured EIS data were fitted using the software ZView©, version 2.7 (Scribner Associates, Inc., NC, USA).

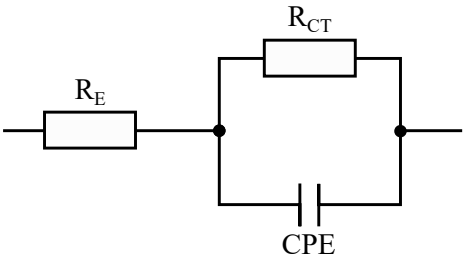

Figure 3.7: Equivalent electrical circuit used to model the EIS spectra.

3.4 Setup Validation

As a first step, EIS tests were carried out to ensure that the electric contact between the specimen and the fatigue testing machine does not jeopardize the electrochemical measurements. No load was applied to the specimen. A first test was carried out with the specimen connected to the fatigue testing machine. A second measurement was performed with the specimen completely isolated from the fatigue test machine, and a third test was carried out with the specimen connected to the fatigue machine again. The three measurements generated almost identical results, as shown in Fig. 3.8. Therefore, it was assumed that the electrical contact between the specimen and the fatigue testing machine does not interfere with the electrochemical measurements.

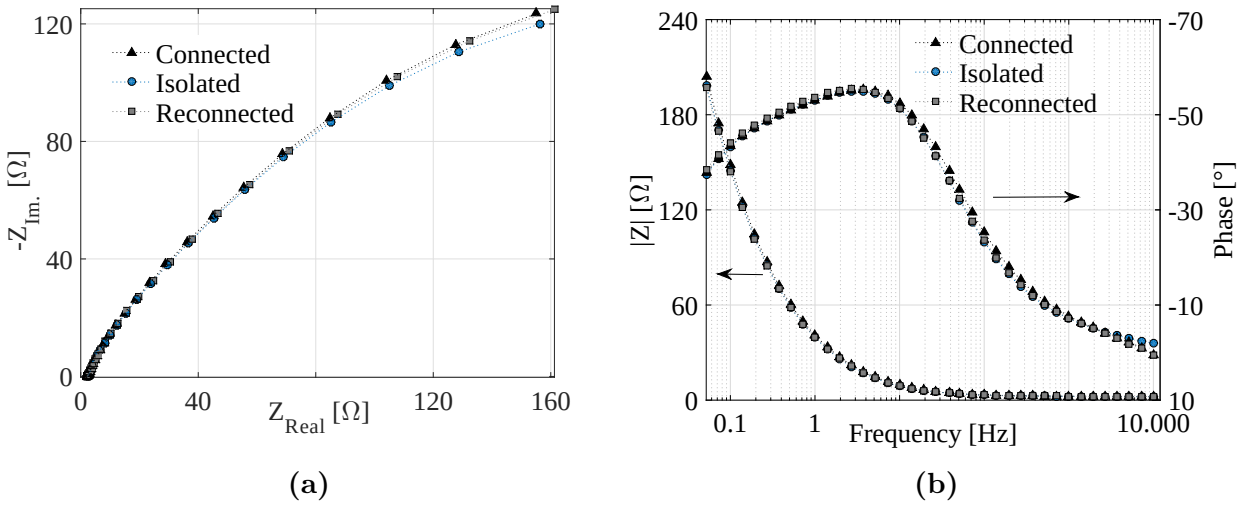

Figure 3.8: EIS measurements made to evaluate the influence of electrical contact between the specimen and the fatigue testing machine. (a) Nyquist plot and (b) Bode plot [70].

The effects of solution circulation on the corrosion potential response during the corrosion fatigue tests were also evaluated. In this preliminary test, the corrosion potential was monitored during the application of a fully reversed cyclic stress of 550 MPa of amplitude and 1.0 Hz load frequency. The test was performed without circulation of solution for 200 s. In the sequence, the solution circulation was turned on. These two conditions can be easily distinguished in Fig. 3.9a. For the condition of stagnated solution, it was observed a clean sine wave signal as the corrosion potential response, with the same frequency as the mechanical load, and a decreasing mean value (Fig. 3.9b). The decreasing mean value of the E_{corr} is explained by oxygen depletion in the neighbourhood of the metallic interface, which reduces the cathodic rate and shifts the potential to more negative values. As soon as the circulation started, a rapid increase in the corrosion potential was noticed. This is expected, considering that with electrolyte circulation, the oxygen supply to the metallic surface is facilitated, which increases the corrosion potential. A detailed examination of the E_{corr} sign after 200 s revealed a noise level greater than the oscillations caused by the cyclic stress, as shown in Fig. 3.9c. In order to have a better understanding of the effects of cyclic loads on the E_{corr} response, it was decided, in a first moment, to carry out the corrosion fatigue tests without solution circulation.

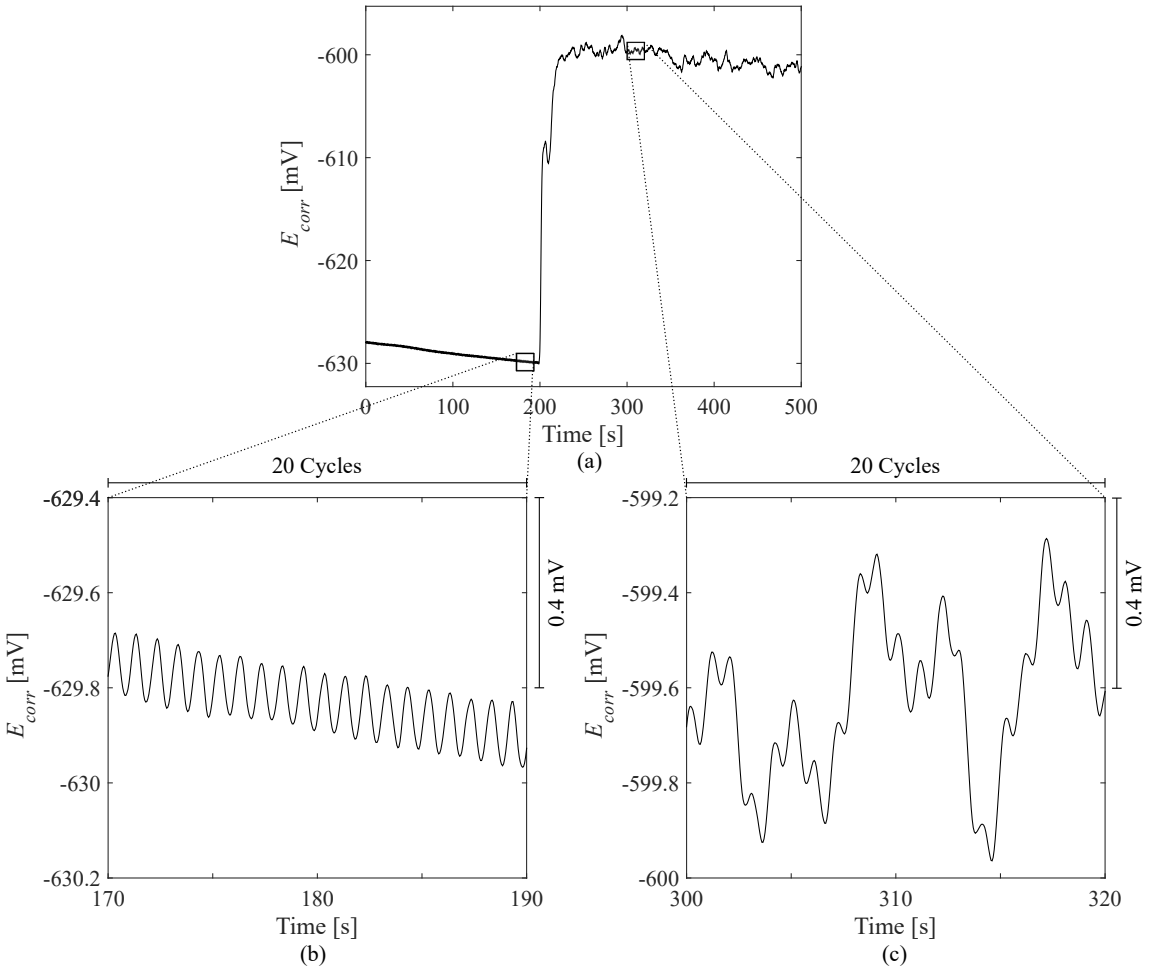

Figure 3.9: Preliminary tests to evaluate the effects of solution circulation on the corrosion potential response.

Chapter 4 – Results

In this chapter, the corrosion fatigue and in-air fatigue results are presented. A post-failure inspection of the specimens was performed and a quantitative analysis of the corrosion degradation due to corrosion fatigue was carried out using the fraction of corroded area as an index. The morphology of the corroded surfaces were also evaluated using a Scanning Electron Microscope (SEM). The second set results shows the evolution of the electrochemical properties of the system during the corrosion fatigue tests. The information about the electrochemical response of grade R4 steel under fatigue load in the literature is non-existent, to the best of the author's knowledge.

4.1 In-air fatigue and corrosion fatigue tests

The fatigue curves comparing both environmental conditions for the tests under fully reversed loads ($R = -1$) and for the tests in the presence of mean stress ($R = 0.1$) are presented in Fig. 4.1a and Fig. 4.1b, respectively. The arrows represent tests that did not fail after 2 million cycles. The corrosive environment played an important role in both load conditions. The change in slope observed for the tests in seawater environment means that the corrosive media have an ever-increasing detrimental effect towards lower stress amplitudes on the observed corrosion fatigue life.

The intersection formed by the curves for the in-air and seawater environment can be understood as a threshold. For amplitudes above this limit, the observed fatigue lives for the in-air condition and in seawater environment should be similar, and the failure will be dominated by the mechanical component. This phenomenon can be explained by the shorter duration of the tests carried out at higher stress amplitudes. The highest amplitude corrosion fatigue test, $S_a = 435$ MPa, carried out in the presence of mean stress (Fig. 4.1b) resulted in fatigue life of 13648 cycles. This means an immersion period of less than 5h, considering that the applied load frequency was 1.0 Hz and that the specimen was immersed 1h before the load application.

Comparing the fatigue lives at the lower stress amplitudes can be more challenging. The effects of the corrosive environment are so severe that the most part of the amplitudes used on the corrosion fatigue tests would result on runouts for the in-air condition. A rough estimation

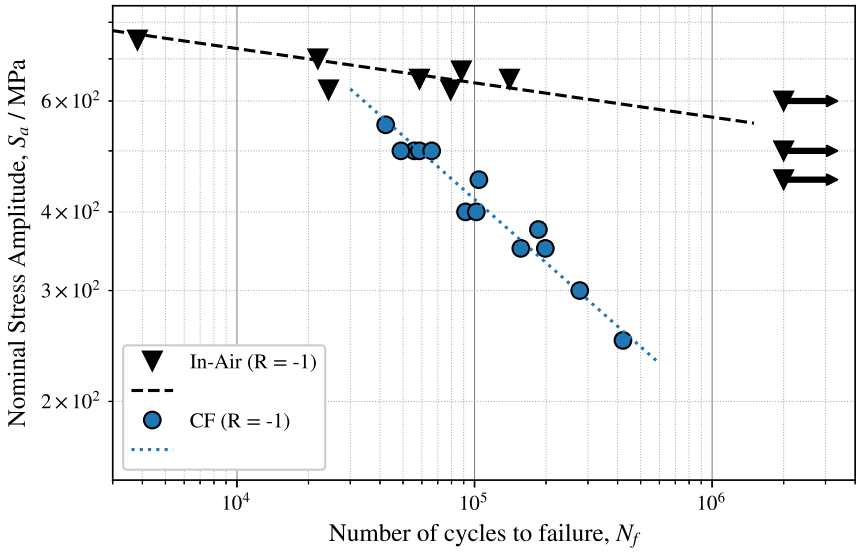

(a)

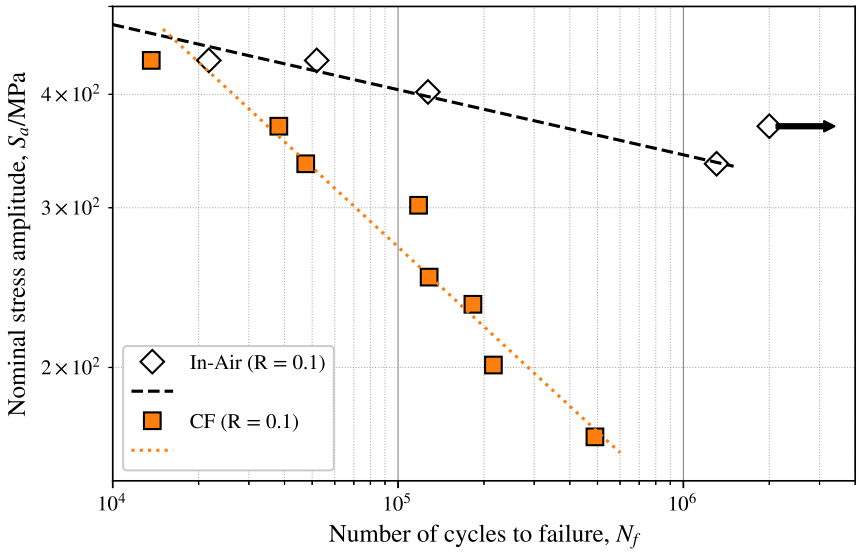

(b)

Figure 4.1: Fraction curves for (a) $R = -1$ e (b) $R = 0.1$ load ratios.

of the fatigue life reduction can be performed by extrapolating the obtained fatigue curves, as shown in Fig. 4.2a for $R = -1$ and Fig. 4.2b for $R = 0.1$. Using this estimation, the life reduction can be greater than 6 orders of magnitude for the tests performed under fully reversed loading and greater than 5 orders of magnitude for the tests carried out in the presence of mean stress.

The same set of results are rearranged to allow a better visualization of the effect of the mean stress on the observed fatigue life for the in-air condition (Fig. 4.3a) and corrosion fatigue (Fig. 4.3b). For the same load amplitude, the presence of the mean stress causes a reduction of the number of cycles to failure. The effects of the positive load ratio (Fig. 4.3b) are particularly important in the corrosion fatigue experiment. For this condition, the specimen is always under

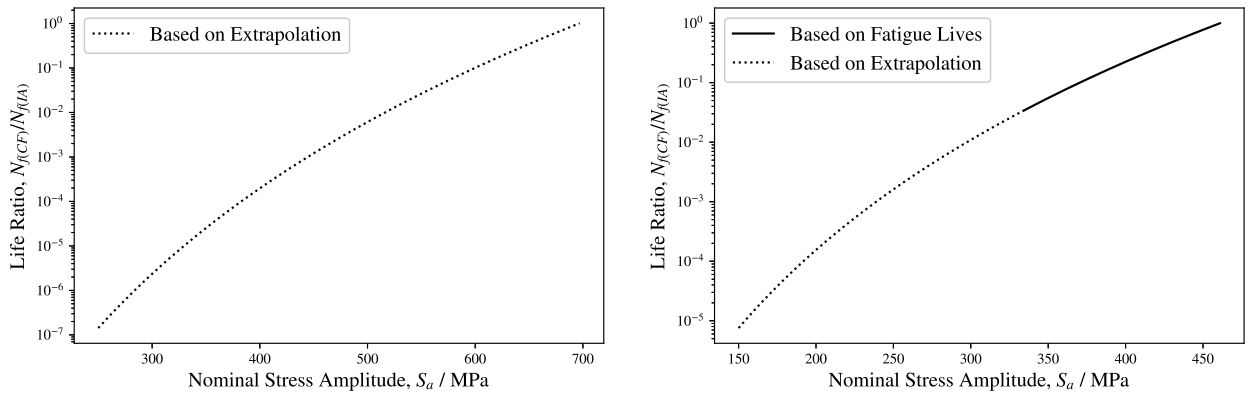

(a) **(b)**

Figure 4.2: Fatigue life ratios between in-air condition, $N_{f(IA)}$ and corrosion fatigue, $N_{f(CF)}$, considering (a) $R = -1$ e (b) $R = 0.1$ load ratios.

traction, causing the nucleated cracks to stay open during the whole loading cycle and exposed to the corrosive environment. This phenomenon is not observed in the fully reversed tests, where the cracks close during the compressive part of the load.

The complete set of fatigue tests (in-air and corrosive environment) is presented in Fig. 4.4. The Smith-Watson-Topper (SWT) [71] parameter was used to take into account the effect of mean stress on the fatigue life. This parameter has been already used in corrosion fatigue studies [72] in the presence of mean stress and showed good results when compared to the experimental data. The SWT parameter in conditions where macroscopic plasticity is not observed can be defined as:

$$SWT = \sqrt{S_a S_{max}}, \tag{4.1}$$

where S_a is the nominal stress amplitude and S_{max} is the maximum nominal stress.

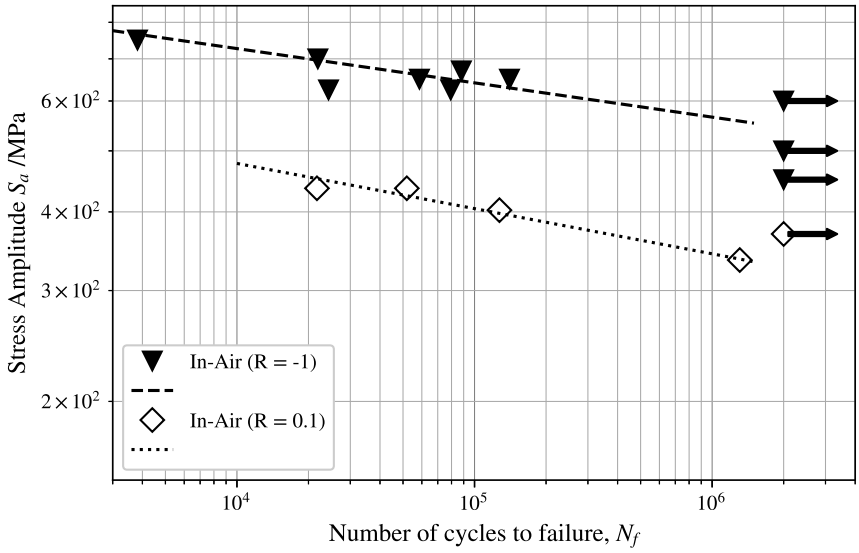

(a)

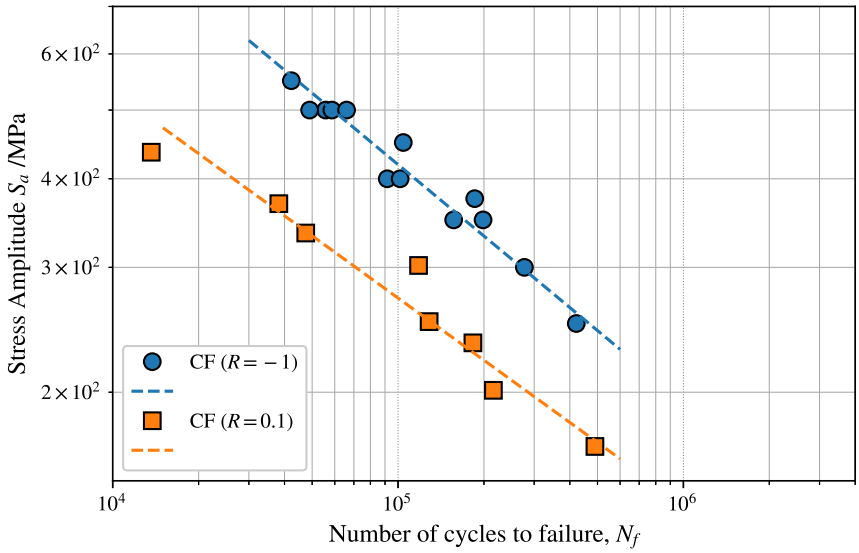

(b)

Figure 4.3: Fatigue curves for (a) in-air condition e (b) corrosion fatigue.

The data shown in Fig. 4.4 reveals that the SWT parameter is able to capture the mean stress effect for corrosion fatigue environmental condition within a factor-of-two. For the in-air condition, the SWT parameter tends to generate optimistic predictions for the test in presence of mean stress. All the results stayed within a factor-of-four for this condition.

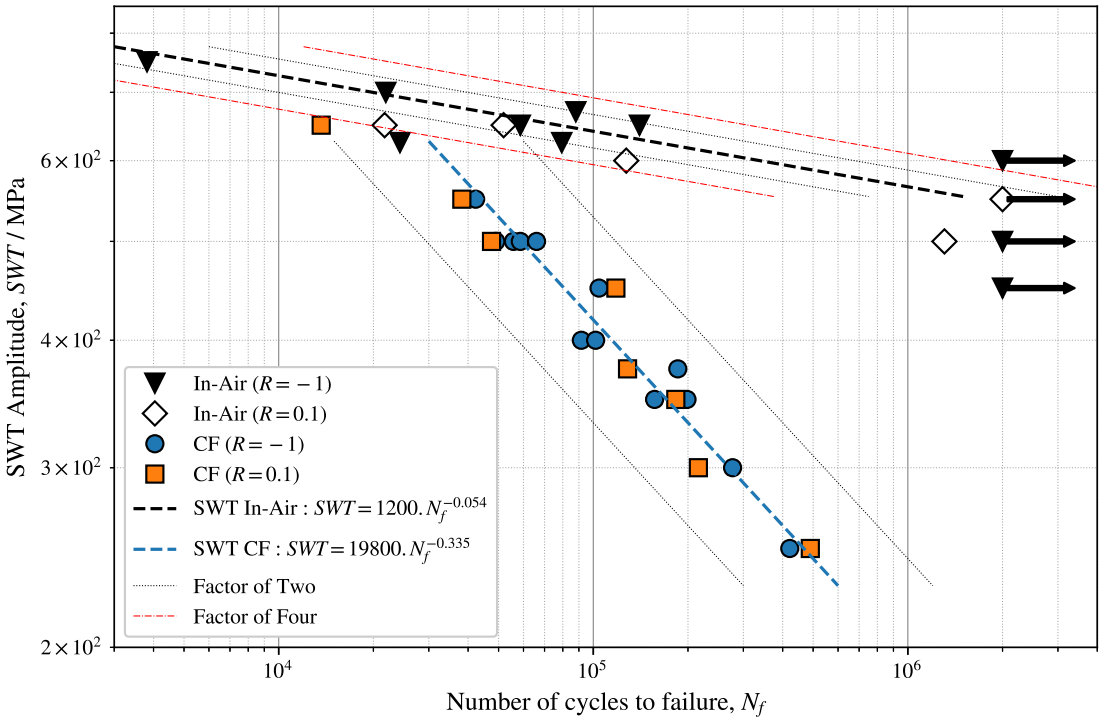

Figure 4.4: In-air and corrosion fatigue (CF) curves using the SWT parameter.

4.1.1 Corrosion level quantitative analysis for cylindrical specimens

The corrosion levels obtained for $R = -1$ and $R = 0.1$ load ratios are shown in Fig. 4.5a and Fig. 4.5b, respectively. The immersion period for each test is indicated on top of the respective marker. The SWT parameter was used to describe the tests performed in the presence of mean stress. For the fully reversed condition, it is possible to observe a positive correlation between the fraction of corroded area and the stress amplitude up to approximately 350 MPa. Above this threshold, the fraction of corroded area decreased abruptly. For the tests carried out in the presence of mean stress, a high scattering and no clear correlation was observed. It is noteworthy that the duration of the immersion test, with no mechanical load applied, and the duration of the tests submitted to 350 MPa for both load ratios are quite similar, however, the fraction of the corroded area increased significantly in the presence of mechanical load. This behavior highlights the synergistic nature of the corrosion fatigue phenomenon.

For higher stress amplitudes, the corrosion level does not seem to be influenced by the applied mechanical load. In this condition, the immersion times are shorter due to the lower fatigue lives. This behavior was studied by Duquette & Uhlig [73]. They observed that initial pit formation is not a requirement for corrosion fatigue. Evidence from their research suggested that the applied stress level determines whether cracks develop from pits or from slip bands. At high stress levels, slip bands form quickly with insufficient time for pit formation to take place; hence slip-band cracking dominates. Furthermore, after a crack is nucleated, the anodic

region shifts from the specimen's surface to the interior of the crack [74] generating a cathodic region around the crack. This behaviour causes a high corrosion rate on the interior of the crack decreasing the overall corrosion rate on the surface of the specimen.

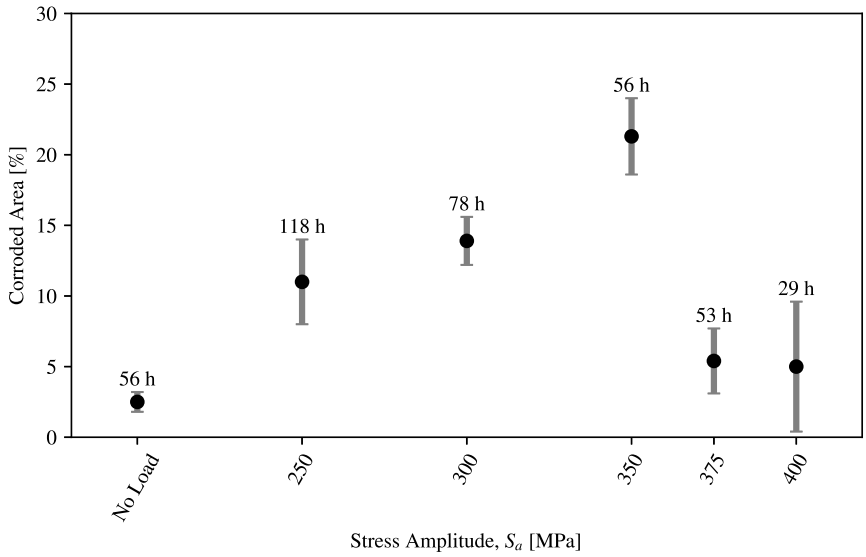

(a)

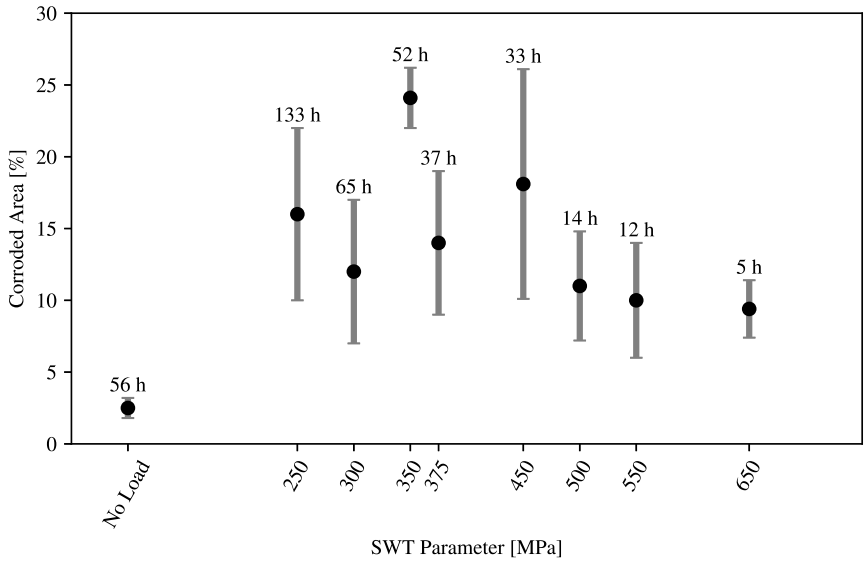

(b)

Figure 4.5: Fraction of the corroded area for (a) $R = -1$ e (b) $R = 0.1$ load ratios.

Higher stresses cause lower lives and, consequently, lower immersion periods which brings some limitations to this type of analysis. Both the applied stress and the immersion period can play an important role on the fractions of corroded area making harder to analyse the real effect of the applied stress on the evolution of corrosion on the specimens. To overcome this limitation, the new specimen's geometry, with a conic working section was used. With this new geometry, different stress levels are submitted to the corrosive environment for the same duration, which allows a more precise correlation between the applied stress amplitude and the level of corroded

area, as described below.

4.1.2 Corrosion level quantitative analysis for trunk conical specimens

The stress distribution on the trunk conical specimen is shown in Fig. 4.6, where 1.0 corresponds to the nominal tension calculated at the minimal radius of the working section. After the rupture, the working section of the specimen was scanned in microscope. A typical corroded surface as well as the image after the corrosion identification routine are also shown in Fig. 4.6.

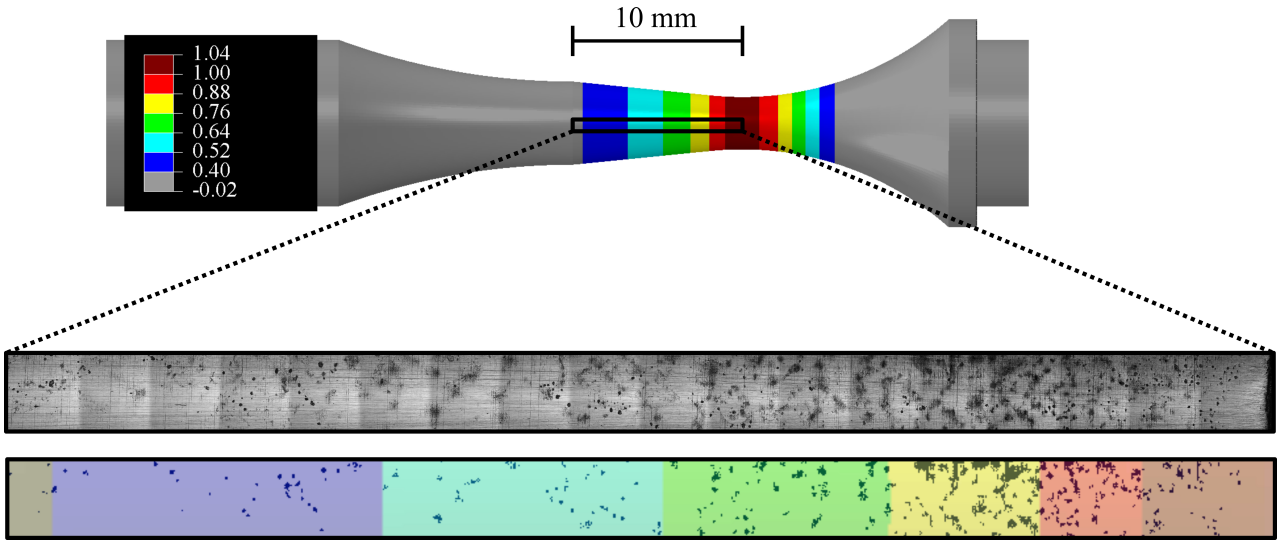

Figure 4.6: Stress distribution on the trunk conical working section and typical corrosion distribution on the inspection area.

The trunk conical section specimens were tested under nominal loads of $SWT_{nom} = 400$ MPa and $SWT_{nom} = 500$ MPa (calculated at the smaller radius of the conical section), generating fatigue lives of 124388 cycles (35 h) and 69819 cycles (20 h), respectively. The quantitative evaluation of the corrosion levels was carried out in a similar way to that performed on cylindrical section specimens. The results obtained for both tests are shown in Fig 4.7a and Fig 4.7b, respectively. The rough images and identified corroded areas at selected distances from the rupture are shown in Fig. 4.8 for both load conditions.

Despite the different immersion periods, both loading conditions generated similar average levels of corroded area along the evaluated section: 7.2% for $SWT_{nom} = 400$ MPa and 7.0% for $SWT_{nom} = 500$ MPa. This phenomenon can be explained by the difference in applied stress of the two samples. The sample that was immersed for less time was subject to higher levels of mechanical stress and vice-versa. In this case, it is verified once again that both the applied stress and the immersion time contribute to the evolution of the corroded area on the surface of the specimens.

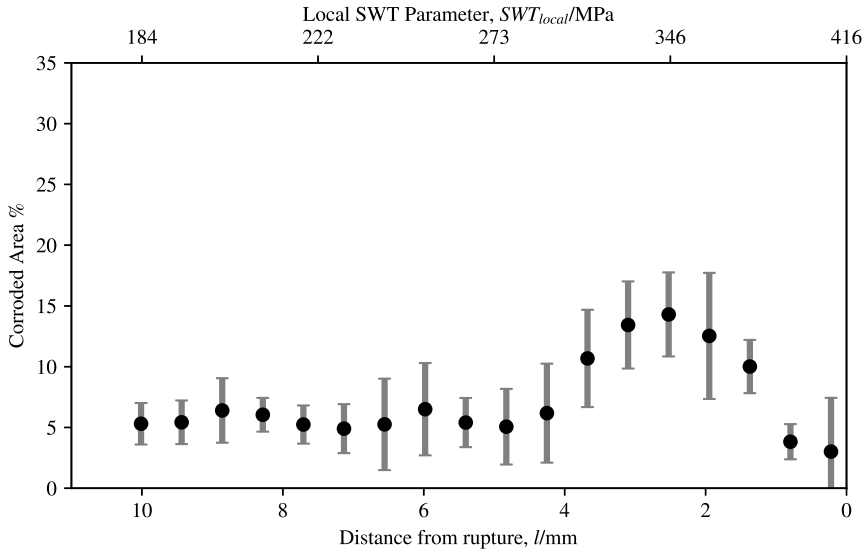

(a)

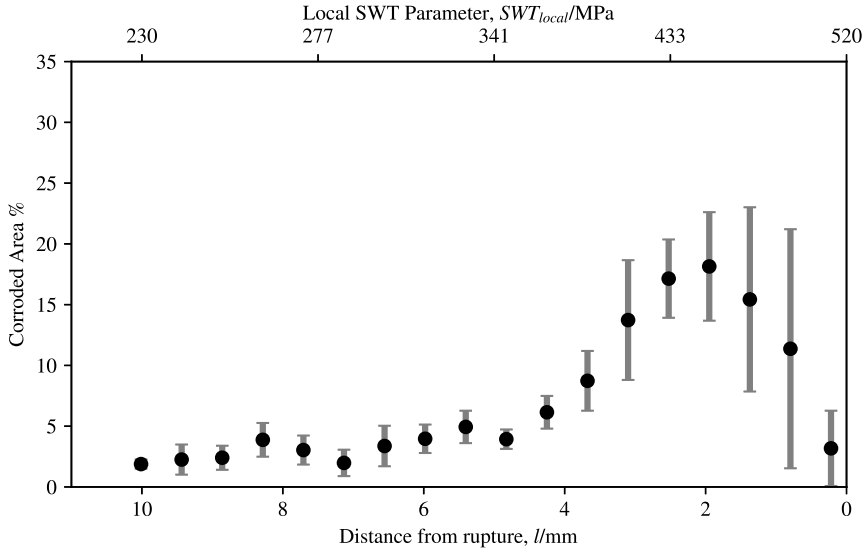

(b)

Figure 4.7: Corroded area as a function of stress levels for trunk conical specimens under (a) $SWT_{nom} = 400$ MPa (35 h of immersion) and (b) $SWT_{nom} = 500$ MPa (20 h of immersion).

As for the variation of corrosion levels along the analyzed region, it is observed that the fraction of corroded area passes through a maximum value in the region of higher stresses, however, the stress values that generate maximum levels of corrosion are different for each condition evaluated. It is also possible to observe that the maximum corroded area takes place at approximately 2 mm from the rupture zone of the specimen for both loading conditions. This behavior indicates that the decrease in the corroded area in the higher stress region may be related to the cathodic zone formed around the main crack, and not to the stress level itself. In this case, the formation of the crack must have occurred before the growth of corrosion defects in that location.

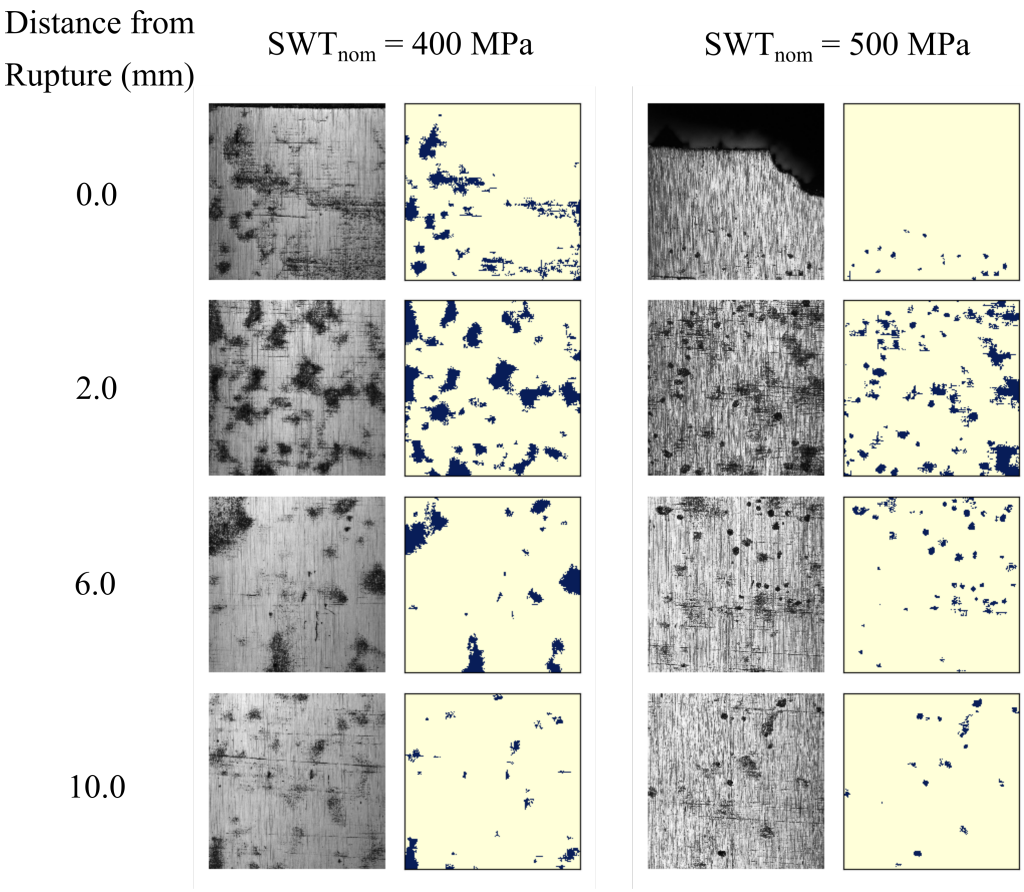

Figure 4.8: Rough images and identified corroded areas at selected distances from the rupture for nominal amplitude of (left) $SWT_{nom} = 400$ MPa and (right) $SWT_{nom} = 500$ MPa.

In order to exclude the effects of a macrocrack on the corroded area fraction measurements, a new fatigue corrosion test was performed, in which the specimen was removed before the initiation of a macrocrack. In this new experiment, the conical specimen was subjected to a nominal load of $SWT_{nom} = 500$ MPa for 7,000 cycles. This value corresponds to 10% of the observed life for the same load condition. A frequency 10 times lower (0.1 Hz) was used, thus the immersion time was similar to the test carried out until failure. The fraction of corroded area observed in this experiment is shown in Fig. 4.9. After the test, the specimen was checked on microscope and no macrocrack was detected.

When no macrocracks were formed on the specimen, the corroded area fraction increases with the mechanical load amplitude. Thus, the decrease in the fraction of corroded area observed in Fig. 4.9 is caused by the presence of a cathodic zone developed around the main crack.

It was observed that higher stress amplitudes produce higher corroded areas until a macrocrack is nucleated. After the crack has nucleated, its interior becomes locally anodic compared to crack's vicinity. This phenomenon caused less apparent corrosion on the higher stress amplitude zone for the tests carried out with the trunk conical specimens up to the failure.

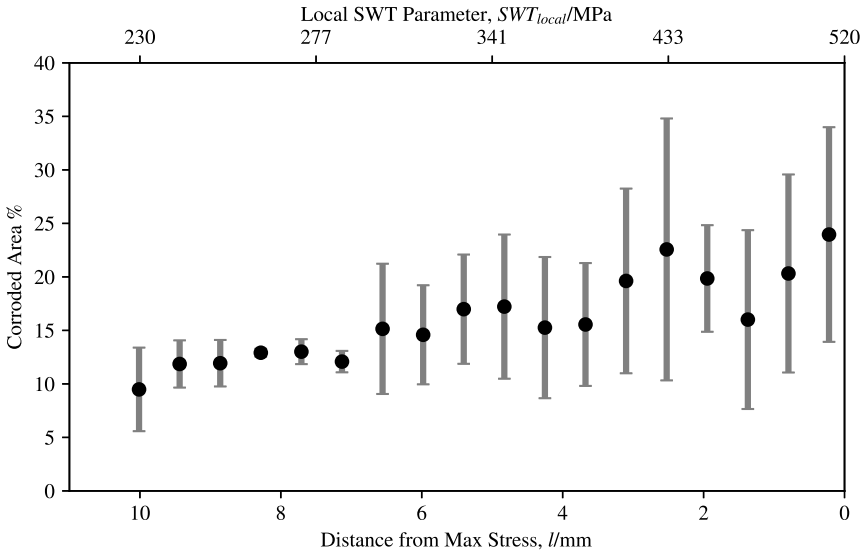

Figure 4.9: Fraction of corroded area as a function of stress levels for trunk conical specimens under $SWT_{nom} = 500$ MPa and f=0.1 Hz (20 h of immersion).

4.2 Corrosion morphology analysis

After the rupture, the cylindrical specimens were submitted to a Scanning Electron Microscope (SEM) analysis in order to evaluate the fractured surface morphology. This analysis was performed on the specimens under $R = 0.1$ load ratio. The absence of the compression phase in the load cycle for this condition preserves valuable information on the propagation surface.

The lateral surface of the specimens were checked for secondary cracks and corrosion defects (Fig.4.10). The level of surface degradation varied significantly depending on the applied stress, and consequentially on the immersion time. For the highest tested amplitude, $SWT = 650MPa$, a few large cracks (more than $300\,\mu m$) and a few corrosion pits were observed. However, for the lower tested amplitude, a great density of microcracks (less than $200\,\mu m$) and corrosion pits were identified. For this condition, the microcracks do not seem to be related with the stress concentrators generated by the corrosion defects.

The microcracks observed for the lower stress condition have random orientations and are not perpendicular to the applied stress which suggests that the crack nucleation occurs at the grain boundaries of the material. These regions are known to be prone to anodic dissolution [28]. Since this behavior was identified for the specimens under low stress amplitude and a higher immersion period, it is reasonable to assume that the failure under this conditions is dominated by the electrochemical processes.

For the higher stress amplitudes, completely perpendicular cracks, with length greater than 300 μm, were identified. The immersion period for corrosion fatigue experiments under high stress amplitudes are shorter when compared to the lower stress amplitudes (5 h for $SWT = 650$

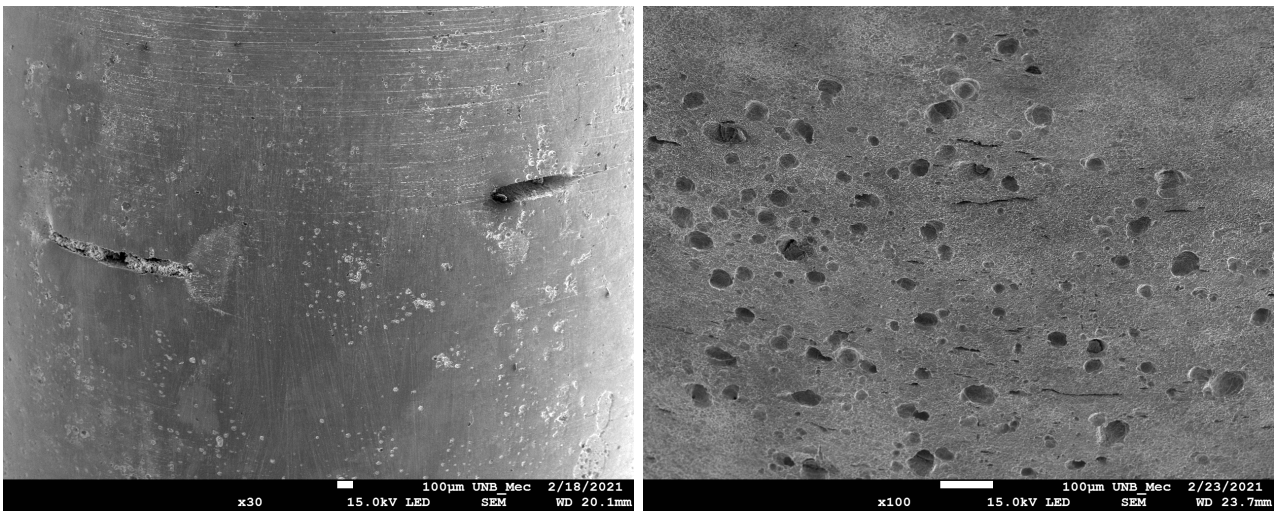

(a) **(b)**

Figure 4.10: Lateral surface of the corrosion fatigue specimens, after the rupture, under (a) $SWT = 650$ MPa and (b) $SWT = 250$ MPa.

MPa versus 137 h for $SWT = 250$ MPa). Since higher stress amplitudes tend to produce a failure morphology similar to the one observed for the in-air condition, the failure for this load level is assumed to be mechanically driven.

The fractured surfaces for the corrosion fatigue condition are shown in Figs. 4.11a, 4.11b, 4.11c and 4.11d, while the fractured surface for in-air condition is shown in Fig. 4.11e. The respective regions are shown in details in Fig. 4.12.

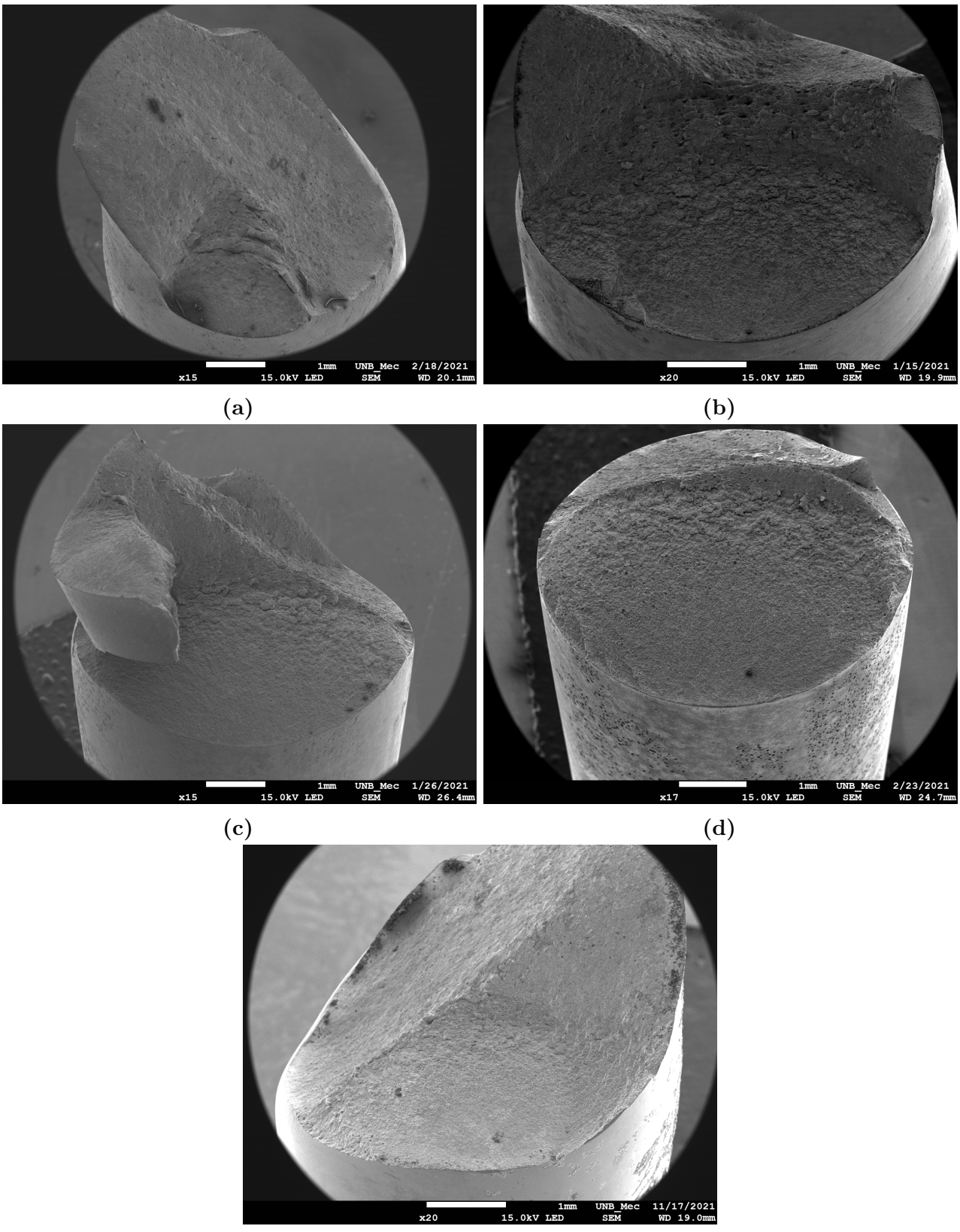

Figure 4.11: corrosion fatigue specimens under load amplitude of: (a) $SWT = 650MPa$, (b) $SWT = 500MPa$, (c) $SWT = 350MPa$, (d) $SWT = 250MPa$ and (e) in-air fatigue specimen under $SWT = 500MPa$

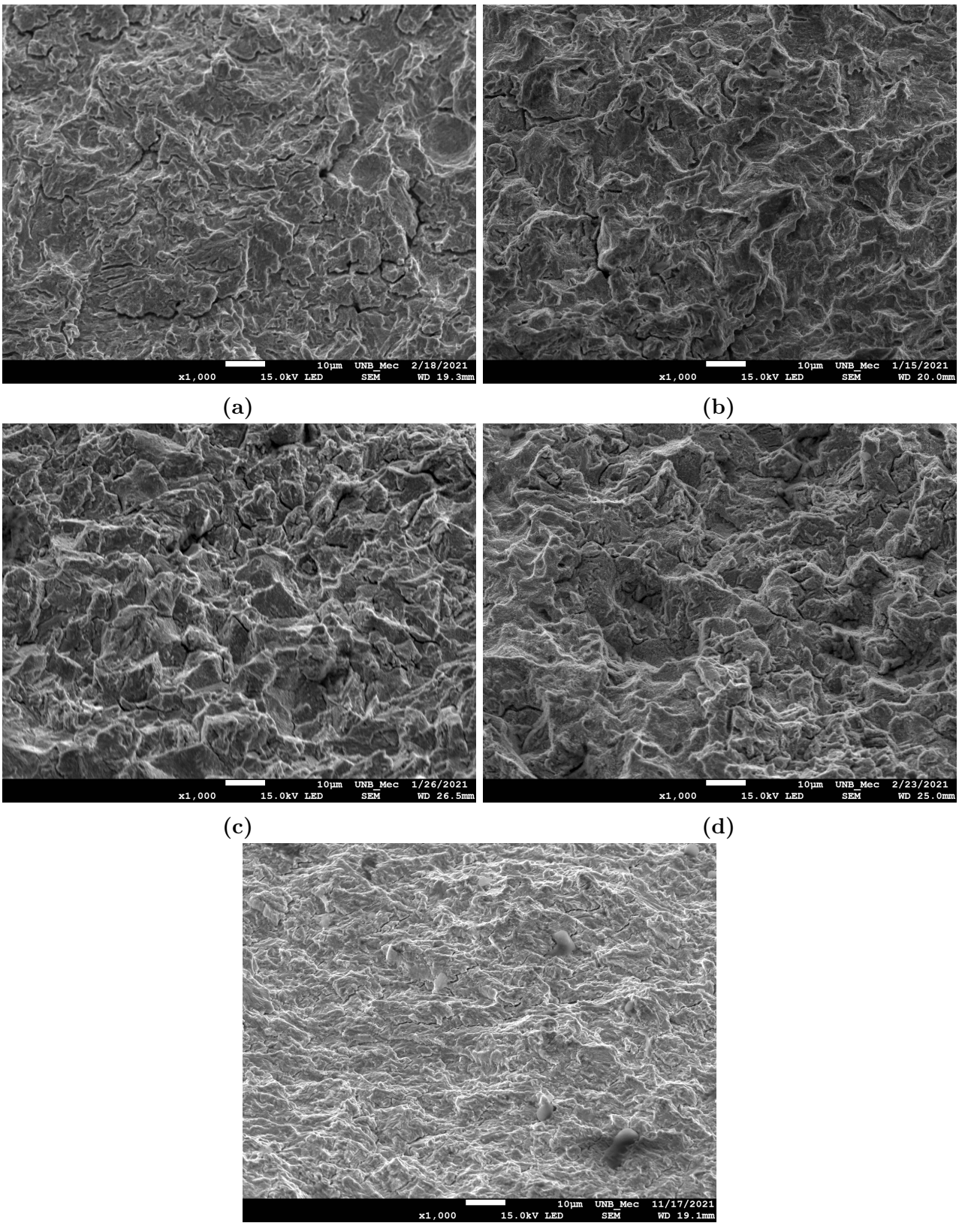

Figure 4.12: Fractured surface morphology for the corrosion fatigue specimens under: (a) $SWT = 650MPa$, (b) $SWT = 500MPa$, (c) $SWT = 350MPa$, (d) $SWT = 250MPa$ and (e) in-air fatigue specimen under $SWT = 500MPa$

From Fig 4.11, it is possible to observe that more severe load amplitudes generate smaller

propagation zones. Perpendicular propagation planes were observed for all the conditions tested. It is also possible to identify a inclined plane after the propagation zone which is caused by the monotonic failure of the material due to shear.

Two distinctive behaviors were identified during the fractured surface analysis of the corrosion fatigue specimens. For higher stress amplitudes, Fig. 4.12a an Fig. 4.12b, transgranular failure was observed. This morphology is similar to the one observed in the in-air condition (Fig. 4.12e). However, for the corrosion fatigue specimens under lower stress amplitudes, Fig. 4.12c and Fig. 4.12d, a portion of intergranular failure was identified. This behaviour was also reported by Zhao *et al.* [53] for a high strength steel under corrosion fatigue in maritime environment.

Images of all conditions tested are presented at Appendix B.

4.3 Electrochemical Measurements

4.3.1 EIS Measurements

The Electrochemical Impedance Spectroscopy (EIS) measurements are presented in this section. The experimental spectra were presented for pure immersion in Fig. 4.13a and corrosion fatigue condition in Fig. 4.13b, and numerically fitted by using the equivalent electric circuit shown in Fig. 3.7. After 1 hour of potential stabilization, and before the load application, the charge transfer resistance was $1950\,\Omega cm^2$. Following this first stage, the effect of time on R_{CT}, which is represented by the diameter of the curves in the Nyquist plot, was different for the non-loaded and loaded specimens. This resistance gradually increased with time in the reference (non-loaded) specimen, while it decreased abruptly in the first 3 hours in the corrosion fatigue specimen (under cyclic load). At the last EIS measurement, the loaded specimen had been subjected nearly to 50000 cycles (N_f=50570) and approximately 15 hours of exposure in the corrosive media. The resistance behaviour difference for equal exposure time was quite significant, as seen from the parameters obtained from the fitting shown in Table 4.1.

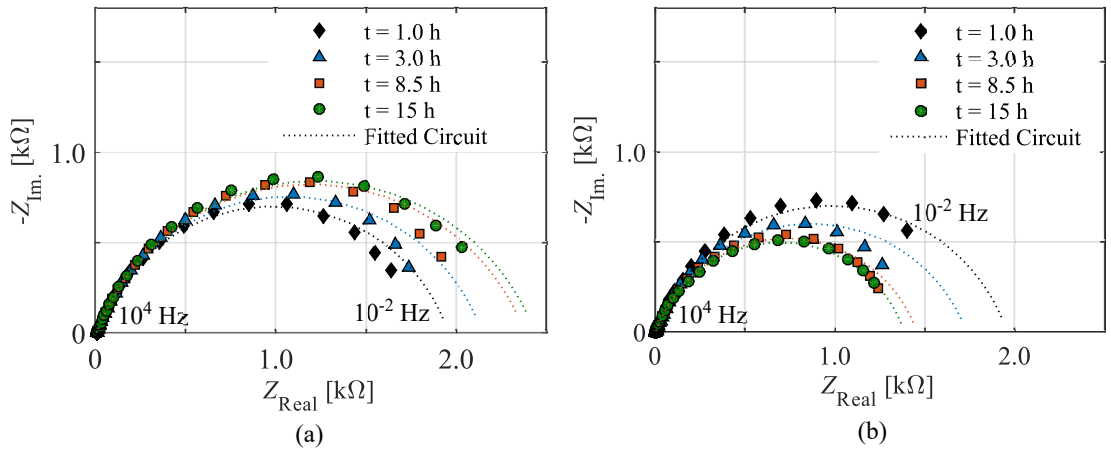

Figure 4.13: Nyquist plots for (a) non-loaded and (b) corrosion fatigue (S_a=500 MPa,N_f=55750 cycles) conditions. Time corresponds to immersion duration; for the corrosion fatigue condition, t=1.0 h was prior to load application and the load was started immediately after the first EIS measurement [70].

Table 4.1: Parameters fitted from the equivalent electrical circuit.

	$R_E/\Omega cm^2$	$R_{CT}/\Omega cm^2$	$Q/\mu F s^{\alpha-1} cm^{-2}$	α
Reference (No Load), t = 1.0 h	8.6	1950	913	0.79
Reference (No Load), t = 15 h	8.5	2430	792	0.77
S_a = 500 MPa, t = 15 h	5.5	1382	1045	0.79

The drop in R_{CT} during the cyclic load application indicates that the material was more active. This kind of evolution, in the absence of any passive film on the surface, can be explained by the appearance of persistent slip bands (PSB). After the appearance of PSBs, a permanent separation of the anodic and cathodic sites is expected. The localized anodic regions have lower impedance compared to the rest of the surface, therefore, it corrodes faster. The crack nucleation will probably occur in these sites, where corrosion takes more severely. At the crack propagation stage, it has been observed [74] that the region between the crack faces is lower in oxygen content compared to the surrounding solution, which makes the crack surfaces more anodic than the rest of the specimen. This localized anodic site can also cause an overall decrease of R_{CT}.

During the test, the intrusion-extrusion events of the PSBs and crack nucleations increase the surface area of the electrode. Thus, an increase in the interfacial capacitance Q can be expected. The parameter α evaluates how the time constant is distributed on the surface and the data reveals that there is no modification of this distribution even with the nucleation of cracks. At the beginning of the corrosion fatigue test, the value of α was already not high (almost 0.8), representing a relatively high dispersion of time constants. This fact can explain the absence of variation in α for more degraded conditions when new events occur (as cracking) that could

eventually have new time constants.

Although EIS is a powerful technique and can provide important information about the electrochemical system, consistency issues were detected on the tests carried out at load amplitudes of 400 MPa and 550 MPa. In general, the EIS measurements relays on a more complex apparatus, with 3 electrode system and applying current fluctuations to the system. A simpler, yet powerful, way to obtain information about the specimen under corrosion fatigue condition is the monitoring of the corrosion potential fluctuation during the experiment. This approach is presented below.

4.3.2 Corrosion Potential Monitoring

A detailed examination of the open circuit potential reveals that small cyclic fluctuations overlap the mean value, with the same frequency of the mechanical loading. The measurements carried out for the specimen under the stress amplitude of $S_a = 500$ MPa ($R = -1$) are shown in Fig. 4.14 to illustrate the potential evolution under cyclic load. The following stages of corrosion potential response were observed: (i) Damage-free response at the beginning of the test – Fig. 4.14a followed by attenuation of the signal, but without significant distortion – Fig. 4.14b (ii) Distorted signals at the middle portion of the test – Fig. 4.14c and 4.14d – and (iii) increase of the distorted signal amplitude at the end – Figs. 4.14e and 4.14f.

One can speculate that the a significant portion of the periodic fluctuations acquired by the potentiostat were introduced by the control of the fatigue testing machine. If this was true, the parasite fluctuations would be constant during the experiment. However, from Figs. 4.14c and 4.14d, it is possible to observe that the signal presents a great level of distortion, with a very low amplitude (less than 0.1 mV). Therefore, even if the fatigue machine introduces some sort of signal into the measurements, this contribution must be negligible compared to the signal of interest.

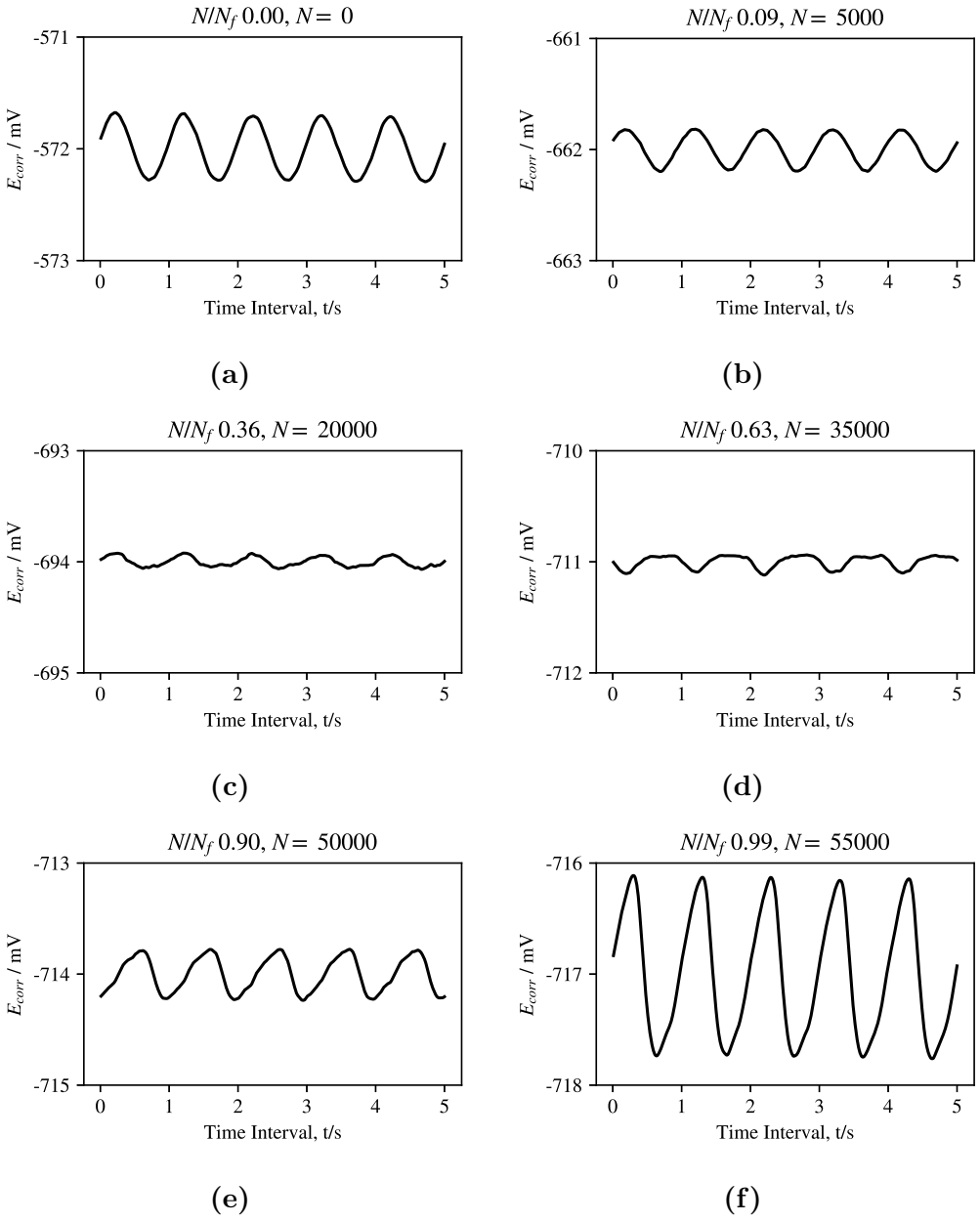

Figure 4.14: Typical corrosion potential evolution obtained at different stages of the corrosion fatigue test (S_a = 500 MPa,N_f = 55750 cycles): (a) $N/N_f \approx 0.00$; (b) $N/N_f \approx 0.18$; (c) $N/N_f \approx 0.36$; (d) $N/N_f \approx 0.63$; (e) $N/N_f \approx 0.90$; (f) $N/N_f \approx 0.99$.

The overall aspect of the specimen during the corrosion fatigue test performed under 500 MPa of stress amplitude is depicted in Fig. 4.15, in which the Fig. 4.15a represents the initial condition of the test. The first signs of the formation of he corrosion products on the specimen were observed for lives as low as 5000 cycles, which corresponds to approximately 2.5 h of immersion (Fig. 4.15a). At 30000 cycles, 9.3 h of immersion, the most part of the working section was covered with corrosion products. Close to the rupture, at 50000 cycles, almost all the surface of the specimen were covered with corrosion products.

(a) **(b)** **(c)** **(d)**

Figure 4.15: Typical corrosion products growth during the corrosion fatigue test (a) at the first cycles, after (b) 5000 cycles, (c) 30000 cycles and (d) 50000 cycles.

In order to be able to correlate the different responses of the corrosion potential with the degradation state of the specimen, a new set of corrosion fatigue tests were carried out. Each test was stopped at a different life and an inspection of the corroded surface was performed, as shown in Fig. 4.16. The tests were performed with the same loading conditions ($S_a = 500$ MPa, $f = 1.0$ Hz) of the test that generated the curves shown in Fig. 4.14. The test used to obtain the characteristics of the corroded surface after the rupture presented a fatigue life of 64440 cycles, while the test performed to capture the E_{corr} signals presented a life of 55750 cycles. The fatigue life difference between these tests was under 16%. Thus, it is assumed that the test carried out during the corrosion potential readings and the test performed to evaluate the surface morphology at the final cycle (Fig. 4.16e) would exhibit a similar corrosion fatigue degradation evolution.

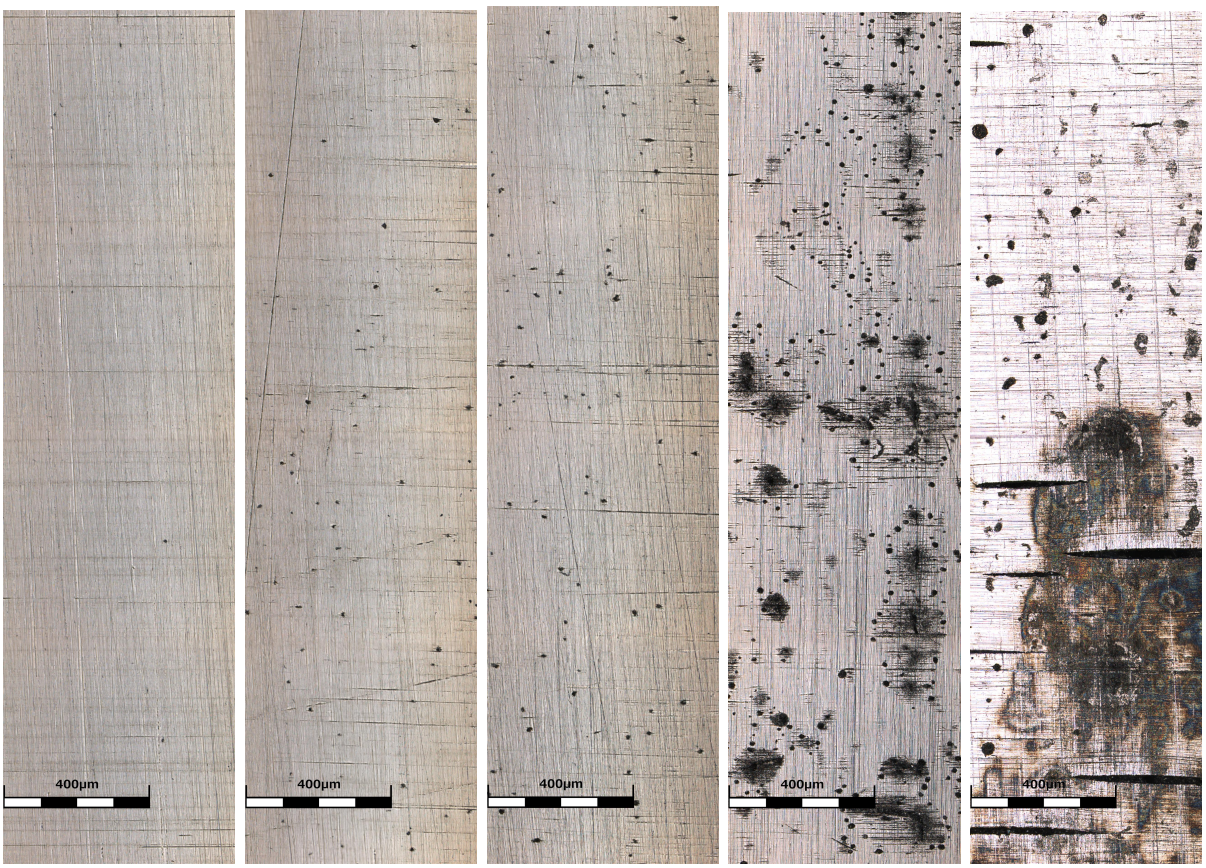

(a) 5000 Cycles **(b)** 20000 Cycles **(c)** 35000 Cycles **(d)** 45000 Cycles **(e)** 64440 Cycles

Figure 4.16: Typical corrosion morphology evolution obtained at different stages of the corrosion fatigue test

Stage I - Attenuation of the signal

In the first stage, the E_{corr} showed a pure sinusoidal waveform with the same frequency as the cyclic load and mean potential of -572 mV vs. Ag/AgCl while the signal range (2 x amplitude) was 0.66 mV. At the first cycles, the potential fluctuation is assigned to purely elastic deformation, therefore this response can be considered the behavior of a damage-free material.

For the first 10000 cycles, a reduction of the sinusoidal signal was observed. The spectral decomposition of the corrosion potential signal (Fig. 4.17) shows no significant signs of distortion, *i.e.* the amplitude of the harmonics were very low when compared to the amplitude of the fundamental frequency (1.0 Hz).

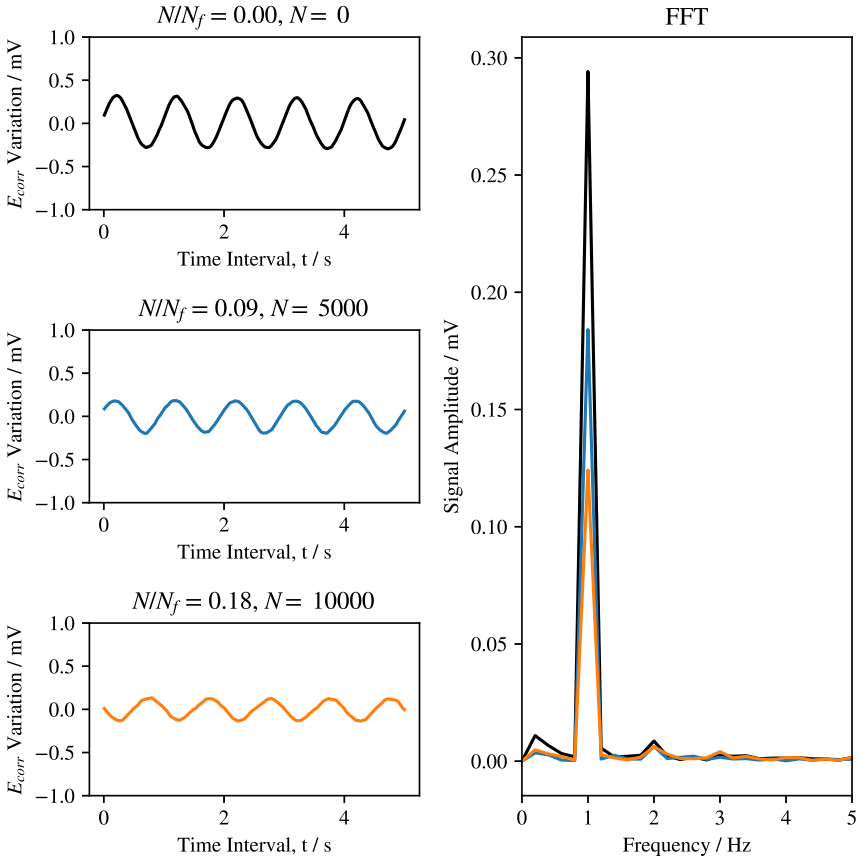

Figure 4.17: Spectral decomposition of the corrosion potential signal for the first 10000 cycles.

At a initial stage, around 5000 cycles, almost no corrosion degradation was on the specimen's surface after the cleaning (Fig. 4.16). Since almost no geometric defects were identified, the stress distribution on the specimen is similar to the initial condition. Meanwhile, the formation of corrosion products on the surface of the specimen was observed, as shown in Fig. 4.15b. At this stage, the corrosion potential response hasn't showed signs of distortion. Therefore, it can be assumed that the decreasing amplitude observed at this stage is due to the growth of corrosion products on the surface of the specimen, which can act as an additional resistance to the electrochemical reactions.

Stage II - Distorted signal with low amplitude

For the intermediate portion of the corrosion fatigue test, for lives between 20000 and 35000 cycles, the corrosion potential response describes a signal with amplitude lower than 0.08 mV and highly distorted, as shown by the spectral decomposition in Fig 4.18.

At this point, it is possible to observe the formation of pits at this fatigue life region as shown in Figs. 4.16b and 4.16c. Thus, the distortion of the E_{corr} signal observed in Figs. 4.14c and 4.14d is probably caused by heterogeneities on the metallic surface, such as the formation of pits, which would produce a non-linear electrochemical response in relation to mechanical

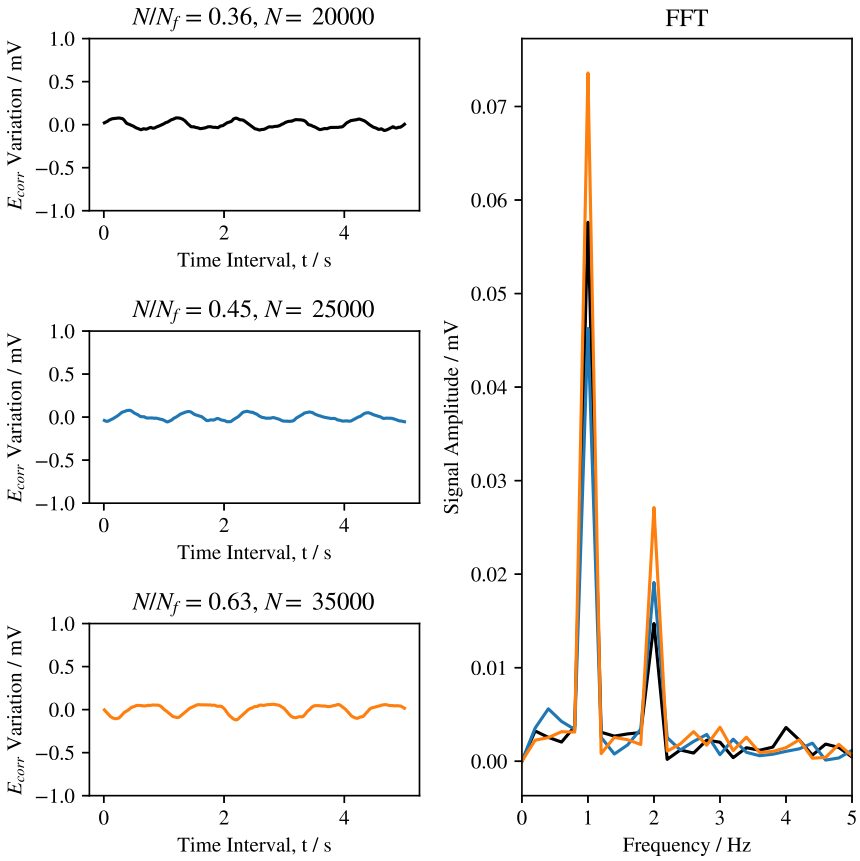

Figure 4.18: Spectral decomposition of the corrosion potential signal for the cycles between 20000 and 35000.

load input.

The same phenomenon, i.e. distortion of the electrochemical response, was observed [19] on iron bars after the appearance of heterogeneities on the inspection area.

Stage III - Sawtooth signal with increasing amplitude

At a higher number of cycles, a continuous increase in the amplitude of the distorted electrochemical response was observed, as shown in Fig. 4.19. The morphology of the corroded surface presented a rapid evolution at this stage. Form Figs. 4.16d to 4.16e it is observed that the number of cracks and their size increased abruptly on the last part of the corrosion fatigue test. This rapid change is also verified by the electrochemical measurements, with a rapid increase of the corrosion potential amplitude from 50000 to 55000 cycles.

This is likely related to the corrosion fatigue long crack propagation regime. In this regime, each cycle reveals an increasing portion of bare material towards the final rupture of the specimen, which would be an interpretation for the rapid E_{corr} amplitude growth observed in the last cycles.

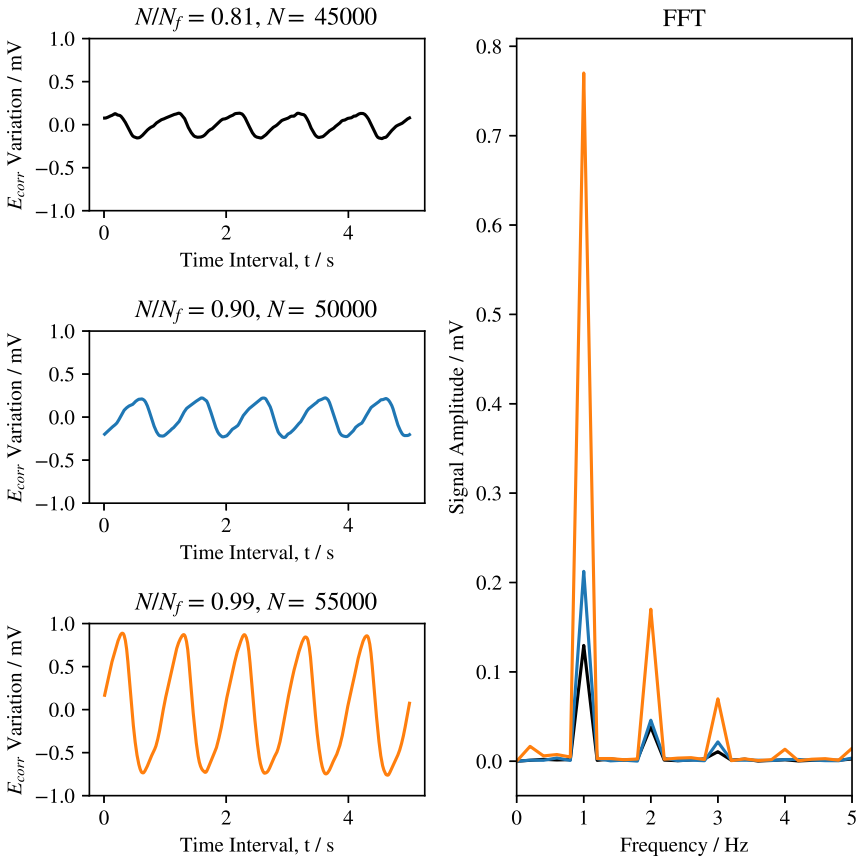

Figure 4.19: Spectral decomposition of the corrosion potential signal for the last 10000 cycles.

When the damage of the specimen is intense, the electrochemical processes become more complex. At the last 10 cycles (Fig. 4.20) it is possible to identify that the saw-tooth shape response observed in Figs. 4.14e and 4.14f is composed by at least two phenomena, causing two peaks overlapping the lowering mean potential value. The first peak grows relatively to the second as the material tends to the failure. This behavior is likely associated with the exposure of fresh material due to the propagation of the main crack responsible for the specimen failure.

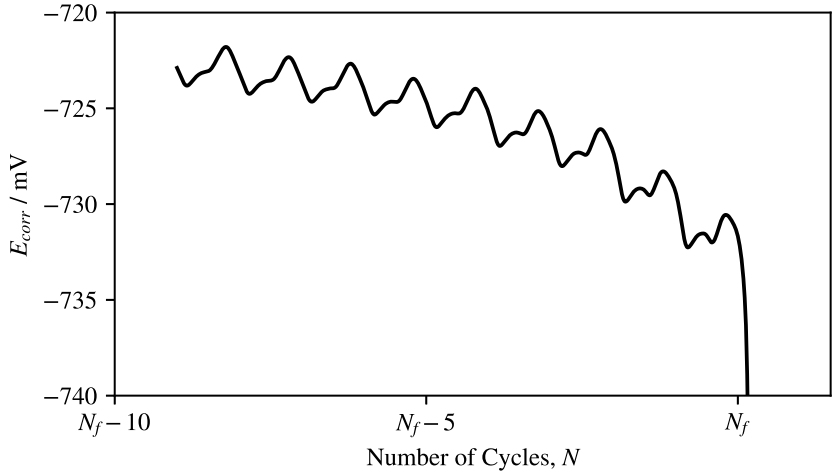

Figure 4.20: Corrosion potential at the last 12 cycles ($S_a = 500$ MPa,$N_f = 55750$ cycles).

To evaluate the consistency of the corrosion potential response behavior throughout a range of stress amplitudes, the same measurements depicted in Fig. 4.14 was carried out for amplitudes of $S_a = 400$ MPa, $S_a = 450$ MPa and $S_a = 550$ MPa.

Figure 4.21 illustrates the variation of potential amplitude with the normalized number of loading cycles for all the corrosion fatigue tests and Fig. 4.22 shows the variation of the mean potential with normalized time for the specimens under cyclic load and without load for different stress amplitudes. It was noticed that the E_{corr} amplitude described a similar evolution for different stress amplitudes tested: a decrease to a minimum value, which usually was observed around the half of the corrosion fatigue life, followed by an increase up to the rupture of the specimens.

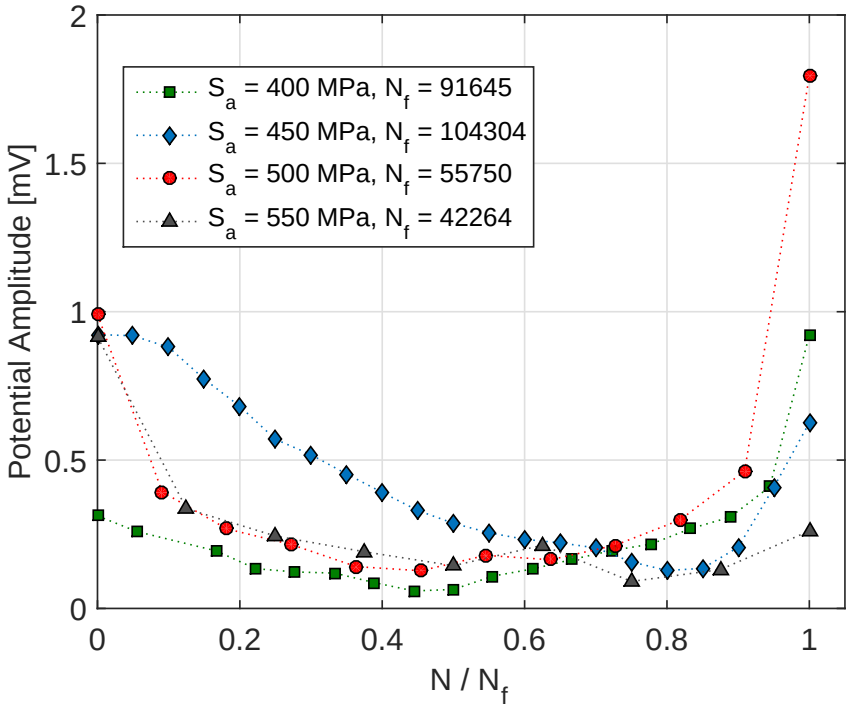

Figure 4.21: Electrochemical potential amplitude of the corrosion potential fluctuations measured during the corrosion fatigue experiments [70].

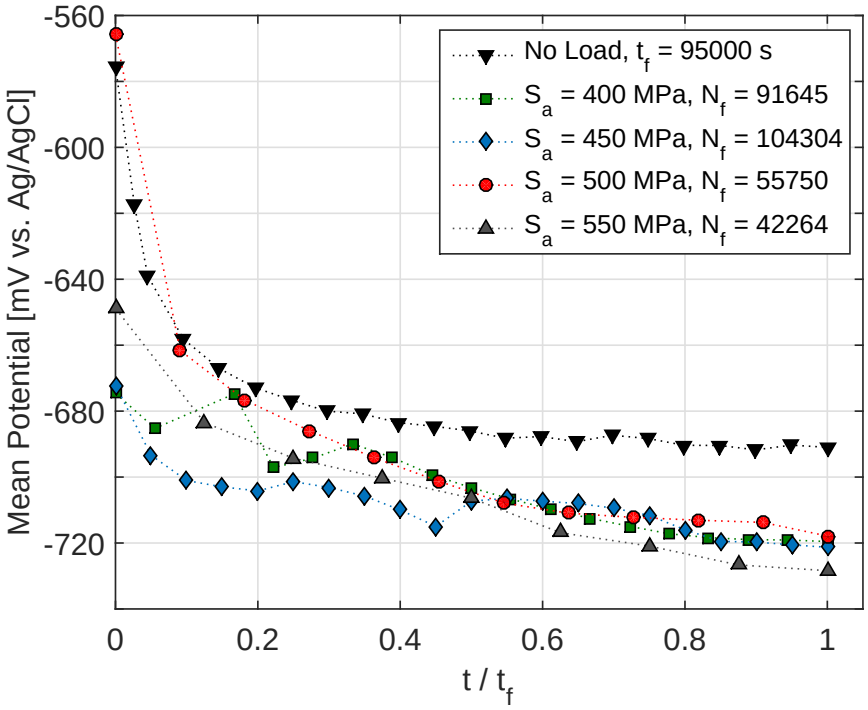

Figure 4.22: Electrochemical mean potential measured during the corrosion fatigue experiment and exposure without load test [70].

The mean corrosion potential presents an initial drop due to the depletion of oxygen on the metallic surface (Fig. 4.22), followed by a less pronounced decrease for the rest of the

exposure period. The specimen under cyclic load had a consistent lower potential compared to the non-loaded one. After 50000 s, the free potential of the non-loaded specimen had stabilized at -690 mV (Ag/AgCl) and almost no change in the mean potential was observed from this point up to the end of the test (95000 s). The free potential values for the specimens under cyclic load converged to -720 mV (Ag/AgCl) at the end of the corrosion fatigue tests. The difference between the two conditions increases with time, which can be attributed to the evolution of accumulated plastic strain in the vicinity of the corrosion defects and the growth of non-perturbed rust of non-loaded specimens.

Another important aspect of the E_{corr} monitoring is the amount of the distortion of the electrochemical response. For this analysis, the signal is transformed from the time domain into the frequency domain using the Fast Fourier Transform (FFT). The amount of distortion of a harmonic function can be defined, for example, as the contribution of the natural frequency with respect to its harmonics, as follows:

$$THD = \frac{1}{A_0}\sqrt{\sum_{n=1}^{\infty} A_i^2}, \tag{4.2}$$

where THD is the total harmonic distortion, A_0 is the amplitude of the natural frequency and $A_n, n \geq 1$ are the amplitude of the harmonics. Typically, calculations are performed up to the 10^{th} order ($n = 10$). Figure 4.23 shows the evolution of the THD during the corrosion fatigue for the different stress amplitudes tested and considering $n = 10$.

According to the study performed by Tada [19], the increase of the distortion is related to crack initiation. However, for the material and conditions tested in this study, the distortion of the signal was caused by the presence of corrosion defects. Before these surface heterogeneities, it was possible to assume a linear correlation between the load level and the electrochemical response. After a certain level of surface degradation, a number of non-linear phenomena contribute to the increase of the distortion of the signal. For more advanced lives, the presence of macrocracks contributes to increase the amplitude of the response signal which reduces the value of the total harmonic distortion.

The corrosion potential stages for all load conditions tested are summarized in Fig. 4.24. A detailed report of all the electrochemical measurements performed is presented at Appendix 1.

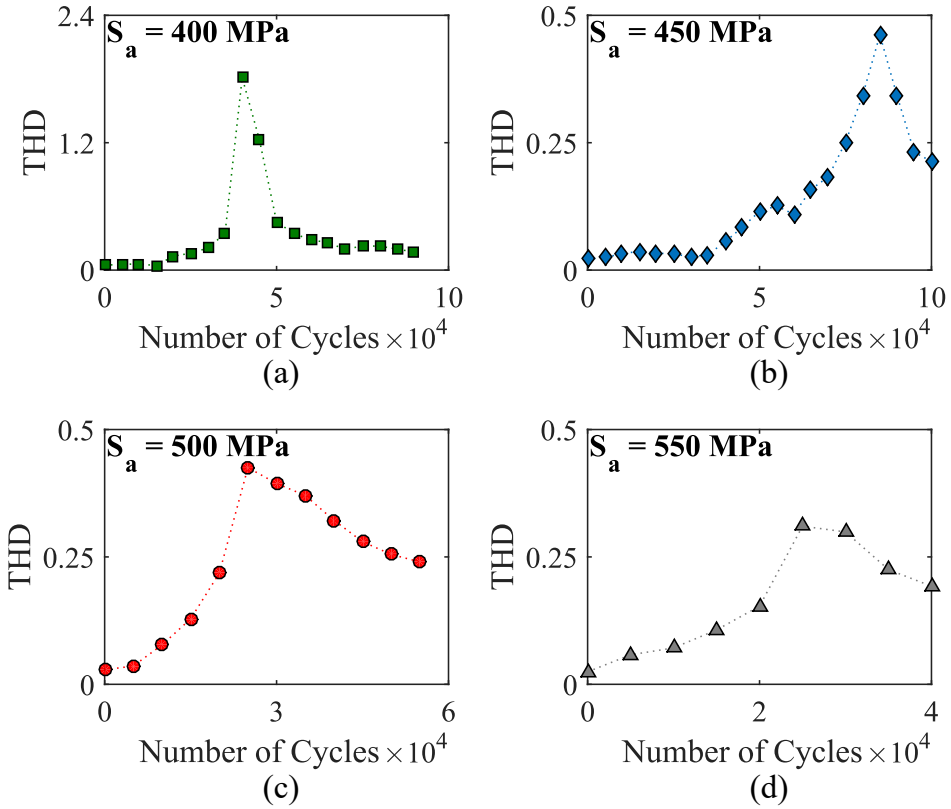

Figure 4.23: Total Harmonic Distortion (THD) during corrosion fatigue tests with stress amplitudes: (a) 400 MPa, (b) 450 MPa, (c) 500 MPa and (d) 550 MPa.

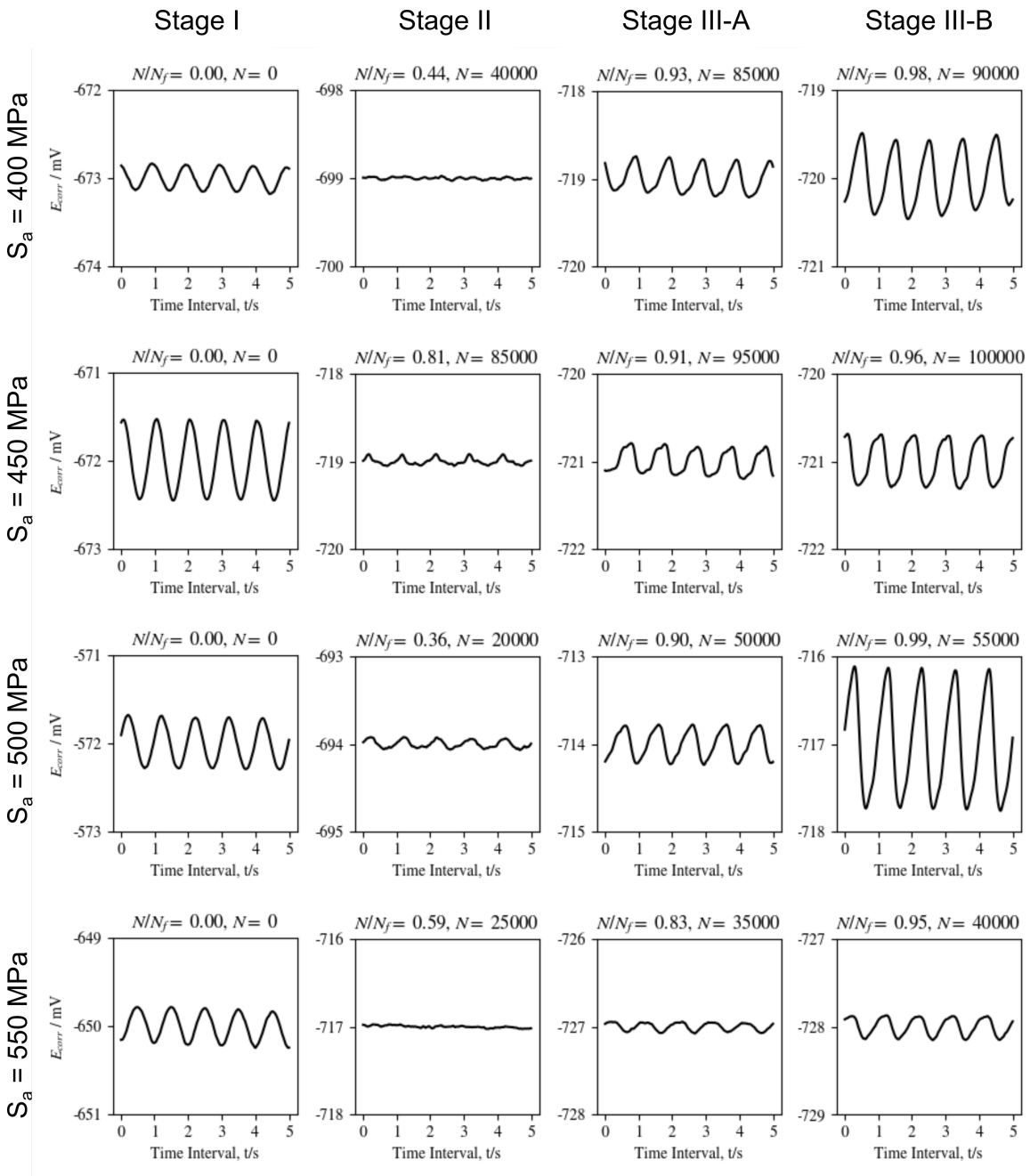

Figure 4.24: Summary the corrosion potential measurements for all load conditions tested.

Chapter 5 – Discussion

Corrosion fatigue is a complex form of failure, that can be described as the overlapping of distinct process such as pitting corrosion, stress corrosion cracking and mechanical fatigue [75]. The electrochemical phenomena consist of pitting formation, or anodic dissolution at crack tip, while the mechanical effects consist of slip bands formation and crack initiation and propagation, and all these effects tend to occur quasi-simultaneously.

During crack initiation, small fractions of atomically clean material become exposed to the environment, at slip bands [45, 76]. These slip bands can be reversed, depending on their size and geometry and on the environment (vacuum, air or solution); in immersion, larger slip bands have generally low reversibility because of the oxide films produced on the surface, generating persistent slip bands (PSB), which, under cyclic stress, increase in number and in their offset height [36]. These PSB are favourable sites for anodic dissolution, as they are fresh material and anodically active sites. Most of the studies on corrosion fatigue do not deal with low alloy steels, but with passive alloys, namely Cr-rich steels, and they describe the progress of corrosion fatigue cracks based upon a metal surface that is passive in all the outer surface and becomes exposed only at the crack tip or at the PSB. However, the same principle can be applied to active materials, with the difference that the outer surface is not truly passive, but instead it has easier access to dissolved oxygen, while the fresh material at the tip is in an oxygen-depleted region. This can lead to a differential aeration effect in which the crack tip is anodic while the cathode is at the mouth of the crack. The oxygen concentration along the crack has been modelled by Turnbull et al [77], who concluded that oxygen access to the crack is mostly controlled by forced convection near the crack mouth, while this pumping does not effectively reach the crack tip, i.e., the oxygen at the crack tip is due to diffusion only. This generates conditions for a differential aeration cell, with the outer surface and the crack walls near the mouth, being cathodic (aerated), while the crack tip becomes anodic, due to oxygen depletion.

The stress amplitude affected the morphology of the fatal crack surface 4.12. While transgranular cracking was observed under high loads, intergranular failure was observed for lower stress amplitude. This is likely due to PSB formation at a lower rate for lower stress amplitudes, while dissolution at grain boundaries becomes the controlling process. Although both processes contribute to a decrease in the crack nucleation time, the effects of the dissolution at grain boundaries seems to be more pronounced on the reduction of the fatigue life. The same

effect has been reported by other authors, namely by Magnin [45], who drew a similar conclusion by varying the strain rate. For a higher rate, PSB formation occurred faster and transgranular failure was observed, while lower strain rates favored the dissolution at grain boundaries, leading to intergranular failure. For stable crack propagation, competitive models are usually accepted [28]. In these models, the crack growth rate can be controlled either by the anodic dissolution at the crack tip or by the tensile effect on the crack. The stable propagation rate of a fatal crack is often greater than the material loss due to anodic dissolution, meaning that the propagation rate of the fatal crack can be driven mostly by the mechanical effect [76].

Regarding the load ratios tested, the Smith-Watson-Topper parameter can capture the mean stress effect especially well for corrosion fatigue environmental condition, with the results laying within a factor-of-two boundary (Fig. 4.4). All the in-air results stayed within a factor-of-four. A rough fatigue life reduction estimation, comparing the fatigue lives under corrosive environment and in air condition can be performed in terms of the SWT parameter. Considering a Basquin [78] life estimation $SWT = AN_f^b$, the ratio $N_{f(CF)}/N_{f(IA)}$ leads to a life reduction relationship irrespective of the applied load ratio as follows:

$$\frac{N_{f(CF)}}{N_{f(IA)}} = \frac{\left(\frac{SWT}{A_{CF}}\right)^{(1/b_{CF})}}{\left(\frac{SWT}{A_{IA}}\right)^{(1/b_{IA})}} = \frac{{A_{IA}}^{1/b_{CF}}}{{A_{CF}}^{1/b_{IA}}} SWT^{\left(\frac{1}{b_{CF}} - \frac{1}{b_{IA}}\right)}, \tag{5.1}$$

where $A_{IA} = 19800$ MPa, $A_{CF} = 1200$ MPa, $b_{IA} = -0.335$ and b_{CF} are the coefficients obtained from curves is Fig. 4.4. For fully alternated load ratios ($R = -1$), the SWT amplitude is equal to the stress amplitude, Sa. Thus, the ratio $N_{f(CF)}/N_{f(IA)}$ in terms of SWT amplitudes describes an identical curve as the one presented in Fig. 4.2a. The exponential behavior of both curves causes the life ratio to reduce very fast for lower SWT amplitudes – almost seven orders of magnitude for $SWT = 250$ MPa. This ratio is based on extrapolations of the fatigue curves and its domain of application is very restricted. The values given by this correlation could not be verified for most of the applied amplitudes (almost all of the stress amplitudes applied to the corrosion fatigue condition resulted in runouts when applied to the in-air condition). Nevertheless, this mathematical relationship highlights how detrimental the corrosive environment can be, especially in the lower stress amplitude range.

5.1 Electrochemical Reactions

Figure 5.1 presents the Pourbaix diagram for iron at iron at 25°C in the presence of water. The area delimited by lines (a) and (b) is that of thermodynamic equilibrium of water with its oxygen, H_2O/O_2 and with its hydrogen H_2O/H_2, respectively. Above line (a), water is unstable

with respect to oxygen evolution, and therefore it becomes oxidized and releases oxygen (OER, oxygen evolution reaction). Below line (b), water is unstable with respect to hydrogen evolution, and therefore it undergoes reduction and hence releases hydrogen (Hydrogen Evolution Reaction, HER). Corrosion of iron in under neutral pH involves the reduction of dissolved oxygen as the cathodic reaction. As seen in the Pourbaix diagram, for water at pH of 6.0 and potentials around -0.4 V vs SHE (-0.69 V vs Ag/AgCl), the HER has a negligible overpotential, and the most important cathodic reaction is the reduction of water, with an overpotential of over 1.0 V. Naturally this means that hydrogen embrittlement is ruled out as in this study.

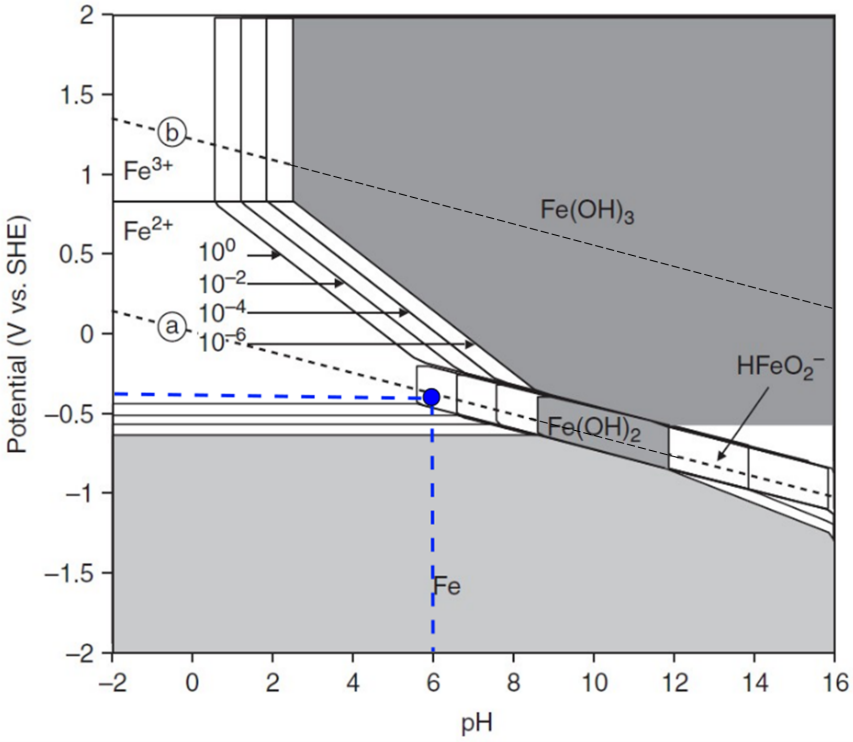

Figure 5.1: Pourbaix diagram for iron in water at 25°C.

For iron in contact with water (neutral pH), the oxidation reaction is:

$$\mathrm{Fe} \longrightarrow \mathrm{Fe}^{2+} + 2\,\mathrm{e}^{-}, \tag{5.2}$$

while the electrons liberated by the oxidation flow through the metal and feed the reduction process, which, in the presence of dissolved oxygen, is:

$$\frac{1}{2}\,\mathrm{O}_2 + \mathrm{H}_2\mathrm{O} + 2\,\mathrm{e}^{-} \longrightarrow 2\,\mathrm{OH}^{-}. \tag{5.3}$$

The cathodic reaction causes local pH rise, even though the pH of the bulk solution may remain unaltered. The $Fe(2+)$ ions migrate towards the cathode, but they are not stable at alkaline pH and therefore they tend to precipitate in the vicinity of the cathode. This results in

accumulation of corrosion products at the cathodic sites, rather than at the anode.

$$Fe^{2+} + 2\,OH^{-} \longrightarrow Fe(OH)_2. \tag{5.4}$$

Which in the presence of dissolved oxygen, may be further converted to Fe(III) species, like $Fe(OH)_3$ or Fe_2O_3.

The tests were carried out with stagnant solution and a rapid shift of the mean corrosion potential to more negative values was observed in the first minutes of the test. The OER typically occurs under diffusion rate control, under conditions of limiting current. This means that all the oxygen that reaches the surface is immediately converted at the electrode, and therefore the cathodic current is described by a current plateau. Variations in the oxygen concentration thus lead to differences in the resulting corrosion rate, and the initial potential drift is likely due to both iron activation (due to dissolution of oxides formed in the atmosphere despite the short time between the surface preparation and the start of the experiments) and oxygen depletion, which causes a reduction of the cathodic reaction rate, as shown in Fig 5.2.

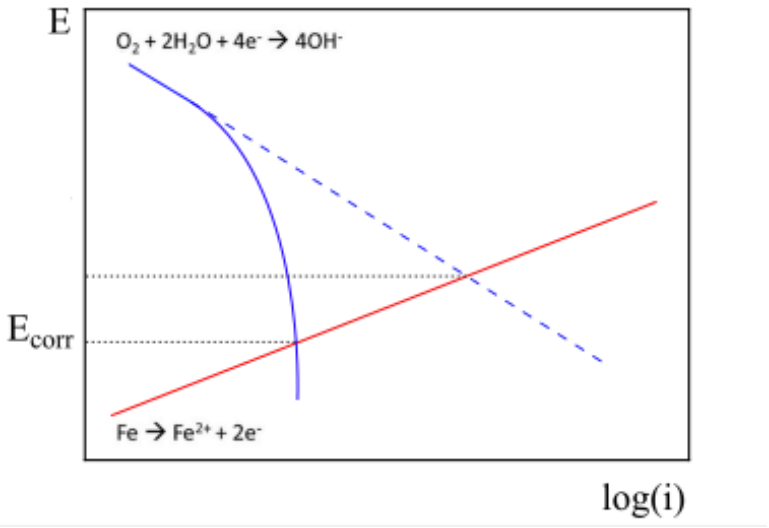

Figure 5.2: Electrochemical reactions for oxygen reduction under diffusion rate control.

5.2 Corrosion Potential Fluctuations

The tests carried out in this thesis were made under spontaneous corrosion, *i.e.*, under null current cell current, with the cyclic stress being the only stimulus applied. Naturally, the anode and the cathode are in different regions of the specimen, and the corrosion rate current will vary, but the process is totally spontaneous from an electrochemical perspective. This approach is distinct from that used by most of the authors, who were concerned with corrosion of stainless steel or other alloys with passive behavior, and who carried out their studies under

potentiostatic control, while the current flowing out of the specimen across the electrochemical cell was monitored [18, 19, 46]. In those studies the outer surface is passive, while at each opening of the crack some fresh metal is exposed and becomes active. The resulting current is not really the corrosion rate, but rather the excess of anodic current (beyond the rate of the cathodic reaction rate) and its real meaning is somehow hard to interpret. In the present work, of course, there the limitation of not being able to determine the corrosion rate or any other current. However, it is surprising how the fluctuations of the potential and their evolution are quite similar. The evolution of both the E_{corr} and E_{corr} fluctuations suggest the existence of three stages in the corrosion fatigue process described below.

Stage I – Induction

Along the lifetime of the specimens under cyclic load, the E_{corr} fluctuation pattern changed steadily and reproducibly in terms of the amplitude variations and the distortion of the signal. In the first stage, the potential has a sinusoidal pattern, with the same frequency as the applied stress. During this initial stage, a test was made applying only a few cycles of loading at a reduced frequency of 0.1 Hz, which allowed the identification of the traction phase corresponding to the potential shift in the positive direction i.e., the potential becomes less negative, while the more negative part of the curve corresponded to the compression half-cycle. The same behavior is assumed to be valid in all the stages of degradation (although not checked in other conditions). Naturally, there may be a phase shift between the potential and the strain, as reported by other authors [20] but that could not be measured.

In the first cycles, the E_{corr} fluctuation is a clean sine wave and reveals purely elastic deformation; the applied stresses amplitude is around 50% of the yield stress, and the response is thus that of a damage-free material. Still, the amplitude of the E_{corr} fluctuations tends to decrease. The spectral decomposition of the corrosion potential signal (Fig. 4.17) shows no significant signs of distortion, i.e. the amplitude of the first harmonics were very low when compared to the amplitude of the fundamental frequency. This response has been interpreted in the literature with different causes: either the charging of the electrical double layer related to area changes due to stress application or the change in the surface energy due to the applied stress [46]. The electrochemical double layer behaves like a capacitor where opposite charges are stored along the metal-electrolyte interface. Elastic strains produce changes in this interfacial area and, hence, the total charge stored within the double layer also changes accordingly [46]. This phenomenon produces a transient response with the same frequency as the cyclic loading. In terms of electrochemical potentials, an increase of the interfacial area (tension) could cause an increase on the electrochemical potential. Although the study performed by Li *et al.* deals with an electrochemical system under potentiostatic control, different levels of polarization were applied in their study, including potentials near to the corrosion potential of the sample. Thus, it is reasonable to assume that both fluctuations (the potentials registered in this study and the currents identified by Li *et al.*) share similar causes. The possible charge-discharge of the double layer could be better interpreted with data from the phase shift between stress and potential

[19]. An alternative cause for these fluctuations is the variation of the lattice parameter, and thus the surface energy of the specimen, as proposed for single crystals [79] and even for stainless steel [46].

Stage II - Nucleation

During this stage, intense pit nucleation was observed along an otherwise polished surface, while micro-cracks likely also nucleate, under the effect of the cyclic stress. These are non-synchronous stimulus, which results is severe distortion of the potential signal. During this phase, the E_{corr} amplitude becomes much lower and depends less on the load stimulus as it did in Stage I, accompanied by a significant contribution of the first harmonic. At this stage, not only elastic but also plastic strain (pit region) explains the complexity of the response signal, likely because of the exposure of material at slip steps, under both tension and compression loads [60]; the reactivity of the newly exposed area is higher than the original surface, which can be explained by the differences in the composition and atomic arrangements between the newly formed and the original regions. The shape of the potential transients has a surprisingly good coincidence with the current transients reported by other authors and assigned to the rapid dissolution of newly exposed material [60]. One interesting aspect is the asymmetry of the potential fluctuations. Often one of the half-waves, most commonly the anodic one, is more affected than the other. This likely means that the nucleation both of small cracks and of pits control the anodic variation of the potential and thus have a time response that is totally unsynchronised with the load.

Stage III - Propagation

At this stage, the amplitude of the potential transients increased in subsequent cycles. Further, the development of the second harmonic was observed. This is the stage of crack propagation and the growth of the potential amplitude can be justified by the increase of exposed area in subsequent cycles [19, 45, 60]. The reactivity of the newly exposed area is much higher than the pre-existing surface, and hence a transient is expected when the fresh surface is exposed to the solution [60]. It is noteworthy that crack propagation only occurs during a brief period of the tension phase of the loading. In this stage, the potential fluctuations become more complex, *i.e.* with more relevant harmonics, as shown in Fig. 4.19. The exposure of fresh material is appointed as the main reason for electrochemical responses changes after crack nucleation [19, 60]. Opening of the crack increases the anodic area, but it also enhances the cathodic reaction at the walls of the crack, which tend to be more active than the rest of the specimen's surface [74]. Crack opening increases the ratio between the anodic areas (small compared to the rest of the exposed surface) and cathodic areas on the specimen. In practical terms, after crack nucleation, two distinctive behaviors are expected – one during the tension phase of the load, with all the cracks open and the other on the compression, when the cracks will be closed. The response for each load phase (tension and compression) would become further apart from each other as the crack grows, which is likely perceived as an increase of the amplitude and distortion of

the signal. Finally, the forced convection of oxygen due to the motion of the crack faces can also contribute to the potential response. Since the cathodic reaction for this system is under diffusional control, solution convection would facilitate the delivery of oxygen to the cathodic reaction, increasing the limiting current. In terms of potential, this would be perceived as an increase of the potential (Fig. 5.3). The potential fluctuations due to solution stirring comes with a high level of noise, which would explain the increase of relevant harmonics during this phase.

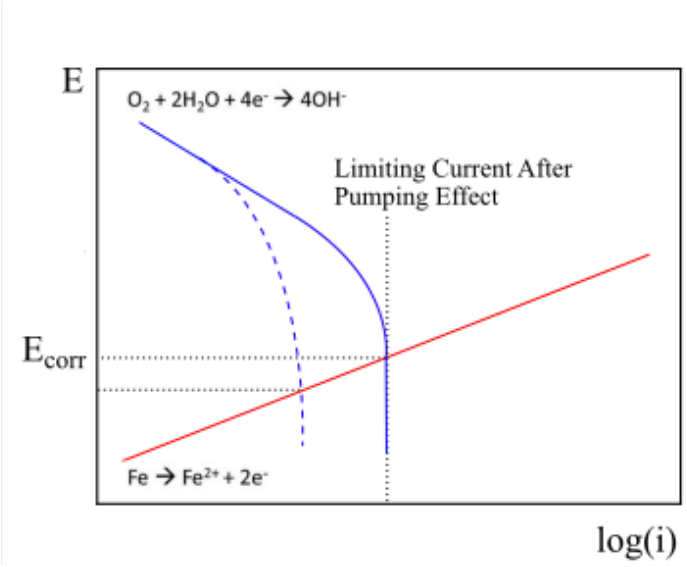

Figure 5.3: Electrochemical reactions for oxygen reduction under forced convection.

From an electrochemical perspective the potential shift to more positive values (in the crack opening) can result either from the cathodic depolarization (increase of oxygen concentration) or from anodic polarization (inhibited oxidation). Comparatively, the cathode is much larger than the anode, as it comprises all the external surface. Therefore changes in the cathodic current should not be expected as a consequence of crack opening. However, it is hard to understand how the anodic reaction could become more polarized (slower kinetics) upon the opening of the crack, *i.e.*, when fresh metal becomes exposed. Further, under oxygen diffusion control, the variation in the anodic kinetics would not affect the current transients. A possible explanation for this apparent contradiction is that the outer surface contributes only moderately to the differential aeration cell (either because of the pitting on the outside or because of some passivation due to the local alkalinization), while the actual cathode is located at the crack walls, especially in outer section of the crack [77]. As the crack opens, forced convection of fresh electrolyte brings dissolved oxygen into the crack, increasing the galvanic current and accelerating the reaction. The larger this cathodic area, the larger the potential transient.

The distinctive potential responses can be identified by comparing the first and second harmonic contributions with the fundamental amplitude of the signal (A_n/A_0), as shown in Fig. 5.4. Stage I is described by a pure sinusoidal variation at the fundamental frequency. At this phase, only elastic deformation occurs. In stage II an increase contribution first harmonic

is interpreted as the nucleation of pits and microcracks on the surface, eventually with the appearance of plastic strain due to the stress concentrations, as observed by other authors [18, 45, 46]. At Stage III, an increase of the second harmonic and decrease of the first harmonic contributions reveals that the area inside the crack increases gradually, while forced convection operates due to the movement of the crack walls. A greater contribution of the higher order harmonics was also observed by Tada *et al.* [18].

The transition from Stage II to Stage III can be hard to distinguish. The newly formed cracks have a very short length, and therefore their effect on the electrochemical response is also small. As their number increases and they grow, their effect on the response becomes more evident, which makes hard to pinpoint a discrete frontier between Stages II and III.

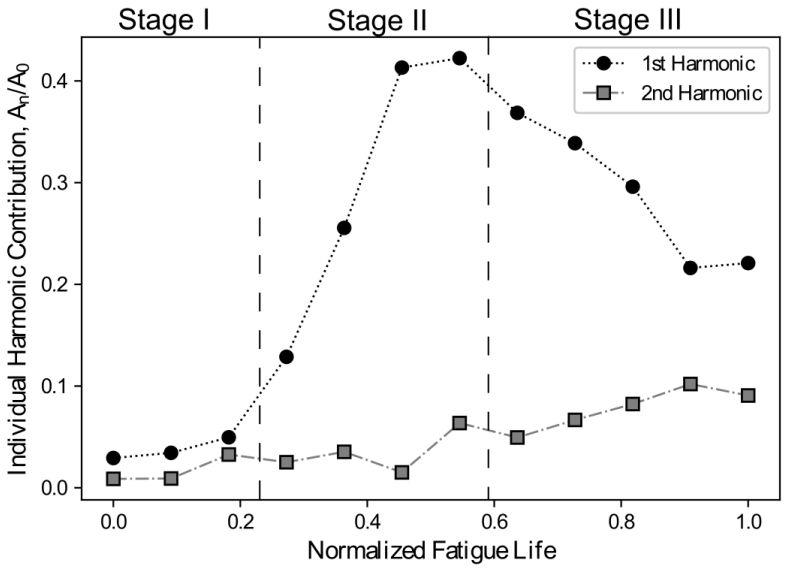

Figure 5.4: Typical individual harmonic evolution during corrosion fatigue tests.

Mean potential evolution

The mean corrosion potential presents an initial drop, followed by a less pronounced decrease for the rest of the exposure period for both loaded and no-loaded conditions 4.22. Under cyclic load the potential was consistently lower compared to the non-loaded one. Other effects, besides oxygen depletion, must be acting on the specimen under cyclic loading to justify this potential difference. It is known that during the first cycles the formation of numerous slip bands is expected for the specimen under cyclic loading [75]. Slip bands are fresh material prone to corrosion, and therefore slip bands formation results (anodic depolarization) in a shift to more active (more negative) potentials. This behavior is consistent with other studies [45] where a strong decrease in the mean corrosion potential was attributed to the formation of the slip bands, although stainless steel was used in that work. For more advanced lives, the potential difference can also be attributed to the evolution of accumulated plastic strain in the vicinity of the corrosion defects. At the end of the test, the presence of crack on the loaded specimen also generates locally anodic areas which can contribute to potential changes to more negative

regions.

5.3 Trunk-Conical Specimens

The use of truck-conical working section has shown clear advantages in relation to the classical cylindrical geometry. With this new geometry, different stress levels are submitted to the corrosive environment by the same duration, which allowed a more precise correlation between the applied stress amplitude and the level of corrosion. This approach has shown to be both cost and time effective, since with only one specimen it is possible to evaluate a wide range of stress amplitudes, reducing material costs and fatigue machine time. Evaluating a range of stresses over only one specimen also eliminates the effect of composition variations between different specimens, which is often seen for specimens machined from different batch of materials. However, it is also important to understand the main limitations and drawbacks of this type of analysis. Every surface feature (pits, cracks) has the potential to change the behavior of its vicinity which may lead misinterpretations of the degradation level in this region. It was verified that the presence of a macrocrack reduces abruptly the corroded area on its vicinity. The time frame of the test is defined by the higher stress zone since it is the rupture region. This period may be too short to properly evaluate all the corrosion fatigue effects on the lower stress region.

Chapter 6 – Conclusions and Future Work

6.1 Conclusions

The main objective of this research was to study the uniaxial behavior of the grade R4 steel simultaneously under corrosive environment and cyclic mechanical loading. Fully alternated ($R = -1$) and tension-tension ($R = 0.1$) tests were carried out with the fatigue lives varying between 10^3 and $2 \cdot 10^6$ cycles. The observed lives were compared to the in-air condition in order to evaluate the detrimental effects of the aggressive environment. The degradation mechanisms were correlated with the corrosion potential fluctuations due to cyclic loading corrosion-fatigue tests. Valuable information on the mechanisms of degradation of offshore steel under corrosion-fatigue condition is drawn from these measurements. A corrosion level quantitative analysis was carried out using the fraction of corroded area for different loading conditions as an index to describe the influence of environmental variables on the material.

Based on the obtained results, the following conclusions can be drawn:

- For steel under uniaxial cyclic loading, the corrosive environment reduces significantly the material lifetime before failure; a decrease in the corrosion fatigue life when compared to in-air fatigue was observed even for short periods of immersion. For lower stress amplitude no failure before 2 million cycles was observed for the in-air condition. Based on the extrapolations of the obtained fatigue curves, the fatigue life reduction due to the environment could reach several orders of magnitude. This analysis highlights how detrimental the corrosive environment can be, especially in the lower stress amplitude range.

- The mean stress causes a reduction of the observed life for both air fatigue and corrosion fatigue. The Smith-Watson-Topper parameter has shown to be a good option to predict the effects of the positive load ratio on the observed lives. Using this parameter, all the corrosion fatigue lives stayed within factor-of-two boundaries.

- The fraction of corroded surface area was determined by image processing of microscopical

images and correlated with both the time of exposure and the applied stress. This procedure allowed to determine a growth in the corroded area with the stress amplitude up to a threshold.

- SEM inspections revealed that lower mechanical amplitudes cause intergranular failure while the higher amplitudes cause transgranular failure, for the corrosion fatigue tests. Only transgranular failure was observed for the in-air fatigue tests.

- The use of trunk conical specimens associated with a corrosion level analysis is proposed and the effects of the stress amplitude, decoupled from the immersion time, on the corrosion fatigue failure. This approach also has shown to be time and material efficient since a range of stresses can be tested at once, with only one specimen. The major drawback of this approach if that the time until failure is determined by the section under the highest stress, which may lead to short exposure times depending on the set parameters.

- Electrochemical monitoring of corrosion fatigue of steel was made using samples under spontaneous condition, following only the corrosion potential. To the best of the author's knowledge, this was the first time this approach was used to study the corrosion fatigue behavior of low alloy steel. A strong correlation between the fluctuations of the corrosion potential and the cyclic applied load was observed and the three distinctive corrosion potential responses could be identified. Stage I, characterized by a sinusoidal signal, reveals a damage-free material under elastic straining. Stage II is assigned to the nucleation of pits and microcracks, revealed by distorted variation of the corrosion potential fluctuations. Stage III is characterized by an increase of the signal amplitude as the exposed area increases due to crack propagation. In stages II and III the presence of 1st and 2nd harmonic was identified, revealing secondary processes.

6.2 Future Work

Based on the studies already concluded, the following topics are proposed as suggestions of next steps regarding the research of the corrosion fatigue behavior of grade R4 steel on simulated seawater.

1) Characterization of different degradation features using the shape of the electrochemical potential.

Corrosion-fatigue experiments with pre-cracked specimens (without corrosion) and pre-corroded specimens (without cracks) can also be carried out. This set of experiments aims to isolate the effects of each degradation feature (corrosion and cracks) on the corrosion potential response of the material. The corrosion potential signal corresponding to the first cycles will be analysed. It is important to guarantee that signal is measured before corrosion takes place for the pre-cracked specimen and before the nucleation of microcracks for the pre-corroded

specimen. The electrochemical signal of each mechanism acting isolated from each other on the material will be useful to understand more complicated situations where all mechanisms are present.

2) Corrosion-fatigue experiments with active-passive specimens.

Changing the applied electrochemical potential to a point where a passive film is thermodynamically stable will be important to have a better knowledge of the corrosion-fatigue condition observed on offshore structures. In this set of experiments the current signal can be measured with a controlled potential. The shape of current response can be used to identify the nucleation of cracks during the experiment. Similar experiments on iron bars were conducted by Tada [19]. The current monitoring carries valuable information about the kinetics of the electrochemical processes.

3) Multiaxial corrosion-fatigue tests.

Offshore mooring link are subjected to multiaxial loading. Various multiaxial criteria based on different modeling have been proposed. However, the corrosive effect combined with the multiaxial loading was not normally investigated. Pioneer multiaxial experiments were conducted by Huang and co-authors [15] on stainless steel immersed in NaCl solution. The literature lacks of information on the multiaxial behavior of offshore steels, such as the grade R4, specially when combining multiaxial loads and corrosion environment. The experimental setup proposed in this work is suitable for multiaxial corrosion-fatigue testing and data obtained from this experiments may interest both academic and industrial community.

References

[1] *Number of wells x Output.* http://www.petrobras.com.br/en/our-activities/performance-areas/oil-and-gas-exploration-and-production/pre-salt/. Accessed: 2019-10-12.

[2] *The State of the Art of the Brazilian Pre-Salt Exploration.* http://www.anp.gov.br/images/Palestras/Abelha_Marina_Brazilian-Pre-Salt_APPEX_2019MAR6.pdf. Accessed: 2019-10-12.

[3] *Floating production system JIP FPS mooring integrity. Research Report 444 prepared for the Health and Safety Executive.* Noble Denton Europe Limited., 2006.

[4] *Design and analysis of stationkeeping systems for floating structures - 4th Edition.* American Petroleum Institute, 2018.

[5] R. B. Gordon, M. G. Brown and E. M. Allen. "Mooring Integrity Management: A State-of-the-Art Review". In: Offshore Technology Conference, 2014.

[6] E. Fontaine, A. Kilner, C. Carra, D. Washington, K. Ma, A. Phadke, D. Laskowski and G. Kusinski. "Industry Survey of Past Failures, Pre-emptive Replacements and Reported Degradations for Mooring Systems of Floating Production Units". In: Offshore Technology Conference, 2014.

[7] K. tung Ma, H. Shu, P. Smedley, D. L'Hostis and A. Duggal. "A Historical Review on Integrity Issues of Permanent Mooring Systems". In: Offshore Technology Conference, 2013.

[8] E. Fontaine, A. Potts, K. tung Ma, A. Arredondo and R. E. Melchers. "SCORCH JIP: Examination and Testing of Severely-Corroded Mooring Chains From West Africa". In: Offshore Technology Conference, 2012.

[9] L. Rampi and P. Vargas. *Methodology to account for corrosive environment on accelerated fatigue test on mooring chains within the chain out of plane bending (OPB) fatigue Joint Industry Project (JIP). Fatigue design 2011 : Recueil de conférences proceedings.* CETIM, 2011.

[10] T. Palin-Luc, R. Pérez-Mora, C. Bathias, G. Domínguez, P. C. Paris and J. L. Arana. "Fatigue crack initiation and growth on a steel in the very high cycle regime with sea water corrosion". In: *Engineering Fracture Mechanics* 77.11 (2010), pp. 1953–1962.

[11] R. Pérez-Mora, T. Palin-Luc, C. Bathias and P. C. Paris. “Very high cycle fatigue of a high strength steel under sea water corrosion: A strong corrosion and mechanical damage coupling”. In: *International Journal of Fatigue* 74 (2015), pp. 156–165.

[12] J. Fernández, W. Storesund and J. Navas. “Fatigue Performance of Grade R4 and R5 Mooring Chains in Seawater”. In: *Volume 1A: Offshore Technology*. ASME, 2014.

[13] R. Nevshupa, I. Martinez, S. Ramos and A. Arredondo. “The effect of environmental variables on early corrosion of high–strength low–alloy mooring steel immersed in seawater”. In: *Marine Structures* 60 (2018), pp. 226–240.

[14] C. Melis, P. Jean and P. Vargas. “Out-of-Plane Bending Testing of Chain Links”. In: *24th International Conference on Offshore Mechanics and Arctic Engineering: Volume 3*. ASME, 2005.

[15] Y.-H. Huang, S.-T. Tu, F.-Z. Xuan and T. Itoh. “Corrosion fatigue behaviour of 304 stainless steel under proportional and non-proportional multiaxial loading condition”. In: *Fatigue & Fracture of Engineering Materials & Structures* 37.4 (2013), pp. 436–445.

[16] S. Beretta, M. Carboni, G. Fiore and A. L. Conte. “Corrosion–fatigue of A1N railway axle steel exposed to rainwater”. In: *International Journal of Fatigue* 32.6 (2010), pp. 952–961.

[17] M. E. May, T. Palin-Luc, N. Saintier and O. Devos. “Effect of corrosion on the high cycle fatigue strength of martensitic stainless steel X12CrNiMoV12-3”. In: *International Journal of Fatigue* 47 (2013), pp. 330–339.

[18] E. Tada, K. Noda, S. Kumai and T. Tsuru. “Monitoring of corrosion fatigue cracking using harmonic analysis of current responses induced by cyclic stressing”. In: *Corrosion Science* 46.6 (2004), pp. 1549–1563.

[19] E. Tada. “Detection of corrosion fatigue cracking through current responses induced by cyclic stressing”. In: *Corrosion Science* 49.1 (2007), pp. 248–254.

[20] M. Klein, G. Frieling and F. Walther. “Corrosion fatigue assessment of creep-resistant magnesium alloys DieMag422 and AE42”. In: *Engineering Fracture Mechanics* 185 (2017), pp. 33–45.

[21] K. G. Denbigh. *The Principles of Chemical Equilibrium: With Applications in Chemistry and Chemical Engineering*. 4th ed. Cambridge University Press, 1981.

[22] E. A. Ticianelli. *Eletroquímica. Princípios e Aplicações*. Edusp, 2013.

[23] P. R. Roberge. *Corrosion Engineering: Principles and Practice*. McGraw-Hill Education, 2008.

[24] M. G. Fontana. *Corrosion Engineering*. McGraw-Hill Book Company, 1985.

[25] *Impedance Spectroscopy: Theory, Experiment, and Applications*. Wiley-Interscience, 2005.

[26] N. Sato. “Basics of Corrosion Chemistry”. In: *Green Corrosion Chemistry and Engineering*. Wiley-VCH Verlag GmbH & Co. KGaA, 2011, pp. 1–32.

[27] M. Pourbaix. *Atlas of Electrochemical Equilibria in Aqueous Solutions*. National Association of Corrosion, 1974.

[28] N. O. Larrosa, R. Akid and R. A. Ainsworth. "Corrosion-fatigue: a review of damage tolerance models". In: *International Materials Reviews* 63.5 (2017), pp. 283–308.

[29] G. Brug, A. van den Eeden, M. Sluyters-Rehbach and J. Sluyters. "The analysis of electrode impedances complicated by the presence of a constant phase element". In: *Journal of Electroanalytical Chemistry and Interfacial Electrochemistry* 176.1-2 (1984), pp. 275–295.

[30] M. E. Orazem and B. Tribollet. *Electrochemical Impedance Spectroscopy*. en. The ECS Series of Texts and Monographs. Hoboken, NJ: Wiley-Blackwell, Aug. 2008.

[31] M. Müller. "Theoretical Considerations on Corrosion Fatigue Crack Initiation". In: *Metallurgical Transactions A* 13.4 (1982), pp. 649–655.

[32] R Akid. "The Role of Stress-Assisted Localized Corrosion in the Development of Short Fatigue Cracks". In: *Effects of the Environment on the Initiation of Crack Growth*. ASTM International, pp. 3–3–15.

[33] Y. Kondo. "Prediction of Fatigue Crack Initiation Life Based on Pit Growth". In: *CORROSION* 45.1 (1989), pp. 7–11.

[34] D. Hoeppner. "Model for Prediction of Fatigue Lives Based Upon a Pitting Corrosion Fatigue Process". In: *Fatigue Mechanisms*. ASTM International, pp. 841–841–30.

[35] T. C. Lindley, P. Mcintyre and P. J. Trant. "Fatigue-crack initiation at corrosion pits". In: *Metals Technology* 9.1 (1982), pp. 135–142.

[36] B. Yan, G. Farrington and C. Laird. "Strain localization in single crystals of copper cycled in 0.1 M perchloric acid solution under potential control". In: *Acta Metallurgica* 33.8 (1985), pp. 1533–1545.

[37] Q. Y. Wang, R. M. Pidaparti and M. J. Palakal. "Comparative Study of Corrosion-Fatigue in Aircraft Materials". In: *AIAA Journal* 39.2 (2001), pp. 325–330.

[38] L. Weng, J. Zhang, S. Kalnaus, M. Feng and Y. Jiang. "Corrosion fatigue crack growth of AISI 4340 steel". In: *International Journal of Fatigue* 48 (2013), pp. 156–164.

[39] S. Suresh and R. O. Ritchie. "Propagation of short fatigue cracks". In: *International Materials Reviews* 29.1 (1984), pp. 445–475.

[40] R. Ritchie and J. Lankford. "Small fatigue cracks: A statement of the problem and potential solutions". In: *Materials Science and Engineering* 84 (1986), pp. 11–16.

[41] S. G. Lee and I. S. Kim. "Strain Rate Effects on the Fatigue Crack Growth of SA508 Cl.3 Reactor Pressure Vessel Steel in High-Temperature Water Environment". In: *Journal of Pressure Vessel Technology* 123.2 (2001), pp. 173–178.

[42] X. Wu and Y. Katada. "Strain-rate dependence of low cycle fatigue behavior in a simulated BWR environment". In: *Corrosion Science* 47.6 (2005), pp. 1415–1428.

[43] H. Seifert and S. Ritter. “Corrosion fatigue crack growth behaviour of low-alloy reactor pressure vessel steels under boiling water reactor conditions”. In: *Corrosion Science* 50.7 (2008), pp. 1884–1899.

[44] E. Tada, R. Tsuru and R. Oltra. “Synchronised current analysis for corrosion fatigue of iron.” In: (1996).

[45] T. Magnin. “Recent Advances for Corrosion Fatigue Mechanisms.” In: *ISIJ International* 35.3 (1995), pp. 223–233.

[46] Y. Li, G. Farrington and C. Laird. “Cyclic response-electrochemical interaction in mono- and polycrystalline AISI 316L stainless steel in H2SO4 solution — I. The influence of mechanical strain on the transient dissolution behavior during corrosion fatigue”. In: *Acta Metallurgica et Materialia* 41.3 (1993), pp. 693–708.

[47] R. Akid and K. J. Miller. “Short fatigue crack growth behaviour of a low carbon steel under corrosion fatigue conditions”. In: *Fatigue & Fracture of Engineering Materials and Structures* 14.6 (1991), pp. 637–649.

[48] H Mughrabi, R Wang, K Differt and U Essmann. “Fatigue Crack Initiation by Cyclic Slip Irreversibilities in High-Cycle Fatigue”. In: *Fatigue Mechanisms: Advances in Quantitative Measurement of Physical Damage*. Vol. 5. ASTM International, pp. 5–41.

[49] J. A. Ewing and J. C. M. Humfrey. “VI. The fracture of metals under repeated alternations of stress”. In: *Philosophical Transactions of the Royal Society of London. Series A* 200.321-330 (1903), pp. 241–250.

[50] D. F. Socie. *Multiaxial Fatigue*. SAE International, 1999.

[51] B. S. Jr. *ASM Handbook: Corrosion : Fundamentals, Testing, and Protection*. ASM International, 2003.

[52] S. Srivatsan and T. S. Sudarshan. “Mechanisms of fatigue crack initiation in metals: role of aqueous environments”. In: *Journal of Materials Science* 23.5 (1988), pp. 1521–1533.

[53] T. Zhao, Z. Liu, C. Du, C. Dai, X. Li and B. Zhang. “Corrosion fatigue crack initiation and initial propagation mechanism of E690 steel in simulated seawater”. In: *Materials Science and Engineering: A* 708 (2017), pp. 181–192.

[54] L. L. Shreir, R. A. Jarman and G. T. Burstein. *Corrosion - Volume 1, 3rd ed.* Woburn, MA: Butterworth-Heinemann, 1994.

[55] D. Whitman and R. Evans. In: *J. Iron Steel Inst.* 165 (1950), p. 72.

[56] W. Zhao, Y. Wang, T. Zhang and Y. Wang. “Study on the mechanism of high-cycle corrosion fatigue crack initiation in X80 steel”. In: *Corrosion Science* 57 (2012), pp. 99–103.

[57] I. Cornet and S. Golan. “Influence of Temperature on Corrosion Fatigue”. In: *CORROSION* 15.5 (1959), pp. 58–64.

[58] O. Devereux, A. McEvily and Staehle. *Corrosion Fatigue: Chemistry, Mechanics and Microstructure*. International corrosion conference series. National Association of Corrosion Engineers, Houston TX, 1972.

[59] F. Abbasi. "A review study on Corrosion Fatigue and its related testing methodologies". In: *Journal of Mechanical Engineering Research* 2.1 (2019), pp. 17–24.

[60] S.-X. Li and R. Akid. "Corrosion fatigue life prediction of a steel shaft material in seawater". In: *Engineering Failure Analysis* 34 (2013), pp. 324–334.

[61] L. M. B. Infante. "Corrosion Fatigue testing on steel grades with different heat treatment used in rock-drilling applications". MSc thesis. KTH Royal Institute of Technology, 2016.

[62] S. Luo, M. Liu and X. Lin. "Corrosion fatigue behavior of S135 high-strength drill pipe steel in a simulated marine environment". In: *Materials and Corrosion* 70.4 (2018), pp. 688–697.

[63] S. Jafari, R. S. Raman and C. H. Davies. "Corrosion fatigue of a magnesium alloy in modified simulated body fluid". In: *Engineering Fracture Mechanics* 137 (2015), pp. 2–11.

[64] J. A. Moreto, F. A. P. Júnior, C. I. S. Maciel, L. H. C. Bonazzi, J. F. L. Júnior, C. O. F. T. Ruchert and W. W. B. Filho. "Environmentally-assisted Fatigue Crack Growth in AA7050-T73511 Al Alloy and AA2050-T84 Al-Cu-Li Alloy". In: *Materials Research* 18.6 (2015), pp. 1291–1297.

[65] E. Mamiya, F. Castro, G. Ferreira, E. N. Filho, F. Canut, R. Neves and L. Malcher. "Fatigue of mooring chain links subjected to out-of-plane bending: Experiments and modeling". In: *Engineering Failure Analysis* 100 (2019), pp. 206 –213.

[66] L. Rampi and P. Vargas. "Fatigue Testing of Out-of-Plane Bending Mechanism of Chain Links". In: ASMEDC, 2006.

[67] *Offshore Mooring Chain. Standard UR W22 Rev6 CLN UK*. Standard. International Association Classification Societies, 2016.

[68] *Standard Practice for Conducting Force Controlled Constant Amplitude Axial Fatigue Tests of Metallic Materials*. Standard. West Conshohocken, PA 19428-2959, United States: American Society for Testing and Materials, 2002.

[69] *Standard Practice for Corrosion Fatigue Testing of Metallic Implant Materials*. Standard. West Conshohocken, PA 19428-2959, United States: American Society for Testing and Materials, 2004.

[70] F. A. Canut, A. M. Simões, L. Reis, M. Freitas, I. N. Bastos, F. C. Castro and E. N. Mamiya. "Monitoring of corrosion-fatigue degradation of grade R4 steel using an electrochemical-mechanical combined approach". In: *Fatigue & Fracture of Engineering Materials & Structures* 42.11 (2019), pp. 2509–2519.

[71] K. Smith, P. Watson and T. Topper. "A Stress-Strain Function for the Fatigue of Metals". In: *Journal of Materials* 5.4 (1970), pp. 767–778.

[72] M. Morgantini, D. MacKenzie, T. Comlekci and R. van Rijswick. “The Effect of Mean Stress on Corrosion Fatigue Life”. In: *Procedia Engineering* 213 (2018), pp. 581–588.

[73] D. Duquette and H. Uhlig. “Critical Reaction Rate for Corrosion Fatigue Of 0.18 % Carbon Steel and the Effect of pH”. In: *ASM TRANS QUART* 62 (1969), pp. 839–845.

[74] G. Gabetta. “A method to measure electrochemical potential at the tip of a growing crack during an environmental fatigue test”. In: *Fatigue & Fracture of Engineering Materials and Structures* 5.3 (1982), pp. 215–220.

[75] P. P. Milella. *Fatigue and Corrosion in Metals*. Springer Milan, 2013.

[76] L. L. Shreir, R. A. Jarman and G. T. Burstein. *Corrosion - Volume 2, 3rd ed.* Woburn, MA: Butterworth-Heinemann, 1994.

[77] A. Turnbull. “A theoretical evaluation of the influence of mechanical variables on the concentration of oxygen in a corrosion fatigue crack”. In: *Corrosion Science* 22.9 (1982), pp. 877–893.

[78] O. Basquin. “The exponential law of endurance tests”. In: 10 (1910), pp. 625–630.

[79] S. Ortner, C. Laird and G. Farrington. “The electrochemical response of copper single crystals to corrosion-fatigue in an aqueous, oxide-forming environment”. In: *Acta Metallurgica* 35.4 (1987), pp. 867–874.

Appendix A – Corrosion Potential Measurements

In this section, all the corrosion potential measurements obtained during the corrosion fatigue tests were shown. The measurements were carried out every 5000 seconds, *i.e.* 5000 cycles at a load frequency of 1.0 Hz. All tests were performed at fully reversed load ratio ($R = -1$) and the amplitudes tested were: 400 MPa, 450 MPa, 500 MPa and 550 MPa.

The detailed examination of the corrosion potential revealed that small cyclic fluctuations overlap the mean value, with the same frequency of the mechanical loading. The following stages of corrosion potential response were observed for all the load amplitudes tested: (i) Sine-wave response at the beginning of the test followed by attenuation of the signal, but without significant distortion, (ii) distorted signals at the middle portion of the test and (iii) increase of the distorted signal amplitude at the end.

The results in this appendix are organized as bellow:

A.1 Results for a stress amplitude of 400 MPa

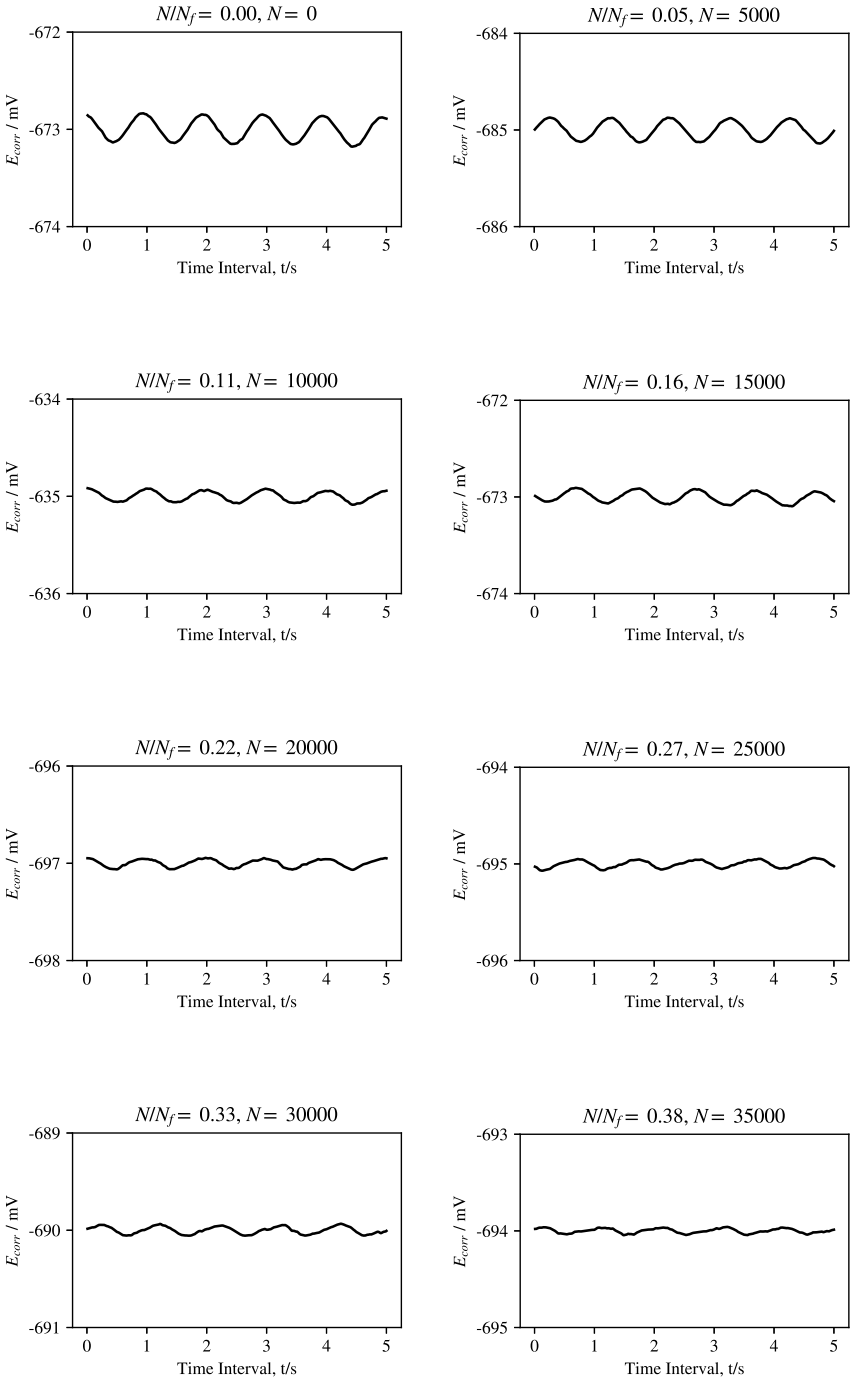

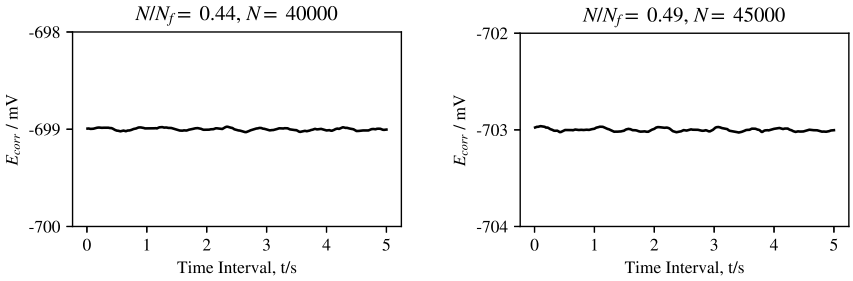
N/N_f = 0.44, N = 40000
-698
-699
-700
E_{corr} / mV
0
1
2
3
4
5
Time Interval, t/s

N/N_f = 0.49, N = 45000
-702
-703
-704
E_{corr} / mV
0
1
2
3
4
5
Time Interval, t/s

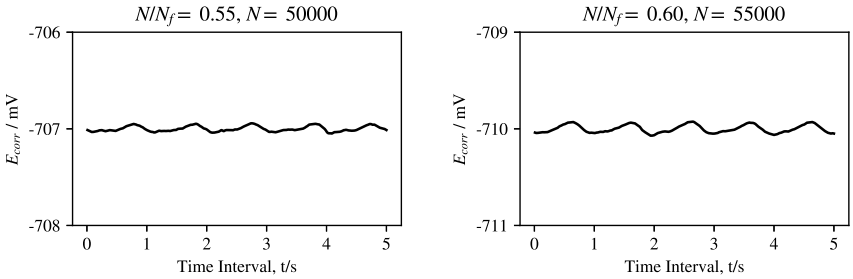
N/N_f = 0.55, N = 50000
-706
-707
-708
E_{corr} / mV
0
1
2
3
4
5
Time Interval, t/s

N/N_f = 0.60, N = 55000
-709
-710
-711
E_{corr} / mV
0
1
2
3
4
5
Time Interval, t/s

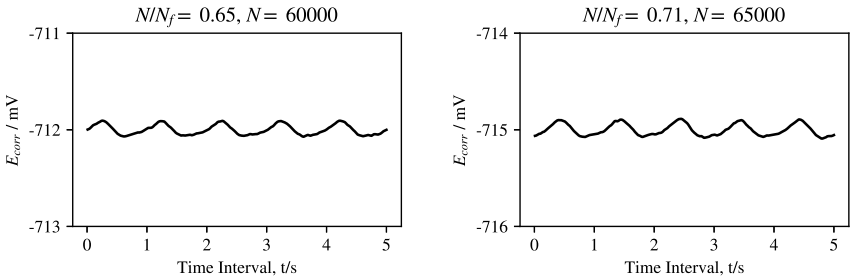
N/N_f = 0.65, N = 60000
-711
-712
-713
E_{corr} / mV
0
1
2
3
4
5
Time Interval, t/s

N/N_f = 0.71, N = 65000
-714
-715
-716
E_{corr} / mV
0
1
2
3
4
5
Time Interval, t/s

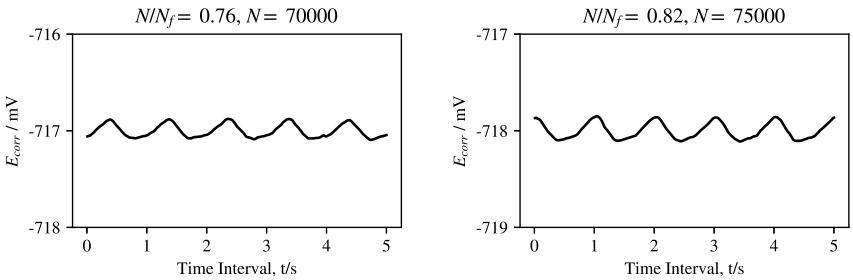
N/N_f = 0.76, N = 70000
-716
-717
-718
E_{corr} / mV
0
1
2
3
4
5
Time Interval, t/s

N/N_f = 0.82, N = 75000
-717
-718
-719
E_{corr} / mV
0
1
2
3
4
5
Time Interval, t/s

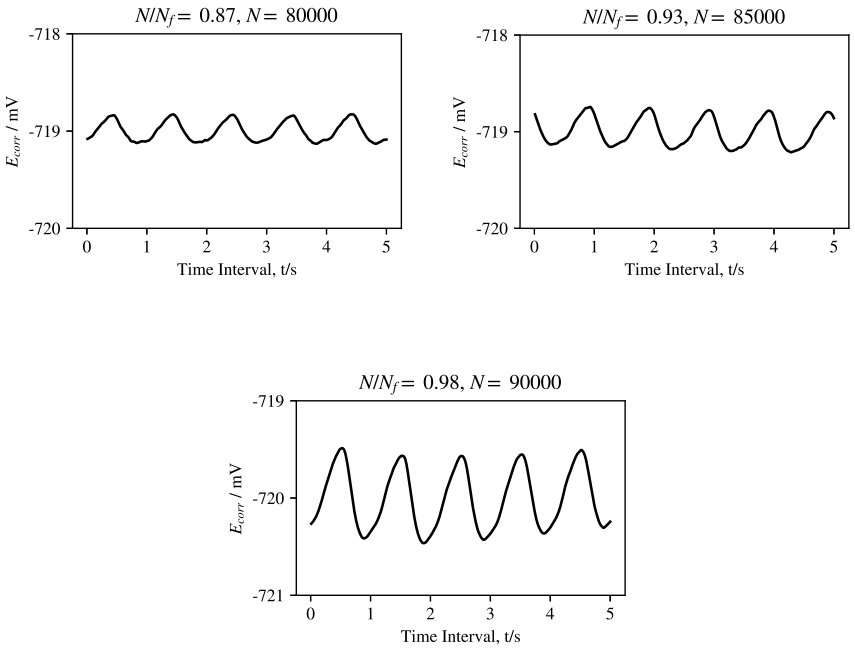

Corrosion potential measurements carried out during a corrosion fatigue test under a nominal stress amplitude of 400 MPa

A.2 Results for a stress amplitude of 450 MPa

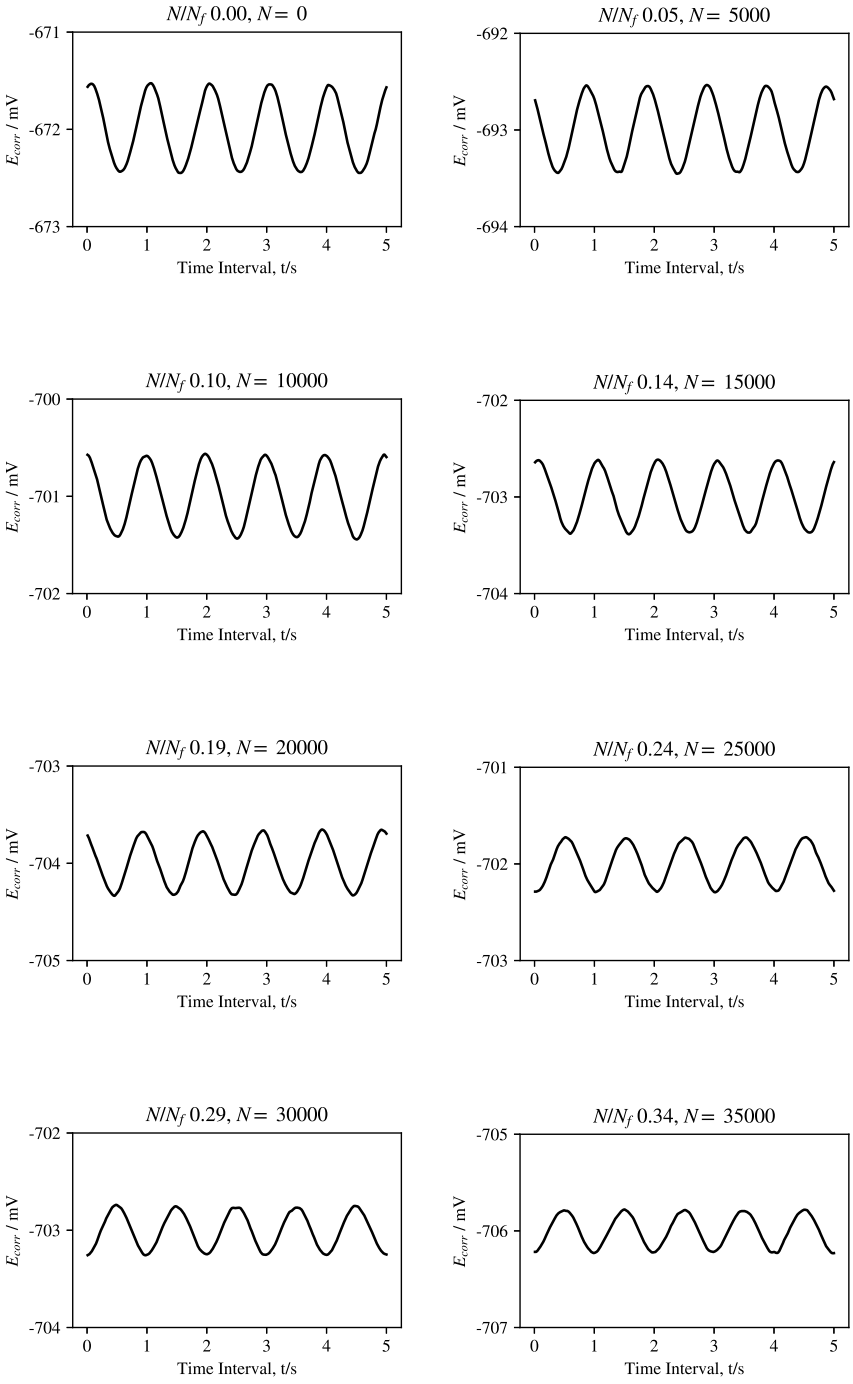

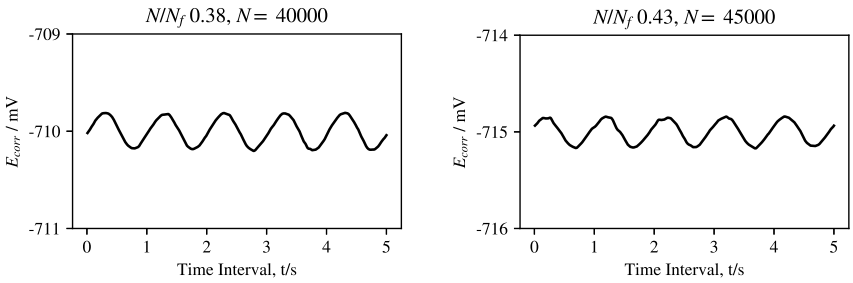
N/N_f 0.38, $N=$ 40000
E_{corr} / mV
-709
-710
-711
0 1 2 3 4 5
Time Interval, t/s

N/N_f 0.43, $N=$ 45000
E_{corr} / mV
-714
-715
-716
0 1 2 3 4 5
Time Interval, t/s

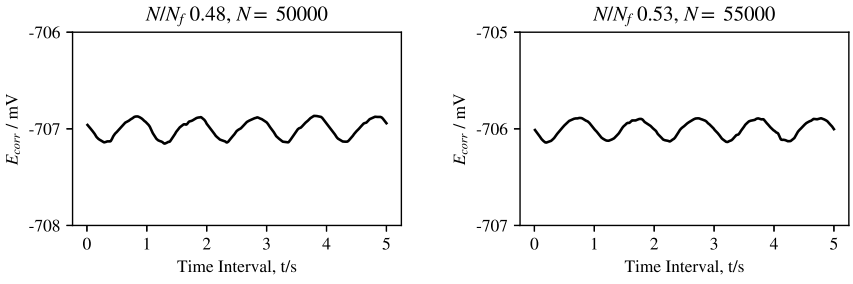
N/N_f 0.48, $N=$ 50000
E_{corr} / mV
-706
-707
-708
0 1 2 3 4 5
Time Interval, t/s

N/N_f 0.53, $N=$ 55000
E_{corr} / mV
-705
-706
-707
0 1 2 3 4 5
Time Interval, t/s

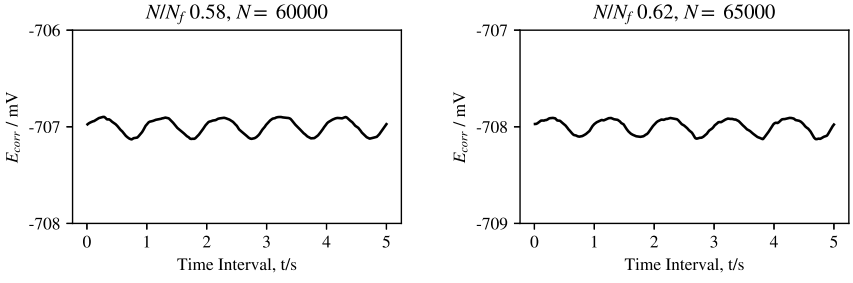
N/N_f 0.58, $N=$ 60000
E_{corr} / mV
-706
-707
-708
0 1 2 3 4 5
Time Interval, t/s

N/N_f 0.62, $N=$ 65000
E_{corr} / mV
-707
-708
-709
0 1 2 3 4 5
Time Interval, t/s

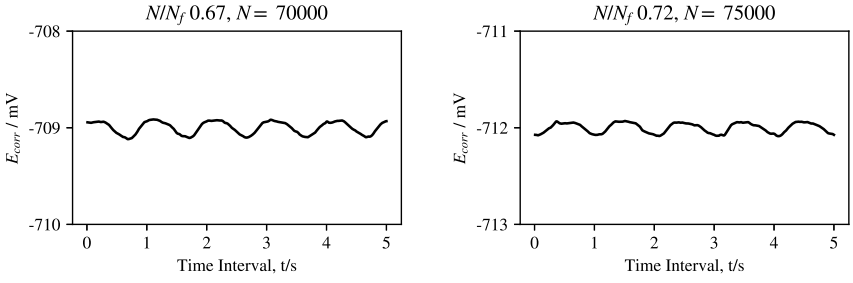
N/N_f 0.67, $N=$ 70000
E_{corr} / mV
-708
-709
-710
0 1 2 3 4 5
Time Interval, t/s

N/N_f 0.72, $N=$ 75000
E_{corr} / mV
-711
-712
-713
0 1 2 3 4 5
Time Interval, t/s

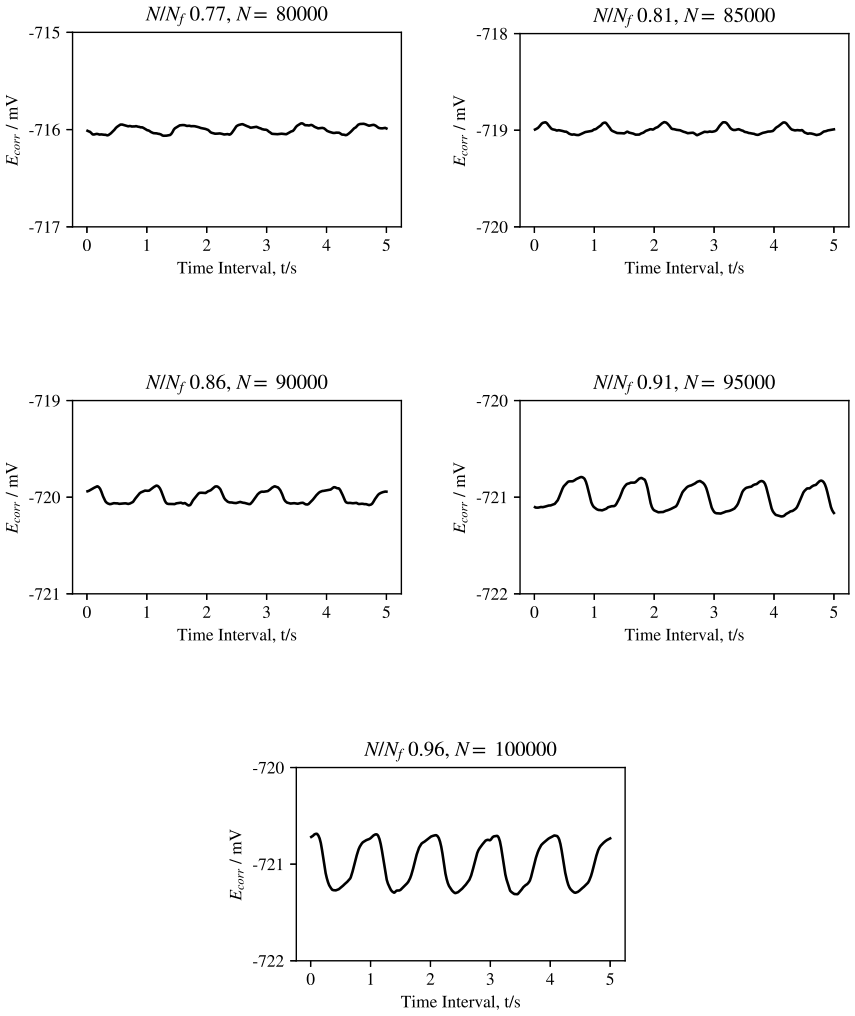

Corrosion potential measurements carried out during a corrosion fatigue test under a nominal stress amplitude of 450 MPa

A.3 Results for a stress amplitude of 500 MPa

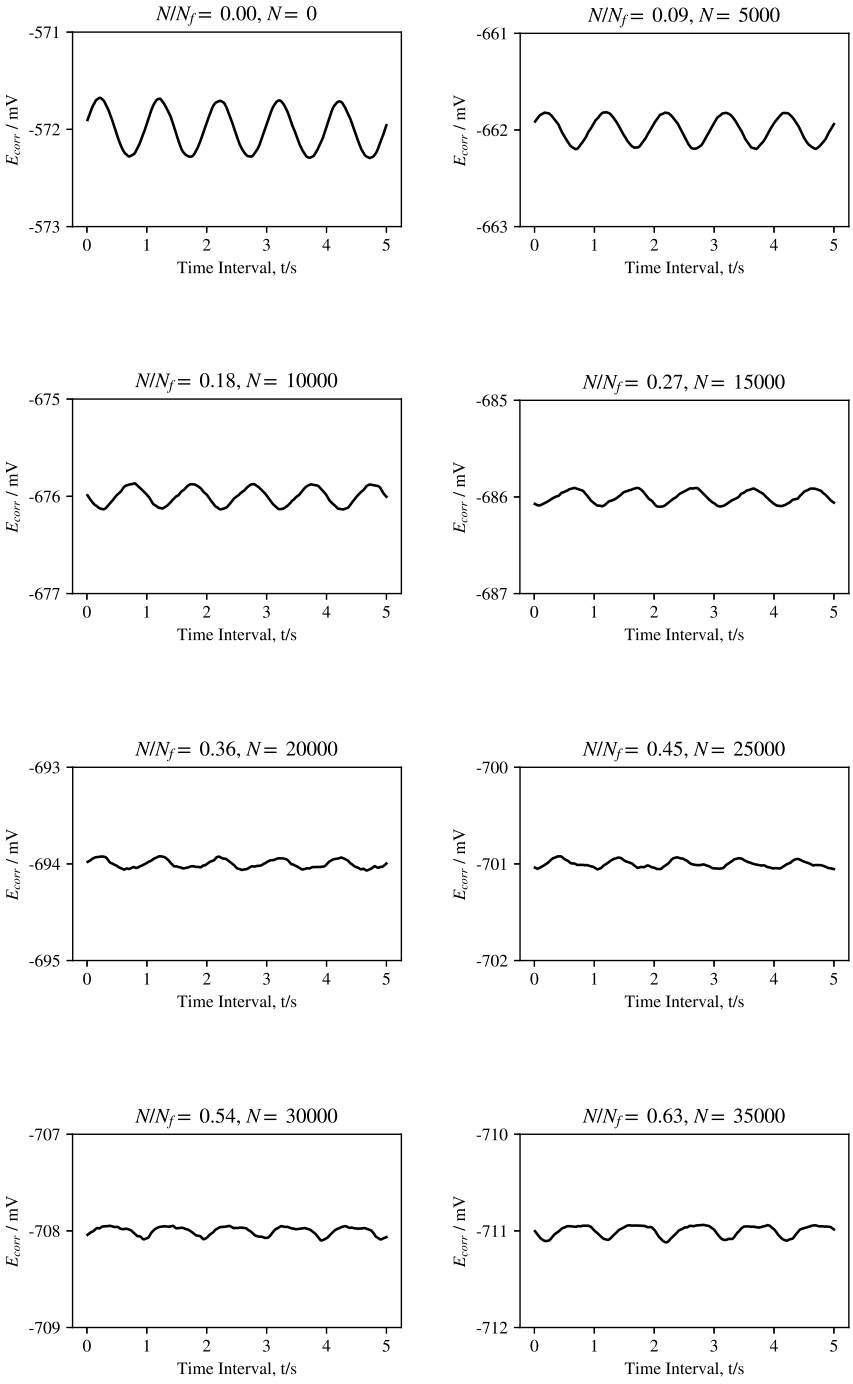

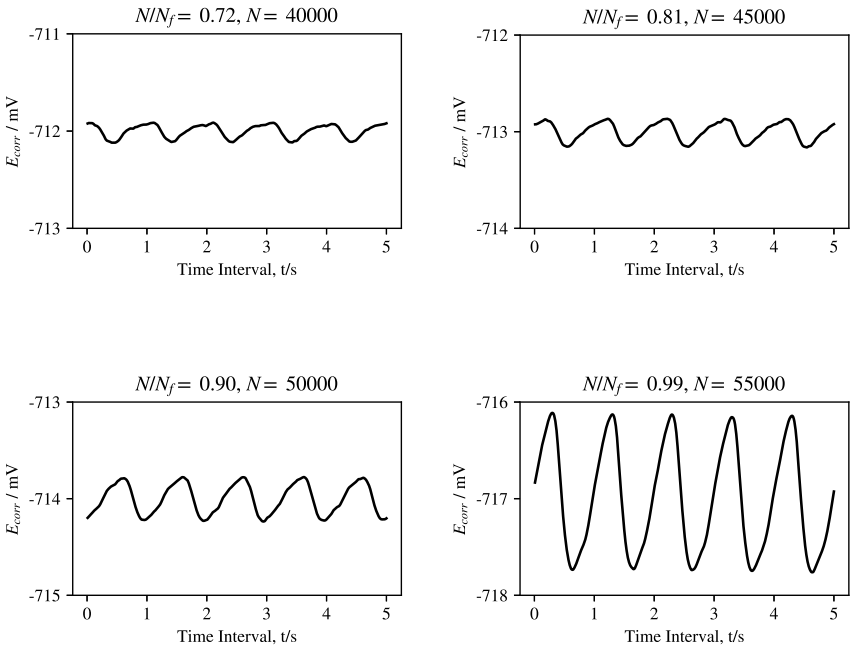

Corrosion potential measurements carried out during a corrosion fatigue test under a nominal stress amplitude of 500 MPa

A.4 Results for a stress amplitude of 550 MPa

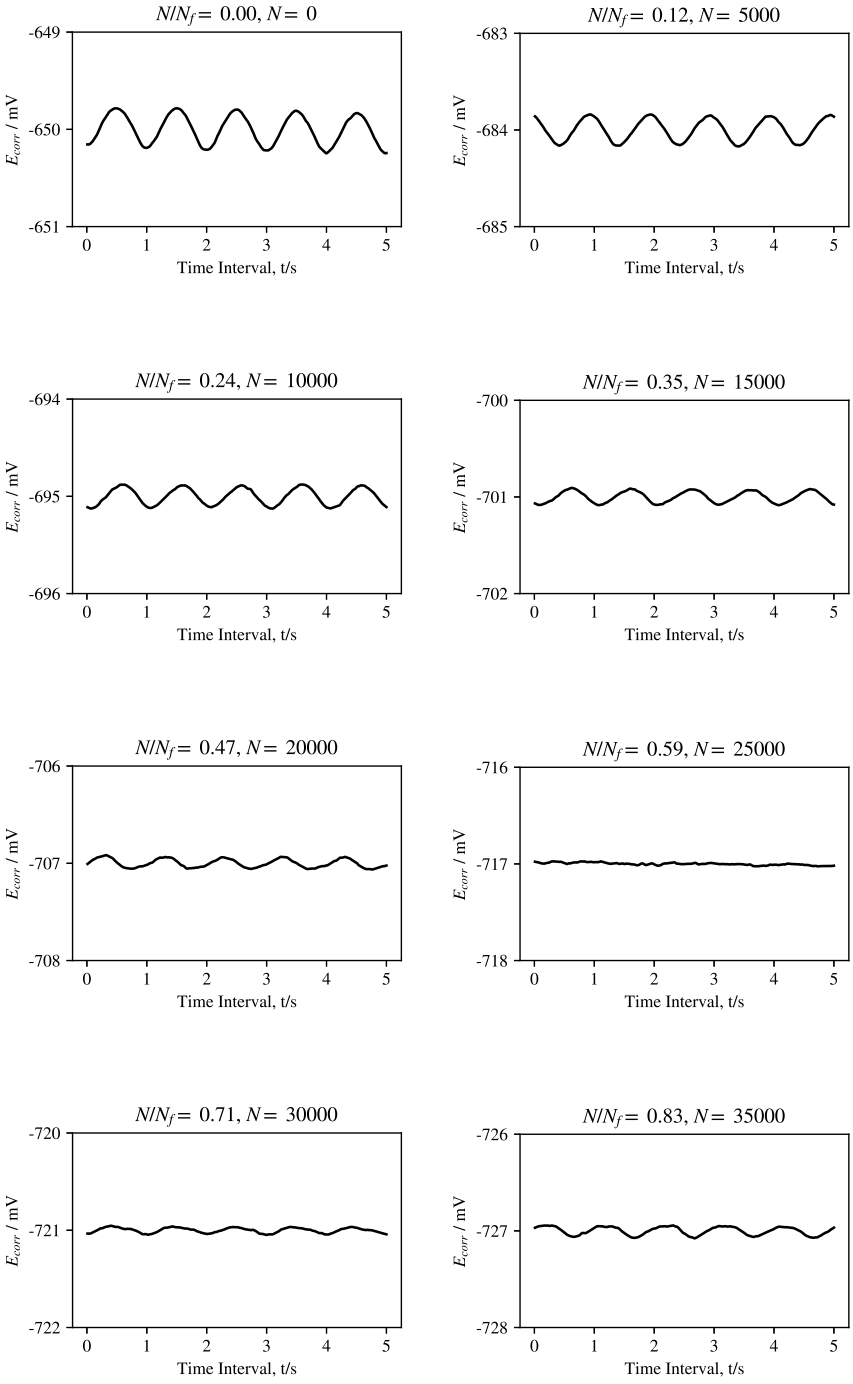

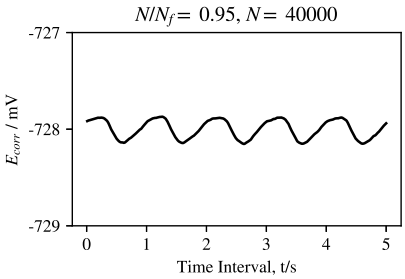

Corrosion potential measurements carried out during a corrosion fatigue test under a nominal stress amplitude of 550 MPa

Appendix B – Corrosion Potential Measurements

Representative images used to calculate the fraction of corroded area on the cylindrical and trunk conical specimens as well as the images of the reference sample (pure immersion) are shown bellow. All tests were carried out at a load frequency of 1.0 Hz, except when described otherwise.

B.1 Reference specimen - No load

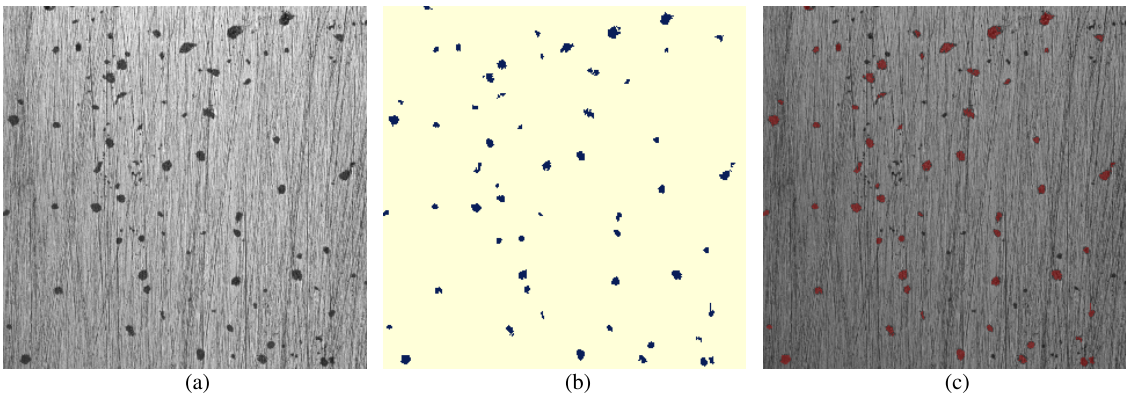

(a) (b) (c)

Figure B.1: Representative images for the pure immersion condition (no load) used to perform the corrosion level quantitative analysis. (a) Rough image, (b) detected corroded areas and (c) verification step.

B.2 Cylindrical Specimens, R = -1

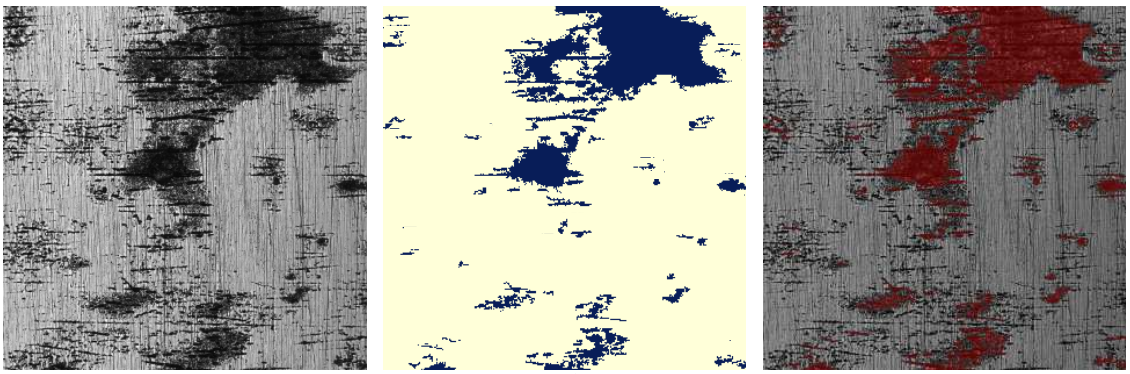

(a) (b) (c)

Figure B.2: Representative images of the specimen tested under $S_a = 250$ MPa, $R = -1$ load ratio used to perform the corrosion level quantitative analysis. (a) Rough image, (b) detected corroded areas and (c) verification step.

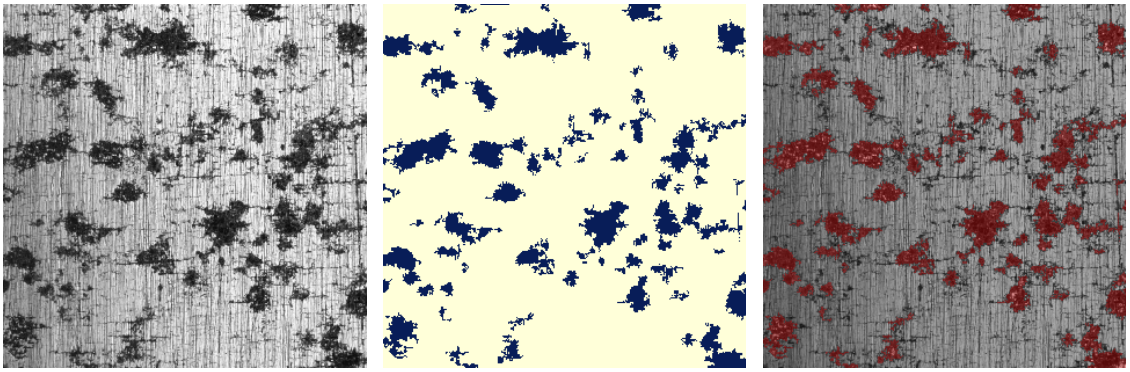

(a) (b) (c)

Figure B.3: Representative images of the specimen tested under $S_a = 300$ MPa, $R = -1$ load ratio used to perform the corrosion level quantitative analysis. (a) Rough image, (b) detected corroded areas and (c) verification step.

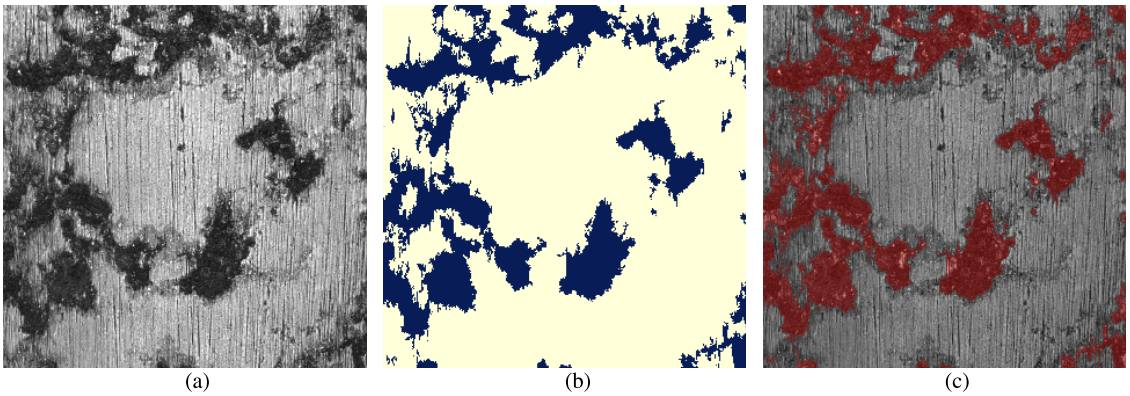

(a) (b) (c)

Figure B.4: Representative images of the specimen tested under $S_a = 350$ MPa, $R = -1$ load ratio used to perform the corrosion level quantitative analysis. (a) Rough image, (b) detected corroded areas and (c) verification step.

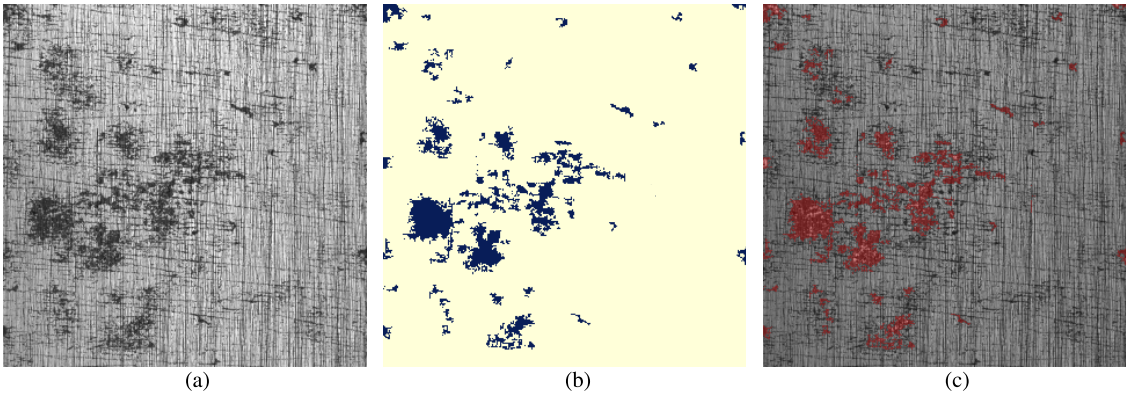

(a) (b) (c)

Figure B.5: Representative images of the specimen tested under $S_a = 375$ MPa, $R = -1$ load ratio used to perform the corrosion level quantitative analysis. (a) Rough image, (b) detected corroded areas and (c) verification step.

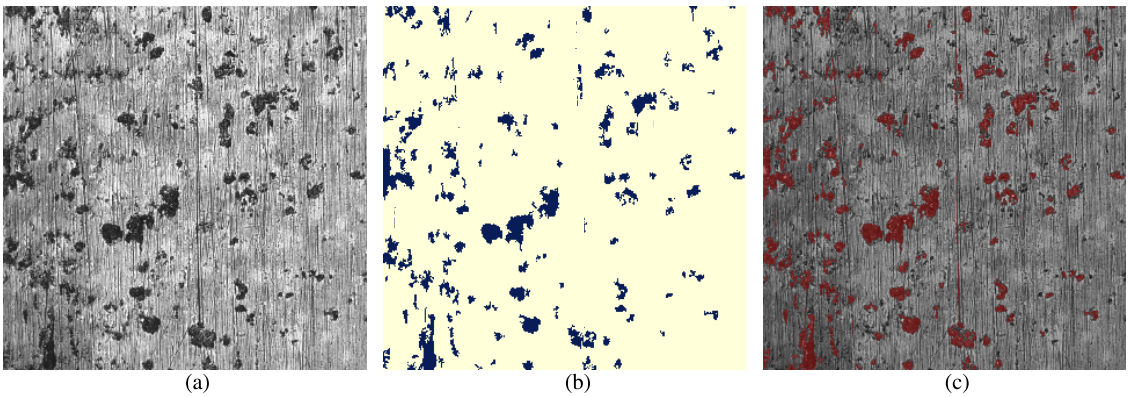

(a) (b) (c)

Figure B.6: Representative images of the specimen tested under $S_a = 400$ MPa, $R = -1$ load ratio used to perform the corrosion level quantitative analysis. (a) Rough image, (b) detected corroded areas and (c) verification step.

B.3 Cylindrical Specimens, R = 0.1

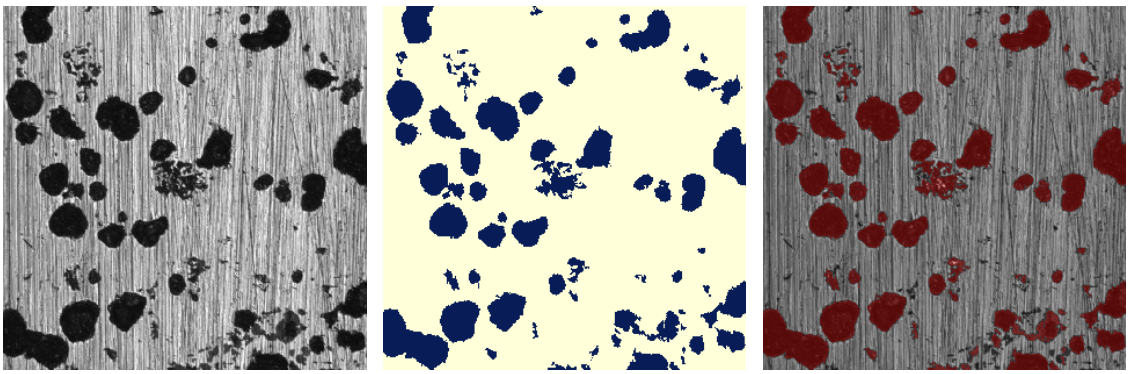

(a) (b) (c)

Figure B.7: Representative images of the specimen tested under $SWT = 250$ MPa, $R = 0.1$ load ratio used to perform the corrosion level quantitative analysis. (a) Rough image, (b) detected corroded areas and (c) verification step.

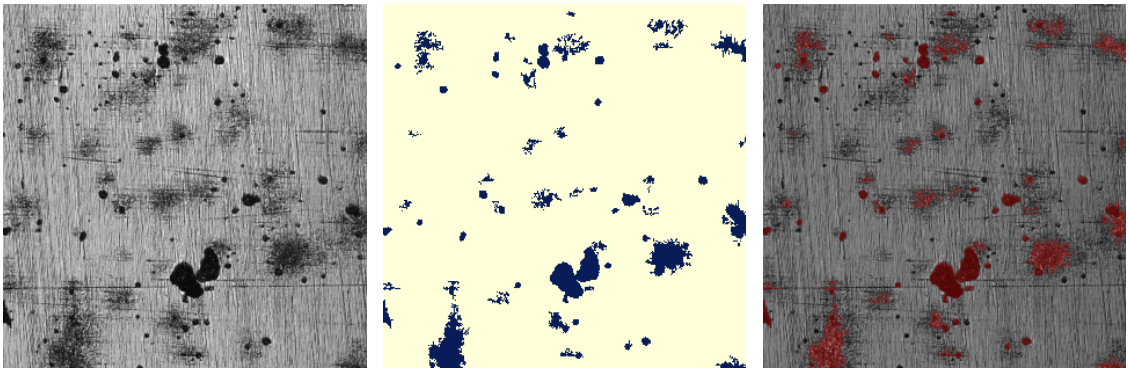

(a) (b) (c)

Figure B.8: Representative images of the specimen tested under $SWT = 300$ MPa, $R = 0.1$ load ratio used to perform the corrosion level quantitative analysis. (a) Rough image, (b) detected corroded areas and (c) verification step.

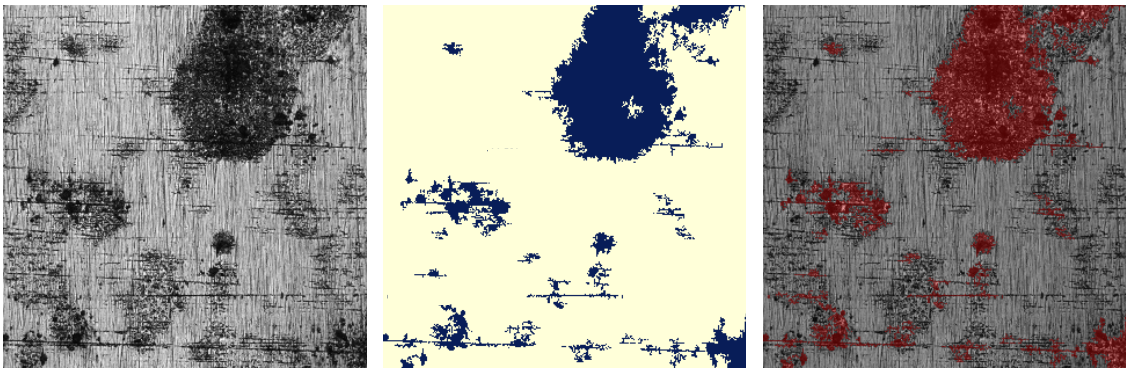

(a) (b) (c)

Figure B.9: Representative images of the specimen tested under $SWT = 350$ MPa, $R = 0.1$ load ratio used to perform the corrosion level quantitative analysis. (a) Rough image, (b) detected corroded areas and (c) verification step.

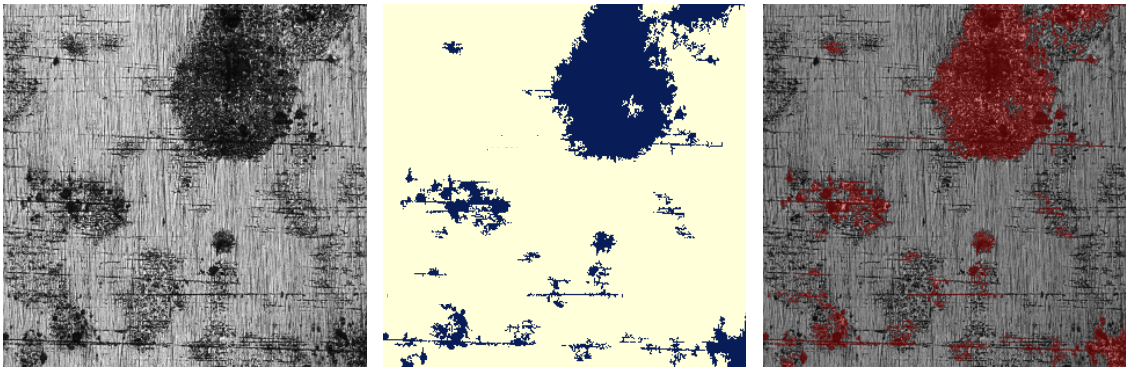

(a) (b) (c)

Figure B.10: Representative images of the specimen tested under $SWT = 375$ MPa, $R = 0.1$ load ratio used to perform the corrosion level quantitative analysis. (a) Rough image, (b) detected corroded areas and (c) verification step.

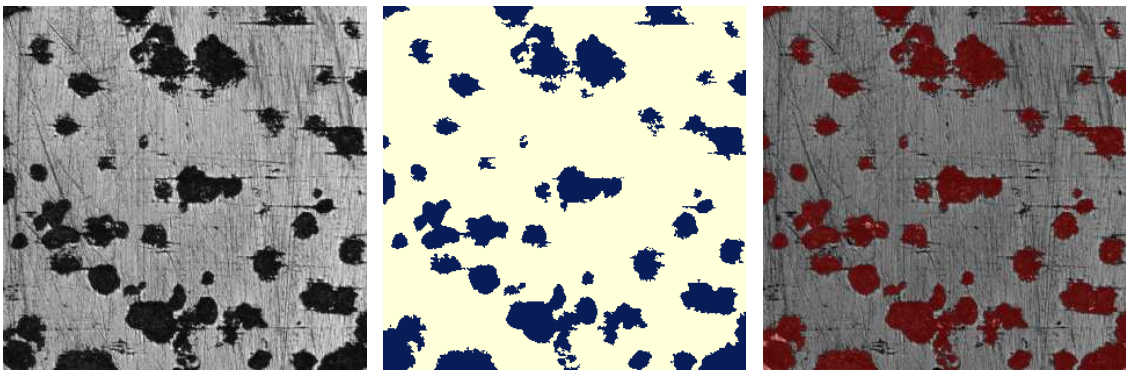

(a) (b) (c)

Figure B.11: Representative images of the specimen tested under $SWT = 450$ MPa, $R = 0.1$ load ratio used to perform the corrosion level quantitative analysis. (a) Rough image, (b) detected corroded areas and (c) verification step.

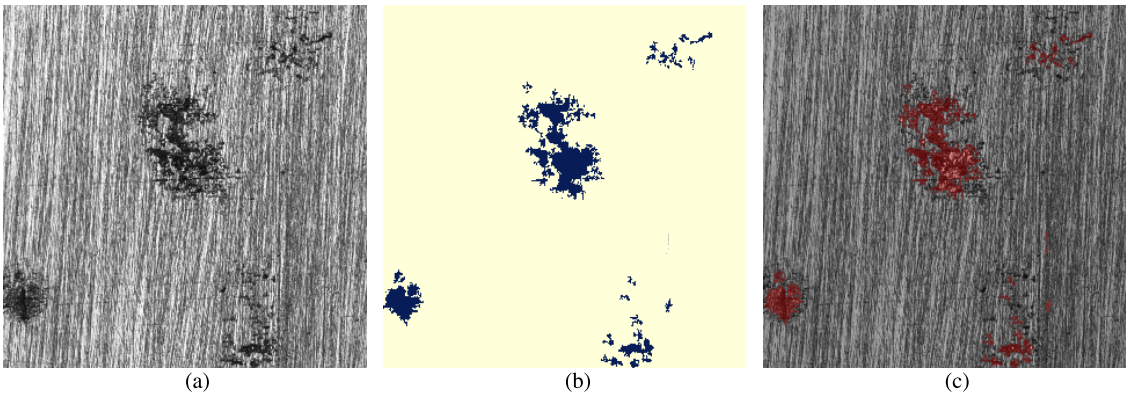

(a) (b) (c)

Figure B.12: Representative images of the specimen tested under $SWT = 500$ MPa, $R = 0.1$ load ratio used to perform the corrosion level quantitative analysis. (a) Rough image, (b) detected corroded areas and (c) verification step.

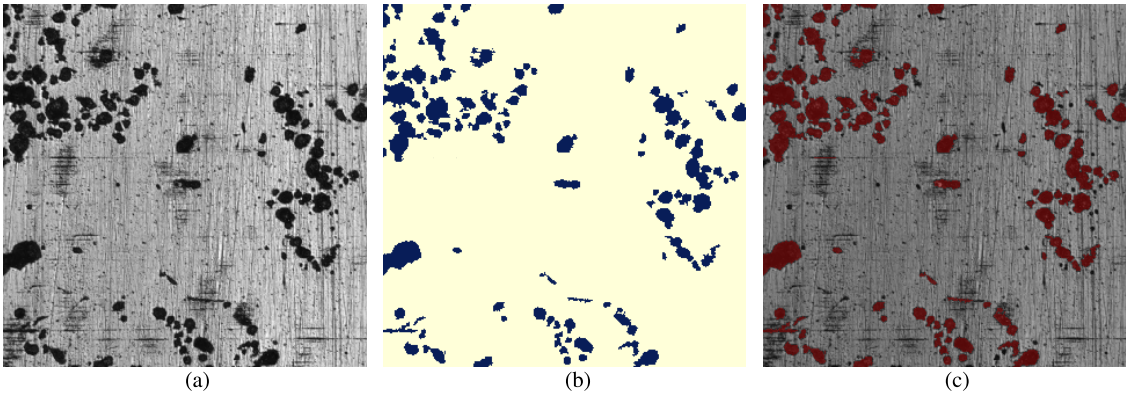

(a) (b) (c)

Figure B.13: Representative images of the specimen tested under $SWT = 550$ MPa, $R = 0.1$ load ratio used to perform the corrosion level quantitative analysis. (a) Rough image, (b) detected corroded areas and (c) verification step.

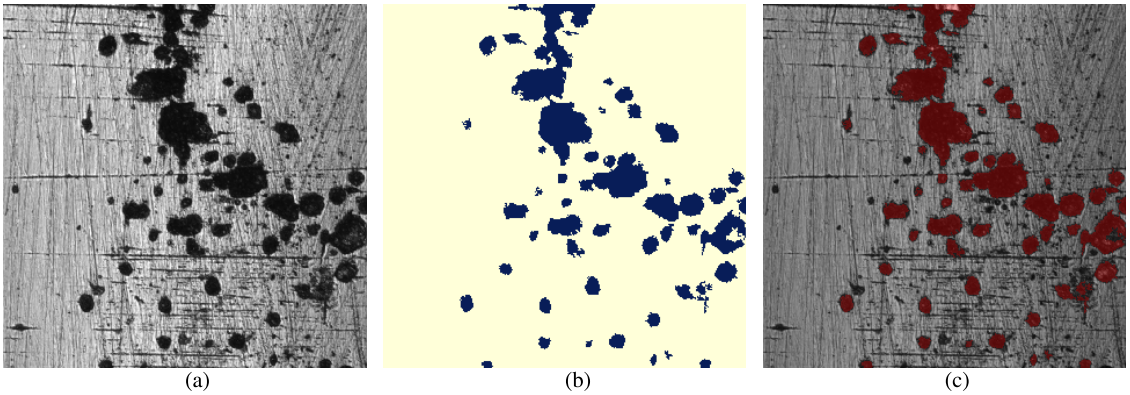

(a) (b) (c)

Figure B.14: Representative images of the specimen tested under $SWT = 650$ MPa, $R = 0.1$ load ratio used to perform the corrosion level quantitative analysis. (a) Rough image, (b) detected corroded areas and (c) verification step.

B.4 Trunk Conical Specimens

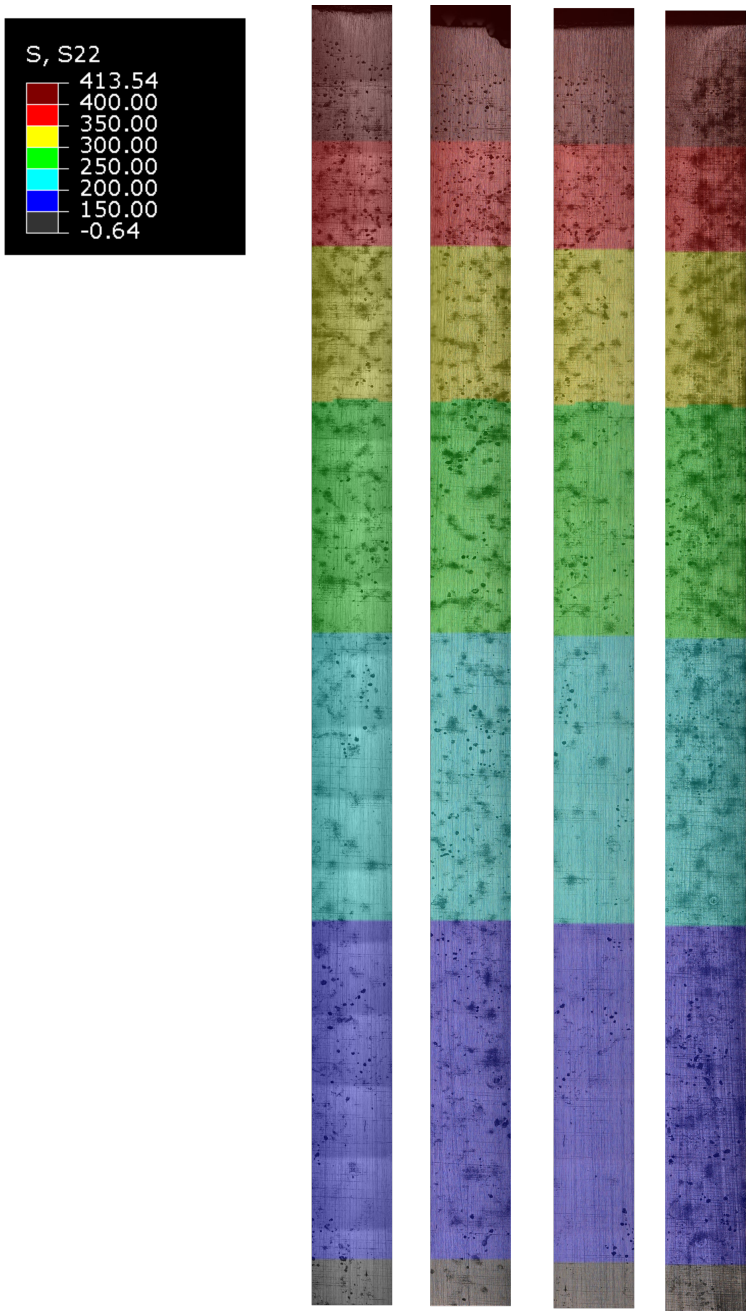

Figure B.15: Representative images of the trunk conical specimen tested under $SWT = 400$ MPa (calculated at the minimal diameter) and $R = 0.1$ load ratio.

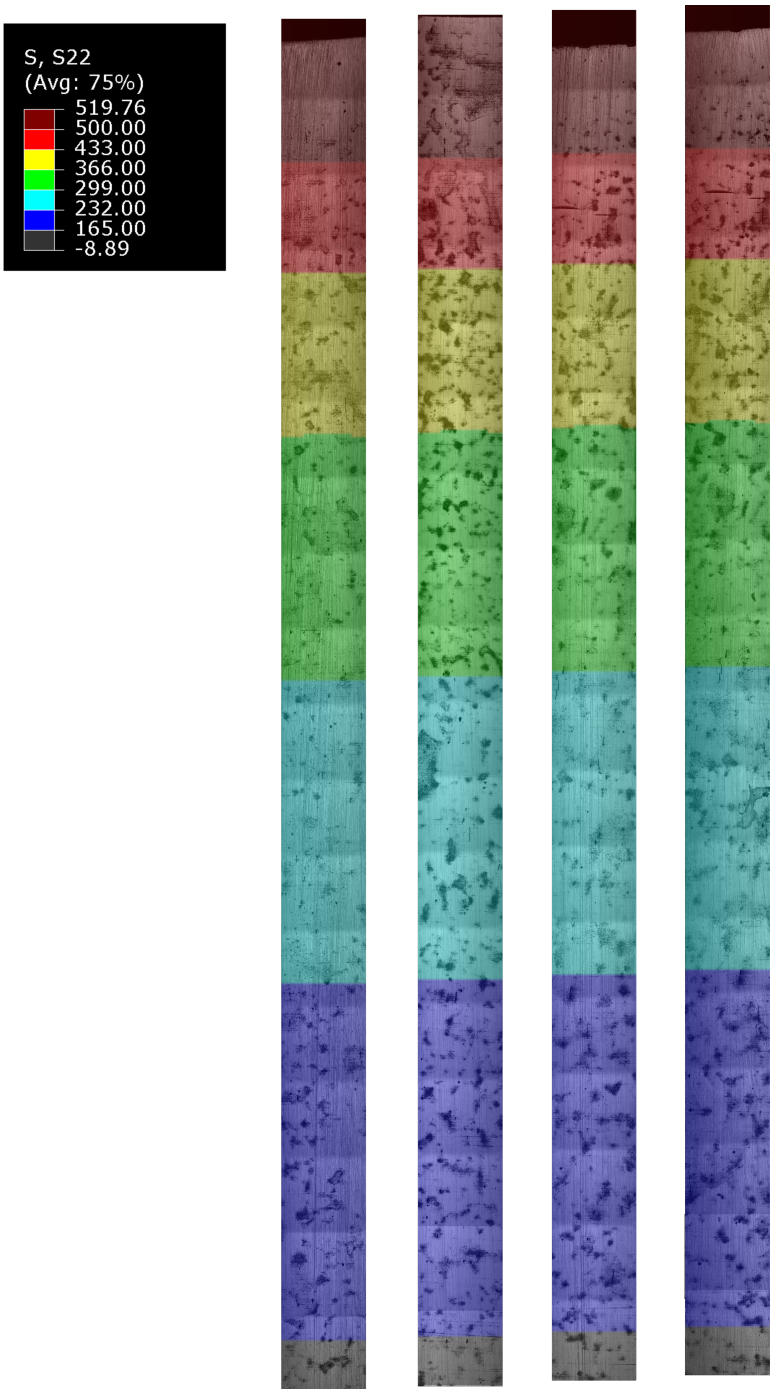

Figure B.16: Representative images of the trunk conical specimen tested under $SWT = 500$ MPa (calculated at the minimal diameter) and $R = 0.1$ load ratio.

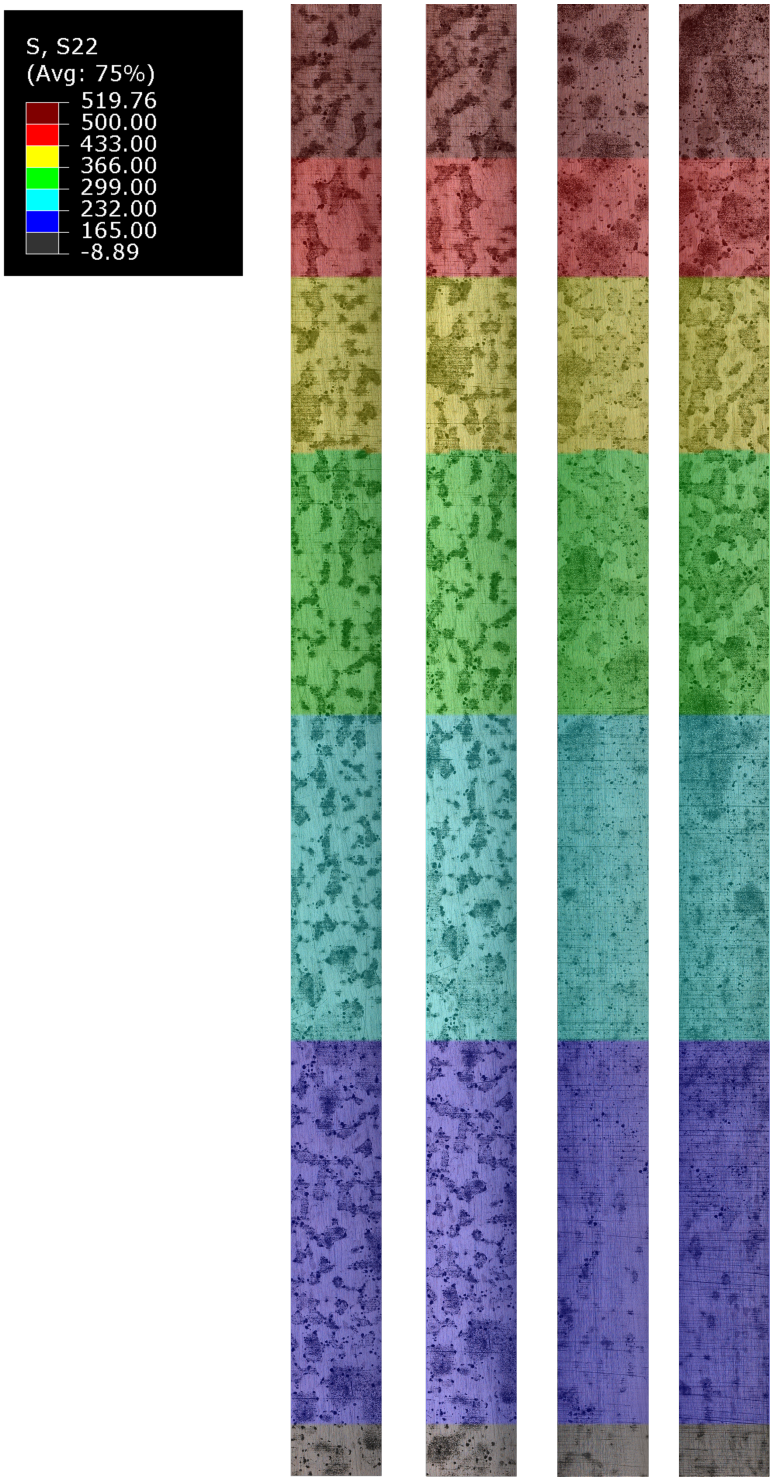

Figure B.17: Representative images of the trunk conical specimen tested under $SWT = 500$ MPa (calculated at the minimal diameter), $R = 0.1$ load ratio and lower load frequency, $f = 0.1$ Hz.